New active three-level laser materials and their use with innovative geometries for efficient continuous-wave and mode-locked coherent sources

im
Fachbereich Physik
der
Freien Universität Berlin
eingereichte Dissertation
von

Simon Rivier

October 2008

1^{st} referee : Prof. Dr Ingolf Volker Hertel
Freie Universität Berlin, Germany

2^{nd} referee : Prof. Dr Markus Pollnau
University of Twente, Enschede, The Netherland

Date of Disputation : 27^{th} October 2008

To my parents,

who have given me everything they could possibly give

Abstract

There is an increasing demand for efficient, reliable and compact diode-pumped solid-state laser sources in both the continuous-wave and pulsed operation regimes. In the 1 μm spectral range, Yb^{3+}-doped gain media are ideally suited as the absorption band is covered by high-power InGaAs laser diodes. Moreover, the very simple electronic configuration of Yb^{3+}, based on two multiplets, reduces the number of parasitic spectroscopic processes and provides a low quantum defect, reducing the thermal effects. Finally, depending on the host, Yb-doped materials exhibit broad emission bands that enable the production of femtosecond pulses in the mode-locked regime.

This thesis investigates two extremely promising groups of doubles tungstate crystals as laser media; the monoclinic double tungstates $KT(WO_4)_2$ and the tetragonal double tungstates $NaT(WO_4)_2$, where T is a trivalent metal or rare-earth cation. The potential of monoclinic double tungstates as laser materials has not only recently be confirmed by the scientific community. As a matter of fact, the strong anisotropy of the monoclinic double tungstates results in the cumulation of the favorable features, a large and broad emission cross section particularly, for one crystal orientation. Moreover, some of these crystals can advantageously tolerate extremely high doping concentration up to the stoichiometric level (100% doping), indicating potential development of exceptionally thin active structures. The anisotropy of their thermo-mechanical properties introduces, however, some limitations and actually prevented till recently the manufacture of advantageous composite structure. In this thesis, laser experiments based on several of such composite structures are performed for the first time. In particular, composite geometries including planar waveguides and composite thin disk were studied and slope efficiencies close to the theoretical limit were achieved. Such structures were also investigated for passive mode-locking and pulse durations as short as 66 fs were notably obtained with a diode-pumped diffusion bonded Yb:$KY(WO_4)_2$ /$KY(WO_4)_2$ crystal. This corresponds to the shortest pulse ever achieved with monoclinic double tungstate lasers and any Yb laser based on a composite crystal. With Ti:sapphire laser pumping and external compression, the pulse duration could be even further shortened to 62 fs.

The other group of crystals investigated, the tetragonal double tungstates, are characterized by a local disorder. Thus, when doped with rare-earth ions, the transition cross sections exhibit significant inhomogeneous broadening leading to broad and smooth absorption and emission bands. This denotes, on one hand, relaxed requirements for diode pumping and, on the other hand, a high potential for ultrashort pulse generation. For the first time, continuous-wave laser operation has been investigated with Yb:$NaY(WO_4)_2$ and a slope efficiency of nearly 70 % has been achieved. The pulse duration in the passive mode-locked regime was as short as 53 fs, which corresponds to one of the shortest pulse generated from any Yb laser.

Keywords: Solid-state lasers, mode-locked lasers, rare earth doped materials

Zusammenfassung

Effiziente, zuverlässige und kompakte diodengepumpte Festkörperlaser, sowohl jene im Dauerstrich-, als auch im gepulsten Betrieb, stehen unter steigender Nachfrage. Im Spektralbereich um 1 μm sind Yb^{3+} dotierte Verstärkermedien besonders geeignet, da deren Absorptionsbande durch InGaAs Laserdioden hoher Leistung abgedeckt wird. Ferner reduziert die sehr einfache Elektronenkonfiguration des Yb^{3+}-Ions, bestehend aus zwei Multipletts, die Anzahl möglicher parasitärer spektroskopischer Übergänge. Dies resultiert in einem geringen Quantendefekt, was wiederum thermische Auswirkungen minimiert. Außerdem weisen Yb-dotierte Materialien in Abhängigkeit des Hostkristalls spektral breite Emissionsbanden auf, welche die Erzeugung von Femtosekundenpulsen im modengekoppelten Betrieb erlauben.

Die vorliegende Dissertation untersucht zwei vielversprechende Gruppen von Wolframaten: Die monoklinischen Wolframate mit der nominalen Formel $KT(WO_4)_2$ und die Gruppe der tetragonalen Wolframate $NaT(WO_4)_2$, wobei T jeweils für ein dreiwertiges Metall bzw. ein Kation eines Seltenerdmetalls steht. Das Potential monoklinischer Wolframate zur Nutzung als Lasermedium ist unlängst in wissenschaftlichen Kreisen bestätigt worden. Bewiesenermaßen resultiert die starke Anisotropie der monoklinischen Wolframate in einer Kumulation günstiger Charakteristika wie zum Beispiel einem großen und breiten Emissionsquerschnitt, vor allem für eine Kristallorientierung. Darüber hinaus ist es möglich, einige dieser Kristalle sehr hoch zu dotieren, bis hin zu Dotierungsgraden von 100% (stöchiometrische Kristalle). Diese vorteilhafte Eigenschaft birgt großes Potential hinsichtlich der Entwicklung außergewöhnlich dünner aktiver Strukturen.

Die Anisotropie ihrer thermisch-mechanischen Eigenschaften führt einige Einschränkungen mit sich, die bis vor Kurzem die Herstellung nutzbarer Komposita vereitelt haben. Im Rahmen der vorliegenden Dissertation wurden erstmals Laserexperimenste auf Basis verschiedener dieser Komposita-Strukturen durchgeführt. Insbesondere wurden Komposita-Geometrien wie z.B. planare Wellenleiter und die Scheibengeometrie untersucht. Die damit erreichten Wirkungsgrade lagen jeweils nahe an der erreichbaren theoretischen Obergrenze. Diese Strukturen wurden auch im Hinblick auf die Erzeugung kurzer Pulse mittels passiver Modenkopplung untersucht. Hierbei wurden mit einem diodengepumpten diffusionsgebondeten Yb:$KY(WO_4)_2$ /$KY(WO_4)_2$ Kristall Pulsdauern von 66 fs erreicht. Dies entspricht den kürzesten Pulsen, welche jemals mit monoklinischen Wolframaten und mit auf Komposita Kristallen basierten Yb-Lasern erreicht wurden. Durch Nutzung eines Titan-Saphir Lasers als Pumplaser und zusätzlicher externer Kompression konnte die Pulsdauer auf 62 fs verkürzt werden.

Die andere Gruppe der untersuchten Kristalle, die der tetragonalen Wolframate, ist durch einen lokal ungeordneten Kristall charakterisiert. Aus diesem Grund weisen die Übergangsquerschnitte eine signifikante inhomogene Verbreiterung auf, wenn die Kristalle mit Seltenerd-Ionen dotiert werden. Breite und glatte Absorptions- und Emissionsbanden sind der Folge, welche einerseits geringere Anforderungen an das Diodenpumpen und andererseits ein hohes Potential für die Erzeugung ultrakurzer Pulse implizieren. Zum ersten Mal untersucht wurde der Dauerstrichbetrieb des Yb:$NaY(WO_4)_2$ und dabei ein Wirkungsgrad von fast 70% erzielt. Im modengekoppelten Betrieb wurden Pulse von nur 53 fs Dauer erreicht. Diese Pulsdauer rangiert unter den kürzesten Pulsen die je mit einem Yb-Laser erzeugt wurden.

Contents

Chapter 1

General introduction

Since the demonstration of the first laser in 1960, based on a synthetic ruby, the unique properties of the laser radiation have constantly revealed new perspectives in fundamental research as well as in industrial applications. Nearly 50 years later, an impressive number of laser sources have been developed based on dielectric crystalline media, semiconductors, liquid solutions or gases. Among all these possibilities, solid-state lasers and especially diode-pumped solid-state lasers provide excellent potentiality due to their reliability, multiple emission wavelengths and mode of operation (continuous-wave, Q-switched, Raman, picosecond, femtosecond etc.) that enable wide areas of applications. In particular, new prospects in material processing, biology, medicine and metrology are emerging. One of the major evolution in laser physics over the last decade is connected with the gradual replacement of the well known neodymium lasers by the potentially more suitable Yb-doped gain media.

This important transition is closely related with the development of high brightness InGaAs laser diodes developed for telecommunication that allow in band pumping of Yb-doped lasers. The Yb ion is distinguished by its very simple energy level scheme based on only two manifolds so that various parasitic spectroscopic processes are avoided and a minimal difference between pump and laser wavelength can be maintained. Hence, extremely efficient laser operation can be achieved and scaling to formerly unattainable output power level is feasible. However, this very simple energy diagram is unfortunately also associated with undesired effects such as a strong thermal dependence so that special procedures have to be introduced to limit these inconveniences.

A key step in the development of such laser sources is the selection of an appropriate host as the spectroscopic characteristics of the Yb ion are known to vary strongly with the internal crystal field. With a suitable gain medium, favorable spectroscopic properties such as a large emission cross section for efficient continuous-wave laser operation or a broad emission cross section for femtosecond pulse generation can be obtained. For specific crystals such as those investigated in this work, the monoclinic double tungstates, such properties can even be collected for one particular orientation. For the other type of crystals investigated, the tetragonal double tungstates, the local disorder of the crystal gives rise to an additional inhomogeneous broadening of the linewidths, that results in an exceptional potential for ultrashort pulse generation.

An additional way to obtain optimum performance is the implementation of special geometries or composite structures that permit efficient heat removal or enhanced overlap of the pump and laser mode. The realization of such innovative structures for the appropriate laser

host, in this case the monoclinic double tungstates, is highly challenging as these materials are characterized by a strong anisotropy.

The aim of this thesis is to apprehend the specific features of the Yb-doped double tungstates as well as the influence of the novel composite structures. In this way, optimum performance in the continuous-wave regime can be achieved with slope efficiencies close to the theoretical limit. In the ultrashort pulse regime, the effect of dispersion together with optical nonlinearities play a central role to achieve efficient and stable operation. The understanding of this interplay as well as the selection and optimization of the appropriate crystal or composite structure are also decisive factors to support the generation of femtosecond pulses. As a result, some of the shortest pulses ever achieved with an Yb laser can be obtained.

As one can understand from this general introduction, an intense collaboration between the research groups dealing with the crystal growth, sample preparation and spectroscopy and myself, investigating the laser performance of such structures, is required. In that way, excellent understanding of the key parameters of these gain media as well as optimum results can be achieved. Such close collaboration was facilitated by the framework of the european project: **DT-CRYS Double Tungstate Crystals: Synthesis, Characterization and Application** involving nine different institutions. For my particular investigations, a close collaboration with four groups of research was carried on. Thus, I would like to briefly present these four groups I have been collaborating with and their area of research. Note also that all published results are joint publications between the crystal growth institutes and the Max-Born-Insitut.

The group FiCMA (Fisica i Cristal.lografia de Materials) at the Universitat Rovira I Virgili (URV), Tarragona, Spain:
This group, lead by Prof. F. Diaz, is working on physics and crystallography of materials. The present research interests are focussed on the growth and characterization of materials for the laser technology. In this project, their activities include high temperature crystal growth (Top-Seeded-Solution-Growth, TSSG), Liquid-Phase-Epitaxy (LPE), sample preparation (orientation, cutting and polishing) as well as the crystallographic, electric, thermal and optical (absorption, fluorescence, dispersion) characterization of the monoclinic double tungstates. Their study and results are shortly presented in this thesis in section 3.1 as well as in section 4.4.1.

The group of Spectroscopy and Laser Materials at The Materials Science Institute of Madrid (ICMM), Madrid, Spain:
The group of Spectroscopy and Laser Materials at ICMM, lead by Prof. C. Zaldo, has expertise on single crystal growth as well as in optical characterization. Crystal growth is based on the Czochralski technique and applied to materials with congruent melting. Recent activity has been focussed on $AT(MoO_4)_2$ (A=Li, Na; T=Bi, Gd) doped with Ln-ions. In this project, their activities include the Czochralski growth as well as the Top-Seeded-Solution-Growth, sample preparation (orientation, cutting and polishing) as well as the crystallographic, electric, thermal and optical (absorption, fluorescence, dispersion) characterization of the tetragonal double tungstates. Their study and results are summarized in this thesis in section 3.2.

The Novel Oxide Waveguides (NOW) group from the Applied Photonics Laboratory at the Ecole Polytechnique Fédérale de Lausanne (EPFL), Lausanne, Switzerland
The Novel Oxide Waveguide group, lead by Prof. M. Pollnau now at the University of Twente,

Netherland, has expertise in crystal and thin-film growth, surface micro-structuring, optical and spectroscopic characterization of actively doped materials. In this particular work, this group produced and optically characterized the monoclinic double tungstates waveguides. Their results are briefly described in section 4.4.1.

Forschungsinstitut für mineralische und metallische Werkstoffe, Edelsteine/Edelmetalle GmbH (FEE), Germany
The team of the Forschungsinstitut für mineralische und metallische Werkstoffe, Edelsteine/ Edelmetalle GmbH specializes in crystal growth and manufacturing of optical elements for laser applications. In particular, they developed and optimized two new techniques to produce composite structures based on the monoclinic double tungstates. This work is summarized in sections 4.4.2 and 4.4.3.

Although the **Ferdinand-Braun-Insitut, Germany** was not directly involved in the European project a close collaboration has been carried on with this institute. The laser diodes as well as the semiconductor saturable absorbers were manufactures in this institute.

This thesis begins, in chapter 2, with a general introduction on Yb-doped gain media where the fundamental properties of such laser sources are detailed. This is followed in chapter 3 by a comprehensive description of the monoclinic and tetragonal double tungstate crystals as well as a comparison of these compounds with other well known gain media. The following chapter (chapter 4) deals with specific geometries and structures that enable efficient laser operation and their implementation with monoclinic double tungstates.

The most representative experimental results obtained in the continuous-wave regime with bulk and newly introduced composites based on the monocinic double tungstates as well as results with the novel tetragonal double tungstates are then presented in chapter 5. In chapter 6, the theory of passive mode-locking, the most reliable method to generate femtosecond pulses, is reviewed while in chapter 7, selected experimental results achieved in the mode-locked regime with the double tungstates and these innovative geometries, leading to the shortest pulse ever achieved with Yb-doped gain media, are described.

Own publications directly related to this thesis:

[1] S. Rivier, V. Petrov, U. Griebner, A. Gross, S. Vernay, V. Wesemann, and D. Rytz, Diffusion bonding of monoclinic Yb:$KY(WO_4)_2$ /$KY(WO_4)_2$ and its continuous-wave and mode-locked laser performance. *Applied Physics Express*, 1:112601, (2008).

[2] A. Schmidt, S. Rivier, V. Petrov, U. Griebner, A. García-Cortés, F. Esteban-Betegón, M. D. Serrano, and C. Zaldo, Diode-pumped femtosecond Yb:$NaY(WO_4)_2$ laser. *Electronics Letters*, 44: 806-807, (2008).

[3] S. Rivier, X. Mateos, O. Silvestre, V. Petrov, U. Griebner, M. C. Pujol, M. Aguiló, F. Díaz, S. Vernay, and D. Rytz, Thin-disk Yb:$KLu(WO_4)_2$ laser with single-pass pumping. *Optics Letters*, 33 (7): 735-737, (2008).

[4] A. Schmidt, S. Rivier, G. Steinmeyer, J. H. Yim, W. B. Cho, A. Lee, F. Rotermund, V. Petrov, and U. Griebner, Passive mode locking of Yb:KLuW using single-walled carbon nanotube saturable absorbers, *Optics Letters*, 33 (7): 729-731, (2008).

[5] X. Han, J. M. Cano-Torres, M. Rico, C. Cascales, C. Zaldo, X. Mateos, S. Rivier, U. Griebner,

and V. Petrov, Spectroscopy and efficient laser operation near 1.95 μm of Tm^{3+} in disordered $NaLu(WO_4)_2$. *Journal of Applied Physics,* 103:083110, (2008).

[6] A. Schmidt, S. Rivier, V. Petrov, U. Griebner, A. García-Cortés, M. D. Serrano, C. Cascales, and C. Zaldo, Continuous-wave and mode-locked operation of diode-pumped Yb:$NaY(WO_4)_2$. *Proceeding SPIE,* Vol. 6998, 69980X (2008).

[7] J. M. Cano-Torres, X. Han, A. García-Cortés, M. D. Serrano, C. Zaldo, F. J. Valle, X. Mateos, S. Rivier, U. Griebner, and V. Petrov, Infrared spectroscopic and laser characterization of Tm in disordered double tungstates. *Materials Science and Engineering: B*, 146 (1-3):22-28, (2008).

[8] S. Rivier, V. Petrov, A, Gross, S. Vernay, V. Wesemann, D. Rytz, and U. Griebner, Segmented grown Yb:$KY(WO_4)_2$ /$KY(WO_4)_2$ for use in continuous-wave and mode-locked lasers. *Optics Express,* 15 (24):16279-16284 (2007).

[9] S. Rivier, A. Schmidt, C. Kränkel, R. Peters, K. Petermann, G. Huber, M. Zorn, M. Weyers, G. Erbert, V. Petrov, and U. Griebner, Ultrashort pulse Yb:$LaSc_3(BO_3)_4$ mode-locked oscillator. *Optics Express,* 15 (23):15539-15544 (2007).

[10] A. García-Cortés, J. M. Cano-Torres, M. D. Serrano, C. Cascales, C. Zaldo, S. Rivier, X. Mateos U. Griebner, and V. Petrov, Spectroscopy and Lasing of Yb-doped $NaY(WO_4)_2$: tunable and femtosecond mode-locked laser operation. *IEEE Journal of Quantum Electronics,* 43 (9):758-764 (2007).

[11] M. Pollnau, Y. E. Romanyuk, F. Gardillou, C.N. Borca, U. Griebner, S. Rivier, and V. Petrov, Double tungstate lasers, from bulk toward on-chip integrated waveguides devices. *IEEE Journal of Selected Topics in Quantum Electronics,* 13 (3):661-671 (2007).

[12] V. Petrov, M. Cinta Pujol, X. Mateos, O. Silvertre, S. Rivier, M. Aguiló, R.M. Solé, J. Liu, U. Griebner, and F. Díaz, Growth and properties of $KLu(WO_4)_2$ and novel ytterbium and thulium lasers based on this monoclinic crystallie host. *Laser & Photonics Review,* 1 (2):179-212 (2007).

[13] S. Rivier, X. Mateos, V. Petrov, U. Griebner, Y. E. Romanyuk, C. N. Borca, F. Gardillou, and M. Pollnau, Tm:$KY(WO_4)_2$ waveguide laser. *Optics Express,* 15 (9):5885-1892 (2007).

[14] A. García-Cortés, M. Cano-Torres, X. Han, C. Cascales, C. Zaldo, X. Mateos, S. Rivier, U. Griebner, V. Petrov, and F. J. Valle, Tunable CW and femtosecond mode-locked Yb^{3+} laser operation in $NaLu(WO_4)_2$ *Journal of Applied Physics,* 101:063110 (2007).

[15] V. Petrov, X. Mateos, S. Rivier, O. Silvestre, M. Aguiló, R. Solé, M. C. Pujol, J. Liu, U. Griebner, and F. Díaz, Novel ytterbium and thulium lasers based on the monoclinic $KLu(WO_4)_2$ crystalline host. *Proceeding SPIE,* Vol. 6604, 66040V (2007).

[16] S. Rivier, X. Mateos, J. Liu, V. Petrov, U. Griebner, M. Zorn, M. Weyers, H. Zhang, J. Wang, and M. Jiang, Passively mode-locked Yb:$LuVO_4$ oscillator. *Optics Express,* 14 (24):11668-11671 (2006).

[17] Y. E. Romanyuk, C. N. Borca, M. Pollnau, S. Rivier, V. Petrov, and U. Griebner, Yb-doped $KY(WO_4)_2$ planar waveguide laser. *Optics Letters,* 31 (1):53-55 (2006).

[18] V. Petrov, S. Rivier, U. Griebner, J.Liu, X. Mateos, A. Aznar, R. Solé, M. Aguiló, and F. Díaz, Epitaxially grown Yb:$KLu(WO_4)_2$ composites for continuous-wave and mode-locked lasers in the 1 μm spectral range. *Journal of Non-Crystalline Solids,* 352 (23-25):2367-2370 (2006).

[19] S. Rivier, V. Petrov, U. Griebner, A. Aznar, X. Mateos, O. Silvestre, R. Solé, M. Aguiló, F. Díaz, M. Zorn, and M. Weyers, Mode-locked laser operation of epitaxially grown Yb:$KLu(WO_4)_2$ composite. *Optics Letters,* 28 (18):2484-2486 (2005).

[20] U. Griebner, S. Rivier, V. Petrov, M. Zorn, G. Erbert, M. Weyers, X. Mateos, R. Solé, J. Gavaldà, M. Aguiló, J. Massons, and F. Díaz, Passively mode-locked Yb:KLu(WO_4)$_2$ oscillators. *Optics Express,* 13 (9):3465-3470 (2005).

[21] U. Griebner, J. Liu, S. Rivier, A. Aznar, R. Gunwald, R. Solé, F. Díaz, and V. Petrov, Laser operation of epitaxially grown Yb:KLu(WO_4)$_2$ / KLu(WO_4)$_2$ composites with monoclinic crystalline structure. *IEEE Journal of Quantum Electronics,* 41(3):408-414 (2005).

Chapter 2

Yb^{3+}-doped gain media

In the following chapter, the fundamental features of Yb^{3+}-doped gain media are presented. It begins with a general introduction on this active ion. In particular, this first part focuses on the specificity of the Yb ion when compared to other active ions and discusses the fundamental influence of the host. In the second part of this chapter, some fundamental equations describing the laser threshold as well as the optical efficiency of Yb-doped lasers are developed. Such equations will be used again in subsequent chapters to compare the different gain media and the different geometries that can be implemented.

2.1 Optical Amplification

The underlying principle for achieving intense, coherent light is "Light Amplification by Stimulated Emission of Radiation", known by its acronym as the **LASER** process. In general, light transmitted through a material is attenuated rather than amplified. The reason is the absorption by the large population of atoms in the lowest energy level at thermal equilibrium. Optical amplification requires then to excite atoms, ions or molecules into higher energy levels creating a non equilibrium situation and generating a population inversion.

In order to understand better the essential features of the formation of a population inversion, one usually distinguishes the operating schemes in two fundamental categories, the four- and three-level laser systems as illustrated in figure 2.1. In both operation schemes, the population inversion is achieved by exciting the active ions from the ground state into the uppermost level 3, followed by a very fast non-radiative transfer into the upper laser level 2 by multi-phonon transitions. In a four-level laser medium, the laser transition then takes place between the excited laser level 2 and the lower laser level 1 which lies well above the ground state level before a fast non-radiative relaxation into the ground state. On the contrary, the laser transition in a three-level laser medium occurs from the excited level directly to the ground state.

From these basic considerations, it is straightforward that the conditions to achieve population inversion and thus optical amplification are very different in a three- or a four-level laser medium. In a three-level laser system, if we assume an extremely fast decay from the uppermost level to the upper laser level, the number of atoms N_3 in level 3 is then negligible and $N_1 + N_2 \approx N_{tot}$. The condition for optical amplification, $\Delta N = N_2 - N_1 > 0$, directly shows

that more than half of the atoms have to be raised from the ground state to the upper laser level. In a four-level laser system, under the same assumption that the non-radiative transitions are much faster than the radiative transition so that $N_0 + N_2 \approx N_{tot}$, one finds that every excited atom will directly create population inversion $\Delta N = N_2 - N_1$.

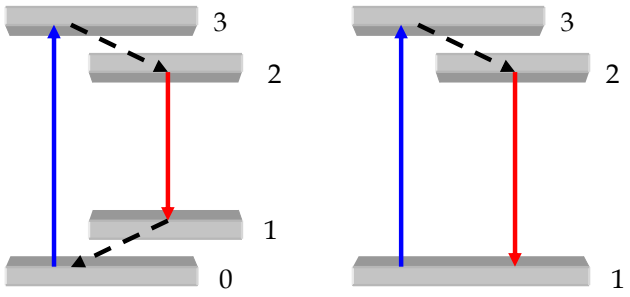

Figure 2.1: Four- and three-level laser operation schemes

Consequently, an ideal four-level laser medium is generally characterized by a very low laser threshold and a gain that usually increases with the absorbed pump power while an "ideal" three-level laser is distinguished by a high threshold as well as a significant reabsorption of the laser radiation due to the significant population in the lower laser level.

2.2 The Ytterbium ion

The operation schemes of real lasers are often more diverse and complex than the two simple models shown earlier so that they have to be adapted to the actual energy level diagrams. We will here have a closer look at the popular trivalent rare-earth-doped gain media. Media doped with rare earth ions, also referred to as lanthanides, usually exhibit favorable properties and give access to a broad range of wavelengths from the ultraviolet to the mid-infrared. The triply ionized rare-earths are characterized by electronic transitions that take place within the 4f shell [DC63]. The orbit is closer to the center than the larger main quantum numbers 5s, 5p, 6s orbits so that 4f electrons are shielded from the environments by the outer layer electrons. Thus, the trivalent rare earth ions can be incorporated into crystal lattice where they retain their sharp energy levels that are only slightly modified by the internal crystal field. For most trivalent rare-earth ions, more than one 4f electron is present so that many levels in the $4f^n$ configuration are possible leading to numerous potential laser transitions. However, in the case of Ce^{3+}, with only one 4f electron or Yb^{3+}, where the complete shell lacks one 4f electron, only a ^2F doublet can arise. Thus, as it can be seen in figure 2.2, the energy level diagram of these two trivalent ions is very simple.

Finally, the Yb^{3+}ion with the electronic configuration [Xe]$4f^{13}$, is more favorable as its energy diagram is composed of two energy levels separated by ≈ 10000 cm^{-1}, corresponding to a convenient wavelength in the near infrared. When the rare-earth ions are subsequently introduced in a laser host, the electric crystal field produces a Stark-effect, which splits all levels into a maximum of $J + 1$ components for an even number of electrons and $J + 1/2$ components for an odd number.

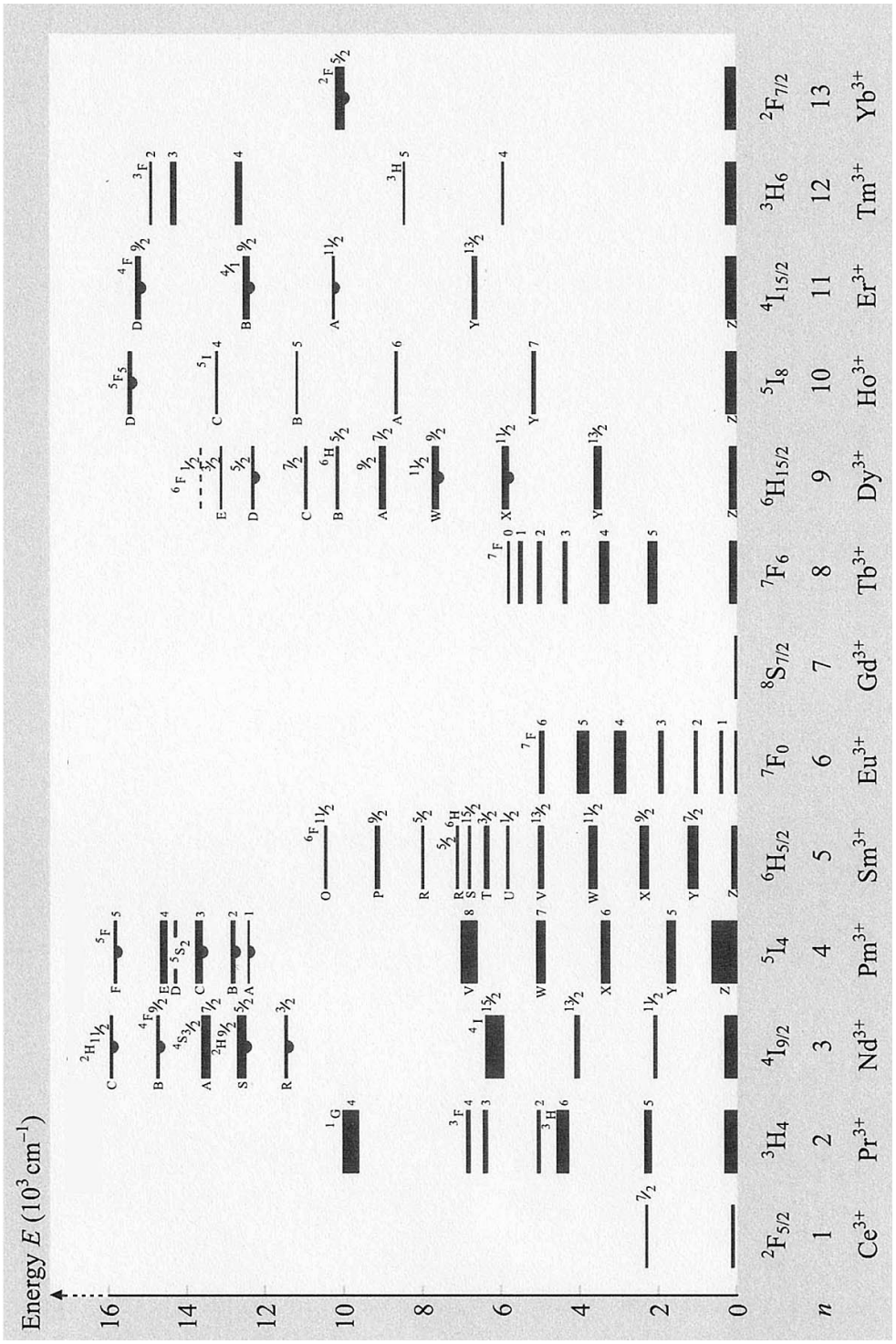

Figure 2.2: Energy level diagrams of trivalent rare earth ions in $LaCl_3$ for energy E lower than 16×10^3 cm^{-1} [Spr07]

In the case of Yb^{3+}, the Stark effect splits the ground state $^2F_{7/2}$ into four Stark sub-levels (0), (1), (2), and (3) and the excited state $^2F_{5/2}$ in three Stark sub-levels (0′), (1′) and (2′). The Stark splitting typically depends on the symmetry and intensity of the crystal field and can vary from ≈ 400 to ≈ 1200 cm^{-1} for a multiplet depending on the host. Finally, broadening of these lines will occur, primarily due to strong electron-phonon coupling and, to some extent, to inhomogenous broadening.

The Yb^{3+}laser, a quasi-three level system

At thermal equilibrium, the relative populations of the levels in a multiplet rapidly (< 10 ps) establish a Boltzmann distribution. For example, the population N_a of a Stark level (a) of the lower multiplet can be written:

$$N_a = \frac{g_a exp(-E_a/k_B T)}{Z_a} N_0 = f_a N_0 \tag{2.1}$$

with
$$Z_a = \sum_i g_i exp(-E_i/k_B T) \tag{2.2}$$

where N_0 is the total dopant concentration of the lower multiplet, k_B the Boltzmann constant, Z_a the partition function, f_a is the fractional population in the level, g_i and g_a are the degeneracy of states i and a and E_i the energy. In ytterbium, each level has a degeneracy of 2. This indicates that at room temperature, Stark levels within ~ 1000 cm^{-1} are connected with a thermal population.

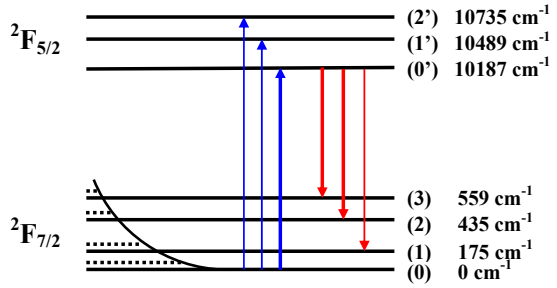

Figure 2.3: Schematic diagram of the Stark levels and transitions of the Yb^{3+} ion showing the thermally populated levels. On the right side, the Stark level energies of Yb^{3+}in $KLu(WO_4)_2$ are reported. Note that the thermal population in the lower multiplet is strongly accentuated in the figure. For example, at room temperature, the relative population of a energy level at 435 cm^{-1} is $\sim$10%.

As a consequence, the ytterbium laser represents an intermediate case between the ideal four- and three-level lasers and is commonly referred to a *quasi-three level laser* [1]. The transitions related with the absorption, shown by the blue arrows in figure 2.3, take place between

1. Note that an absolutely rigorous designation should actually refer to quasi-three level laser only in the case of a pump transition from the lowest level of the lower multiplet to lowest level of the upper multiplet (zero line). In the case of a pump transition ending in a higher energy level, the term of quasi-four level sometimes appears. However, very sharp transitions from two distinct energy levels are not always present but rather broad transitions that make these

the lowest level of the lower multiplet (0) and the three levels of the upper multiplet (0′), (1′) and (2′). The transition from the (0) level to the (0′) level, called the zero line transition and shown by the thick blue arrow in the figure, is often used to efficiently pump ytterbium lasers as it usually presents a very high absorption peak around 975-980 nm. This is followed by fast intraband thermalization in the upper multiplet where most of the excited ions remain in the lower excited state level (0′). Finally, the laser transitions, shown by red arrows in the figure, take place from this latter level down to the thermally populated levels of the lower multiplet (0), (1), (2), and (3). Stimulated emission from the excited state down to the lower levels of the ground state (1) and specially (0) is generally very difficult to achieve as it requires extremely high inversion.

Due to the thermal population of the lower laser levels, unpumped region of the gain medium cause some loss at the laser wavelength. This leads to very specific properties:

- The threshold of these lasers can be substantially higher than their four-level alternative since the transparency of such crystals is reached only for fixed pump intensity. This explains the rather recent interest for ytterbium lasers as their performance is closely related to the development of high power, high brightness laser diodes that can provide adequate pump intensity for efficient operation. For longitudinal pumping configuration, a pump intensity above the transparency intensity has to be kept for efficient operation. This means that an optimum absorption below 100 % in non lasing condition is required.
- The laser operation is dependent on the temperature. The thermal distribution of the upper and lower multiplet will strongly influence the performance of the laser. A good thermal management, referring to both low heat generation and efficient heat dissipation, is therefore essential [2].
- The emission wavelength is changing with the cavity losses. The spectral shape of the optical gain varies with the balance of the emission and reabsorption at the laser wavelength and, therefore, with the inversion that can be achieved in the gain media. Thus, a significant shift of the laser wavelength is generally observed with different transmission of the output coupler.

Low quantum defect [3]

The drawback coming from the thermally populated lower laser level can nevertheless be largely compensated by the possibility of direct pumping with high power laser diodes with low thermal problems. The zero line transition corresponds to an important absorption peak around 980 nm that is well suited for direct pumping with readily available high power InGaAs laser diodes previously developed for erbium lasers. Thanks to the good spectral properties and the good beam quality of such diodes, it is possible to maintain a high overlap of the pump and laser beam reducing the reabsorption losses. It allows to reach high pump intensity so that the absorption is saturated and efficient operation of the laser can be obtained.

Moreover, as pump and laser transition involve the same two multiplets, the difference of

two distinctions somewhat ambiguous. In this thesis, the designation of quasi-three level lasers will then be employed as a generic term describing laser scheme that exhibit reabsorption losses.

2. Following this idea, cryogenically cooled ytterbium lasers have been studied and developed recently, showing remarkable improvements of the spectroscopic features as well as the thermo-mechanical properties

3. It is important to mention that the notion of quantum defect used in laser physics has no relation with the quantum defect theory used in atomic physics. While this duality can be misleading, there is unfortunately no other term expressing this concept in laser physics.

energy between the pump and laser photons, called the Stokes shift, can be kept exceptionally small. To characterize this, it is interesting to introduce the quantum defect q as

$$q = \frac{h\nu_P - h\nu_L}{h\nu_P} = 1 - \frac{\lambda_P}{\lambda_L} \tag{2.3}$$

where h is the Planck's constant, ν is the optical frequency and λ is the wavelength for the pump and laser photons. The quantum defect as defined here actually sets an upper limit to the power efficiency, given by the value 1-q. It is interesting to briefly compare the quantum defect of an ytterbium laser and the very well known neodymium laser. As we just saw, ytterbium lasers operate as a quasi-three level system while neodymium lasers are typically operating in a potentially more suitable four-level system. The quantum defect for a standard ytterbium tungstate laser being pumped at 980 nm and emitting at 1030 nm is as low as 4.8%. On the other hand, for a conventional neodymium YAG laser with a pump wavelength of 808 nm and a laser wavelength at 1064 nm, the quantum defect reaches 24%. This does not only indicate that the upper limit to the power efficiency is higher in Yb lasers but also means that the heat generation is considerably reduced. In fact, the difference of energy between the pump and laser photon is in general dissipated by lattice vibrations. Thus, a very small quantum defect denotes minor heat loading of the crystal, resulting in less stress and deformation and ultimately in further potential for power scaling.

Limited loss channels

The simple energy level scheme of Yb^{3+}reduces the heat generated in the system and, in addition, also decreases the inherent loss processes that can occur in a gain medium. In particular, parasitic spectroscopic mechanisms involving other energy levels such as upconversion or excited state absorption are absent. Impurities in the crystal could, however, act as quenching centers, giving access to separate deexcitation channels and decreasing the quantum efficiency as well. The quantum efficiency of fluorescence can be defined as the percentage of excited atoms that spontaneously decay by photon emission[4]. It can be seen as an indication of the competition between radiative and non-radiative decay channels.

The probability of energy transfer between ions is, in first approximation, determined by the dipole-dipole interaction and becomes important for active ions in proximity to the quenching center. For dipole-dipole interaction, this rate is inversely proportional to the sixth power of the distance between ions and hence grows very rapidly with increasing concentration of donors and impurities [Dex53]. The rate of resonant transfer between two ions also raises with increasing overlap of the absorption and emission spectra. In addition, at higher doping concentration, the resulting proximity of active ions of the same kind enhances the energy transfer between the donor ions and allows the excitation to travel inside the active material. This mechanism in turn enhances the non-radiative decay by bringing excited atoms closer to the quenching centers. The green fluorescence observed in Yb doped lasers is a good example of the resonant energy transfer between the excited state multiplet $^2F_{5/2}$ of Yb^{3+} to the $^4I_{11/2}$ state of Er^{3+}. Finally, an upconversion process takes place and a photon is emitted around 540 nm. For relatively low doping concentration and large active ion separation, this energy transfer is moderate and the quantum efficiency is kept very high.

4. Note that the quantum efficiency is not related to the quantum defect. While the latter is related to the photon energies, the quantum efficiency is related to the average number of output photons per pump photon.

Non-radiative transition by multiphonon relaxation process can also contribute to reduce the quantum efficiency. The non-radiative transition probability is inversely proportional to the energy gap of the two levels considered and also depends on the energy of the phonons. In Yb doped crystals, as the two multiplets are separated by $\sim$10000 cm^{-1} and the usual highest phonon energy is $\sim$1100 cm^{-1}, multiphonon relaxation requires as much as nine phonons which makes this process to be very unlikely.

In conclusion, at the condition that the quasi-three level behavior of Yb doped lasers can be controlled, the very simple energy level diagram, providing only limited heat generation and loss channels, as well as the good overlap of the absorption band with high power laser diodes elects ytterbium as the perfect active ion for compact and efficient diode pumped solid-state lasers.

2.3 The hosts

While some general properties of Yb doped laser materials have been shortly considered in the previous section, the influence of the host has still not been examined yet. The hosts will though influence many important spectroscopic and thermo-mechanical parameters and have therefore a major importance for close optimization of a laser. In terms of spectroscopic properties, the host will in particular have an important impact on the Stark splitting, the radiative lifetime τ_{rad} as well as the magnitude and bandwidth of the absorption cross section σ_{abs} and emission cross section σ_{em}. The spectroscopic properties discussed here are strongly interrelated. Let us then examine here the fundamental principles that regulate these features.

From the Einstein coefficients that relate the absorption and the stimulated emission in an energy system at thermal equilibrium, it is possible to obtain the McCumber relation [McC64], connecting the emission cross section and the absorption cross section in a gain medium. This relation is often used in spectroscopy and allows to obtain the emission cross section from the measured absorption cross section if the Stark level energies within the manifolds are known. This procedure is called the reciprocity method and is necessary when the overlapping of the absorption and emission cross section does not allow reliable experimental determination of the emission cross section. The relation between absorption cross section σ_{abs} and emission cross section σ_{em} is given by:

$$\sigma_{em}(\lambda) = \sigma_{abs}(\lambda)\frac{Z_l}{Z_u}exp\left(-\frac{E_{zl} - h\nu}{k_B T}\right) \tag{2.4}$$

where Z_l and Z_u are the partition functions of the lower and upper levels as defined in equation 2.2, k_B is the Boltzmann constant, T the temperature and E_{zl} is the energy separating the lowest Stark level of the lower manifold and the lower Stark level of the upper manifold (zero line). This relation shows that the absorption and emission are closely related and that a large absorption cross section is then usually associated with a large emission cross section in an ytterbium laser.

The radiative lifetime τ_{rad} is also connected to the emission cross section by the so-called Füchtbauer-Ladenburg equation [DPC+93]

$$A_{21} = \frac{1}{\tau_{rad}} = 8\pi n^2 c \int \frac{\langle\sigma_{em}(\lambda)\rangle}{\lambda^4} d\lambda \tag{2.5}$$

with n the refractive index, c the speed of light and $\langle\sigma_{em}(\lambda)\rangle$ denotes the average emission cross section over the polarization. This equation immediately shows that a large emission cross section and a large bandwidth inevitably lead to a short radiative lifetime.

This also demonstrates that the use of strongly anisotropic crystals, such as the monoclinic double tungstates studied in this thesis, can be very relevant as they allow to somehow bypass these fundamental limitations. The favorable features, extremely high and broad cross sections for example, can then be concentrated in one polarization.

Now that the principal connections between these spectroscopic parameters are underlined, the desired spectroscopic properties for efficient laser operation in the continuous-wave and short pulse operation regimes can be treated.

Stark Splitting

In general, a strong Stark splitting is desirable as the thermal population of the lower laser level is then reduced, denoting less reabsorption of the emitted photons and lower laser threshold. It also indicates that a larger tunability potential and, ultimately, that the generation of shorter pulses is possible. On the other hand, the emission bandwidth has to be very smooth to allow the generation of ultrashort pulses and a large Stark splitting could introduce some significant modulation in the emission spectrum that would prevent the use of the whole spectral range.

Radiative lifetime

A long upper-state lifetime in a laser gain medium means that a significant population inversion can be maintained with a relatively low pump power. As we will see later in equation 6.11, the radiative lifetime is inversely proportional to the laser threshold. A long radiative lifetime is then usually favorable but is, however, generally related to stronger Q-switching instabilities in the mode-locked regime, see section 6.5 [5]. The suppression of such undesired instabilities can then be very critical in rare-earth-doped gain media.

Interaction cross sections

High absorption and emission cross sections are typically advantageous in the continuous-wave and mode-locked regime. A high absorption cross section denotes the potential for efficient absorption of the pump beam and thus allows the introduction of thin active elements where the overlap of the pump and laser beam becomes less critical. A high emission cross section is also attractive to decrease the laser threshold and to obtain a high slope efficiency at moderate pump intensity as we will see. Broad linewidths are as well advantageous, for uncritical diode pumping, tuning and short pulse generation. A broad absorption band means relaxed requirement on the emission spectrum of the laser diode while a broad emission band permits the generation of shorter pulses. Nevertheless, homogenous and inhomogenous broadening mechanisms are usually connected with a decrease of the interaction cross sections.

5. Actually, the relation described in this thesis that express the tendency for Q-switching in the mode-locked regime does not include directly the radiative lifetime. However, it can be seen from the Füchbauer-Ladenburg relation that a long radiative lifetime is generally connected to a low emission cross section, denoting a significant tendency for Q-switching instabilities.

As one can see, the spectroscopic characteristics are strongly interconnected and a balance between desirable but incompatible features has to be found. The optimum features are also strongly influenced by the desired mode of operation of the laser, in the present work continuous-wave or mode-locked regime. Finally, optimal spectroscopic properties are often incompatible with good thermo-mechanical properties that are desired for good thermal management. In particular, the use of strongly anisotropic crystals such as the monoclinic double tungstates permits to have unique spectroscopic properties with extremely high and broad absorption and emission cross sections. They are, nevertheless, related to strong anisotropy of the mechanical, thermal and optical properties. The implementation of such crystals is therefore particularly challenging and often requires special design of the active element and of the laser resonator.

The other compounds that will be extensively treated in this thesis are the tetragonal sodium double tungstates, which are characterized by an extremely broad emission cross section that is very suitable for ultrashort pulse generation. This specific feature results from local structural disorder that causes an important inhomogenous broadening of the linewidths. The structural disorder is, as might be expected, associated with an important drop of the thermal conductivity.

But before we proceed to a detailed description of these two classes of compounds, let us identify the fundamental equations that describe the operation of Yb-doped lasers.

2.4 Equations and modeling

In this section, the principal equations describing the behavior of Yb lasers will be derived. In particular, it is possible to define some figure of merit based on the spectroscopic properties of Yb doped materials and to understand better the influence of important parameters in order to obtain efficient laser operation.

Rate equations

In this first subsection, the principal rate equations will be derived. In general, the notations and derivations used by Klopp [Klo06] will be extensively employed here. For more details, the reader is advised to refer to his work. It is first important to express the relation connecting the absorption and emission cross sections obtained by spectroscopic measurement at the pump and laser wavelength, $\sigma_{abs,P,L}$ and $\sigma_{em,P,L}$, with the transition cross sections of the individual sublevels. The relations connecting both can be written

$$\begin{aligned} f_{li}\sigma_P &= \sigma_{abs,P} \\ f_{uj}\sigma_P &= \sigma_{em,P} \\ f_{li}\sigma_L &= \sigma_{abs,L} \\ f_{uj}\sigma_L &= \sigma_{em,L} \end{aligned} \tag{2.6}$$

where f_{li} and f_{uj} are the Boltzmann occupation factors of the Stark levels i and j of the lower and upper levels, respectively.

It is also useful to introduce the inversion parameter β defined as

$$\beta = \frac{N_2}{N} \quad \text{and} \quad N_1 = (1-\beta)N \qquad \text{with the total active ion density } N = N_1 + N_2 \tag{2.7}$$

and the effective gain cross section $\sigma_{gain}(\lambda)$ at the pump or laser wavelength as:

$$\sigma_{gain} = \beta\sigma_{em} - (1-\beta)\sigma_{abs} \tag{2.8}$$

The transition rates concerning the pump, laser and spontaneous decay including the previously defined parameters can now be indicated. In this analysis, amplified spontaneous emission and reabsorption of the fluorescence are not considered.

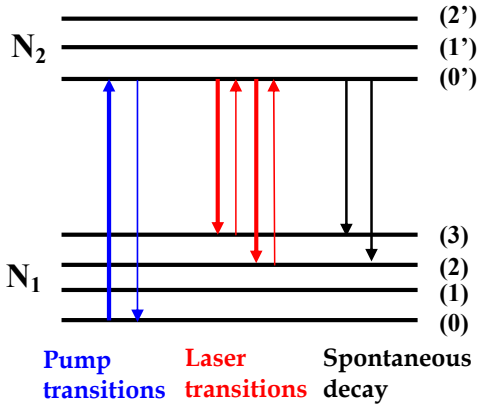

Figure 2.4: Simplified scheme of the principal transitions occurring in an Yb laser

Pump transition rate:
The effective pump rate R_P is given by the absorption rate R_{abs} reduced by the reemission rate R_{reem}:

$$\begin{aligned} R_P = R_{abs} - R_{reem} =& N_1\sigma_{abs,P}\frac{I_P}{h\nu_P} - N_2\sigma_{em,P}\frac{I_P}{h\nu_P} \\ =& N\left[(1-\beta)\sigma_{abs,P} - \beta\sigma_{em,P}\right]\frac{I_P}{h\nu_P} = -N\sigma_{gain,P}\frac{I_P}{h\nu_P} \end{aligned} \tag{2.9}$$

Laser emission rate:
Following the same procedure, the effective laser emission rate R_L is expressed as a contribution of the stimulated emission rate R_{em} reduced by the reabsorption rate R_{reabs}:

$$\begin{aligned} R_L = R_{em} - R_{reabs} =& N_2\sigma_{em,L}\frac{I_L}{h\nu_L} - N_1\sigma_{abs,L}\frac{I_L}{h\nu_L} \\ =& N\left[\beta\sigma_{em,L} - (1-\beta)\sigma_{abs,L}\right]\frac{I_L}{h\nu_L} = N\sigma_{gain,L}\frac{I_L}{h\nu_L} \end{aligned} \tag{2.10}$$

Fluorescence spontaneous decay:
Finally, the radiative decay rate R_{rad} as well as the non-radiative decay rate R_{nr} contribute to the spontaneous decay R_{spd} of the fluorescence:

$$R_{spd} = R_{rad} + R_{nr} = \frac{N_2}{\tau_{rad}} + \frac{N_2}{\tau_{nr}} = \frac{N_2}{\tau_f} = \frac{\beta N}{\tau_f} \tag{2.11}$$

with the fluorescence lifetime τ_f defined as $\frac{1}{\tau_f} = \frac{1}{\tau_{rad}} + \frac{1}{\tau_{nr}}$

By finally combining these contributions together, one finds a general laser rate equation system for the population density in the upper and lower laser levels.

$$\begin{aligned}\frac{dN_2}{dt} &= -\frac{dN_1}{dt} = R_P - R_L - R_{spd} \\ &= \sigma_{em,L}\frac{I_L}{h\nu_L}N_2 + \sigma_{em,P}\frac{I_P}{h\nu_P}N_2 - \sigma_{abs,L}\frac{I_L}{h\nu_L}N_1 - \sigma_{em,P}\frac{I_P}{h\nu_P}N_1 + \frac{N_2}{\tau_f} \\ &= -N\sigma_{gain,P}\frac{I_P}{h\nu_P} - N\sigma_{gain,L}\frac{I_L}{h\nu_L} - \frac{\beta N}{\tau_f}\end{aligned} \tag{2.12}$$

Due to the small cross section for stimulated emission in solid state lasers, typical intracavity pulse energies are much smaller than the saturation energy of the gain in the mode-locking regime. Therefore, the effect of gain saturation due to one pulse can be neglected so that the gain saturates with the average power only. In gain media which have large gain cross sections like semiconductors and dyes, typical intracavity pulse energies may become large enough to saturate the gain considerably in a single pass. As a result, when Yb-doped laser sources are considered, continuous-wave (CW) and mode-locked (ML) operations are related to the same fundamental rate equations.

This steady state equation can be written in the form:

$$\frac{dN_2}{dt} = -\frac{dN_1}{dt} = -N\sigma_{gain,P}\frac{I_P}{h\nu_P} - N\sigma_{gain,L}\frac{I_L}{h\nu_L} - \frac{\beta N}{\tau_f} = 0 \tag{2.13}$$

This general relation contains three parameters, the inversion parameter β, which is also a hidden parameter of the gain cross section σ_g, the pump intensity I_P and the laser intensity I_L. This equation can give in particular a relation between the inversion parameter β and the pump and laser intensities I_P and I_L so that the inversion parameter in the steady state regime can be rewritten as:

$$\beta = \frac{\sigma_{em,P}\frac{I_P}{h\nu_P} + \sigma_{abs,L}\frac{I_L}{h\nu_L}}{(\sigma_{abs,P} + \sigma_{em,P})\frac{I_P}{h\nu_P} + (\sigma_{abs,L} + \sigma_{em,L})\frac{I_L}{h\nu_L} + \frac{1}{\tau_f}} \tag{2.14}$$

Moreover, β_{min} denoting the minimum value of the inversion parameter β to reach the transparency of the active medium at a particular wavelength can be derived by setting $\sigma_g = 0$ in equation 2.8.

$$\beta_{min} = \frac{\sigma_{abs}}{\sigma_{abs} + \sigma_{em}} \tag{2.15}$$

Let us finally consider some important values of the intensity. An important value is the saturation intensity I_{sat} defined as the optical intensity of an input signal which, in the steady state, leads to reduction of the gain to one half of its small-signal value for an infinitesimally thin sample. The saturation intensity can be defined at both the laser and pump wavelength as:

$$I_{sat,P} = \beta_{min,P}\frac{h\nu_P}{\sigma_{abs,P}\tau_f} = \frac{h\nu_P}{(\sigma_{abs,P}+\sigma_{em,P})\tau_f} \tag{2.16}$$

and

$$I_{sat,L} = \beta_{min,L}\frac{h\nu_L}{\sigma_{abs,L}\tau_f} = \frac{h\nu_L}{(\sigma_{abs,L}+\sigma_{em,L})\tau_f} \tag{2.17}$$

We have now derived the rate equations as well as the principal parameters such as the inversion parameter β and the saturation intensities $I_{sat,P}$ and $I_{sat,L}$ that are used to understand and model the quasi-three level laser. Let us then consider some relations that express the laser threshold and the output intensity.

Laser Threshold

For the calculation of the threshold, one uses the condition that the population inversion has to be sufficient so that the round-trip gain averaged over the cavity mode equals the round-trip loss. In the low loss approximation and considering Gaussian beams with no diffraction, the spatial integration [FB87, Ris88, Klo06] gives a well known expression for the threshold

$$\begin{aligned} P_{th} = &\ \beta_{min}\frac{Nl_c h\nu_P}{\tau_f}\frac{\pi}{2}(w_P^2+w_L^2)\left(1+\frac{L_i+T_{OC}}{2Nl_c\sigma_{abs,L}}\right) \\ = &\ \frac{h\nu_P}{\tau_f(\sigma_{em,L}+\sigma_{abs,L})}\frac{\pi}{4}(w_P^2+w_L^2)\left(L_i+T_{OC}+2Nl_c\sigma_{abs,L}\right) \end{aligned} \tag{2.18}$$

where w_P and w_L are the waists of the pump and laser mode respectively, T_{OC} is the transmission of the output coupler at the laser wavelength and L_i is the term taking into account the presence of extra losses. As one can see, a long upper state lifetime as well as a large emission cross section at the laser wavelength are desired for low threshold. Moreover, it is important to minimize the pump and laser mode area inside the crystal. Finally, it is seen that the thermal population in a quasi-three level system constitutes an additional loss term that has to be overcome to reach threshold. The above equation can be further generalized with spatial distribution functions taking into account the effect of overlap of non-Gaussian pump and laser beams [TTB97]. In this case, the equation for the threshold becomes:

$$P_{th} = \frac{h\nu_P(V_{eff}/l_c)}{2\tau_f(\sigma_{abs,L}+\sigma_{em,L})}(L_i+T_{OC}+2Nl_c\sigma_{abs,L}) \tag{2.19}$$

where the quantity V_{eff} is the effective mode volume defined by

$$V_{eff} = 1/\iiint_{crystal} r_P(x,y,z)\phi_0(x,y,z)\,dV \tag{2.20}$$

with $r_P(x,y,z)$, the spatial distribution of the pump photons and $\phi_0(x,y,z)$, the spatial distribution of the laser photons. As we will see in subsequent chapters, this expression can be very useful to compare the laser thresholds for several different configurations.

Output laser intensity and slope efficiency

As the reabsorption losses depend to a great extent on the spatial overlap of the pump and laser beams, precise analysis of the efficiency of quasi-three level lasers turns out to be critical. No analytical solutions taking into account this spatial dependence as well as pump and laser saturation do exist. Considering both the pump and laser beams as plane waves can considerably simplify the problem. This approach should then no longer be considered as an optimum model of a quasi-three level laser especially when the crystal is getting very thick or when the pump beam shows an important divergence. It, however, helps to derive important information about the spectroscopic and resonator parameters influencing the laser efficiency. Such procedure was proposed by Bourdet [Bou00, Bou01] and can be adapted to various pump configurations [BB06]. It will be presented here and adapted to longitudinally pumped Yb-crystals in a single pass configuration. Let us now consider the equations that describe the pump intensity I_P and laser intensity I_L inside the resonator:

$$\frac{dI_L^\epsilon}{dz} = \epsilon\sigma_{gain,L}NI_L^\epsilon \quad \text{and} \quad \frac{dI_P^\epsilon}{dz} = -\epsilon\sigma_{gain,P}NI_P^\epsilon \tag{2.21}$$

where $\epsilon = \pm$ refers to the direction of propagation of the pump and laser wave. These propagation waves are connected together by the equations:

$$\frac{dI_L^+}{I_L^+} = -\frac{dI_L^-}{I_L^-} \quad \text{and} \quad \frac{dI_P^-}{I_P^-} = -\frac{dI_P^-}{I_P^-} \tag{2.22}$$

By developing these equations as in [Bou01], one finds an expression for the output laser intensity I_{las} versus the pump intensity at the entrance face of the crystal $I_P^+(0)$, both intensities being normalized to the relevant saturation intensities, in a longitudinally pumped two mirror cavity in single pass pump configuration:

$$I_{las} = A\left(\frac{\sigma_{abs,L}+\sigma_{em,L}}{\sigma_{abs,P}+\sigma_{em,P}}(1-\Gamma)I_P^+(0) - \sigma_{abs,L}Nl_c + \ln\sqrt{R_1R_{OC}}\right) \tag{2.23}$$

where Γ is the transmission coefficient of the crystal at the pump wavelength in lasing condition, l_c is the length of the crystal, R_1 and R_{OC} are the reflection coefficients at the laser wavelength of the incoupling mirror and the output coupler, respectively, and A is a parameter depending only on the resonator properties that is defined by:

$$A = \frac{(1-R_{OC})\sqrt{R_1}}{(1-\sqrt{R_1R_{OC}})(\sqrt{R_1}+\sqrt{R_{OC}})} \tag{2.24}$$

Optimum crystal length

From this equation, it is possible to derive an optimum transmission of the crystal, i.e. a transmission that will maximize the output laser intensity for a given incident pump intensity. The corresponding optimum crystal length $l_{c,opt}$ can be written as

$$l_{c,opt} = \frac{-1}{\beta_{min,P}-\beta_{min,L}}\ln\left[\left(\sqrt{R_1R_{OC}}\right)^{\frac{1}{N(\sigma_{abs,L}+\sigma_{em,L})}}\left(\frac{\beta_{min,L}}{\beta_{min,P}-\beta_{min,L}}\frac{1}{2I_P^+(0)}\right)^{\frac{1}{N(\sigma_{abs,P}+\sigma_{em,P})}}\right] \tag{2.25}$$

As one can see, the optimum crystal length depends on a lot of variables including spectroscopic parameters such as the transition cross sections, the ytterbium ion concentration and also on the parameters of the laser cavity and the incident pump intensity. This is characteristic of quasi-three level lasers and renders accurate modeling and optimization of such lasers difficult.

However, by assuming that one works with the ideal crystal length and by replacing its transmission coefficient Γ in the equation 2.23, one obtains a final equation for the output laser intensity I_{las} as a function of the incident pump intensity I_{P0} that does not depend on the ytterbium concentration N anymore

$$I_{las} = A\frac{\lambda_P}{\lambda_L}\left[I_{P0} - \frac{I_{min}}{2}\left(1 - \ln\frac{I_{min}}{2I_{P0}}\right) + \frac{I_{min}}{2}\frac{\sigma_{abs,P}}{\sigma_{em,L}}\ln\sqrt{R_1 R_{OC}}\right] \tag{2.26}$$

with I_{min} being the minimum pump intensity required for achieving crystal transparency at the laser wavelength when pumped in a single pass, defined as:

$$I_{min} = \frac{\beta_{min,L}}{\beta_{min,P} - \beta_{min,L}} I_{sat,P}. \tag{2.27}$$

Finally, by dividing the above equation by the incident pump intensity, a general relation for the optical efficiency η is found

$$\eta = A\frac{\lambda_P}{\lambda_L}\left[1 - \frac{I_{min}}{2I_{P0}}\left(1 - \ln\frac{I_{min}}{2I_{P0}}\right) + \frac{I_{min}}{2I_{P0}}\frac{\sigma_{abs,P}}{\sigma_{em,L}}\ln\sqrt{R_1 R_{OC}}\right] \tag{2.28}$$

Let us then further detail this last relation. It can be shown easily that for R_1 tending to 1 and high reflection of the output coupler R_{OC}, the parameter A tends to 1 while the last term in the parentheses of the upper equation tends to zero. In this approximation, considering planar waves only, one obtains a the maximum theoretical optical efficiency η_{max}, which no more depends on the resonator parameters but solely on the spectroscopic parameters

$$\eta_{max} = \frac{\lambda_P}{\lambda_L}\left[1 - \frac{I_{min}}{2I_{P0}}\left(1 - \ln\frac{I_{min}}{2I_{P0}}\right)\right] \tag{2.29}$$

In particular, at low incident pump power, the maximum theoretical optical efficiency is mainly set by I_{min}, the minimum pump intensity required for achieving transparency at the laser wavelength. On the other hand, at high incident pump power, the maximum theoretical optical efficiency tends to the value $\eta_{red} = \frac{\lambda_P}{\lambda_L}$ as seen in Fig. 2.5.

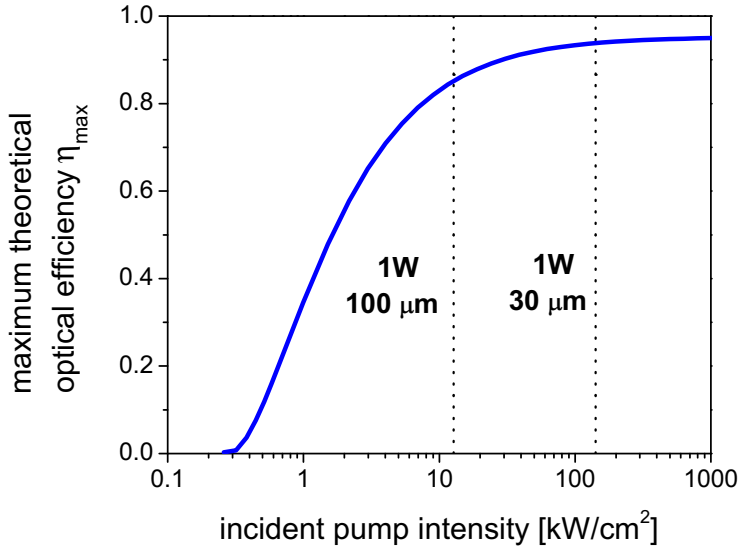

Figure 2.5: Maximum theoretical optical efficiency η_{max} as defined in equation 2.29 for Yb:KLu$(WO_4)_2$ as a function of the incident pump intensity. The two vertical lines indicate the incident pump intensity achieved by focusing 1 W of pump power on a spot diameter of 100 μm and 30 μm. The spectroscopic data of Yb:KLuW used for this plot will be presented in detail in chapter 3.

From this evaluation, one can understand better the fundamental parameters that allow efficient laser operation and it can be used as a spectroscopic figure of merit to compare the different hosts (see section 3.3). It reveals the principle importance of keeping a high pump intensity along the whole crystal length so that laser efficiency close to the upper limit given by the ratio of the pump wavelength to the laser wavelength is allowed. It will also help to maintain a high spatial overlap between the pump and laser modes, an effect that is not considered in this upper analysis. When high pump intensity is maintained, it is also important to use a host that has potentially a maximum efficiency and therefore presents a minimum difference between the pump and laser wavelength. As we will see in the next chapters, the double tungstates are ideally suited for this purpose.

In order to maintain a high pump intensity, two interesting options can be considered. On the one hand, the development of waveguiding structures that avoid diffraction effects and therefore help to maintain a high pump intensity along the entire crystal length (see section 4.3). On the other hand, it can be interesting to reduce the crystal dimension to a very thin layer so that diffraction into the active layer is limited (see section 4.2). However, the use of such thin active disks has usually to be correlated with higher doping levels in order to achieve sufficient absorption or with the implementation of rather complicated resonator geometries that allow multiple pass pumping.

Chapter 3

The Double Tungstates

The aim of the first part of this chapter is to present the method of synthesis as well as the principal spectroscopic and optical properties of some relevant Double Tungstates (DTs). Double tungstate compounds have the general formula $AT(WO_4)_2$, where A is a monovalent alkali-metal cation and T a trivalent metal or rare-earth cation. The large variety of possible substitutions leads to non-equivalent crystalline structures and very different properties. This work will focus on the two most promising structures of DT crystal hosts for laser applications, the monoclinic potassium double tungstates, KREW (RE: rare earth) with RE= Y, Gd, Lu and the tetragonal sodium tungstates, NaREW with RE=Bi, Y, La, Gd and Lu as passive (optically inert) compounds. The different structures of these two DT groups lead to important distinctions in the growth method, optical, spectroscopic and thermo-mechanical properties that will be underlined.

The measurements presented in the first two sections of this chapter (section 3.1 and 3.2) have been performed mostly at the Universitat Rovira I Virgili (URV), Spain and at the Materials Science Institute of Madrid (ICMM), Spain for the monoclinic and tetragonal DTs, respectively. Although not directly within the scope of my work, these data were published in joint papers and will be continuously used throughout this thesis to derive important informations about stability and efficiency in the continuous-wave and mode-locked regime. In the second part of this chapter (section 3.3), the presented data in these first sections are used to compare the double tungstate structures with well established or new promising compounds such as YAG, sesquioxide, vanadate or CALGO crystals.

3.1 The Monoclinic Double Tungstates

The monoclinic potassium double tungstates are very well known as hosts for rare earth dopants. In particular, when doped with Yb^{3+}, they exhibit one of the largest absorption and emission cross sections together with broad linewidths. Moreover, the possibility to reach high doping concentrations without substantial fluorescence quenching and relatively good thermal properties make them especially suitable for both efficient high power lasers and short-pulse generation.

The potassium double tungstates $KY(WO_4)_2$ (KYW), $KGd(WO_4)_2$ (KGdW), and $KLu(WO_4)_2$ (KLuW) are isostructural, crystalizing in the monoclinic structure with space group $C2/c$. The crystal growth method as well as many properties like the thermal conductivity, hardness, opti-

cal transparency and refractive index are similar in these three hosts. Although it is less spread, $KLu(WO_4)_2$ has, however, the highest potential for Yb doping because of the close ionic radii and masses of Yb and Lu. This brings some advantages for high doping levels as the defect formation stays minimal. For composite structures, a high quality of the interface can be preserved thanks to the close lattice parameters of the doped and undoped layers. Finally, for Yb doping, a minimal reduction of the thermal conductivity is expected. The following sections will then focus on the KLuW compound and occasionally, when it is required, differences with the other two monoclinic double tungstates KYW and KGdW will be described.

3.1.1 Synthesis and structure

It is known that monoclinic potassium double tungstates transform upon heating into different phases. The monoclinic KLuW, for example, transforms into an orthorhombic phase and, upon further heating into a trigonal form. This polymorphism excludes standard growth process directly from the melt such as the Czochralski (Cz) method that allows the relatively quick growth of large boules of single crystals.

The Top Seeded Solution Growth (TSSG) method

Monoclinic potassium double tungstate crystals have to be grown from solutions that will decrease the temperature of growth and therefore avoid problems related to their polymorphism. By properly decreasing the temperature, the flux formed by the solvent and solute becomes supersaturated, and the solute excess precipitates, either with spontaneous nucleation, or on a seed, as for the Top Seeded Solution Growth (TSSG) method. The main advantage in the use of a solvent is that the growth takes place in a supersaturated solution at lower temperatures than those required for growing directly from the melt. The selected solvent ($K_2W_2O_7$), is the standard solvent used for monoclinic DTs, with the basic advantages being the absence of foreign ions and the low melting temperature. The best seed orientation to grow KREW crystals by the TSSG method is parallel to the crystallographic b direction of the monoclinic phase. It allows a faster growth, with high quality.

The obtained crystals have a specific morphology with external manifestation of the faces {110}, {111}, {010} and {310} as it can be seen in figure 3.1. The external manifestation of the {010} face in these materials is important as a structural reference in order to prepare samples for characterization purposes or laser applications. Typical sizes and weights of the grown crystals are about one cubic centimeter and several grams.

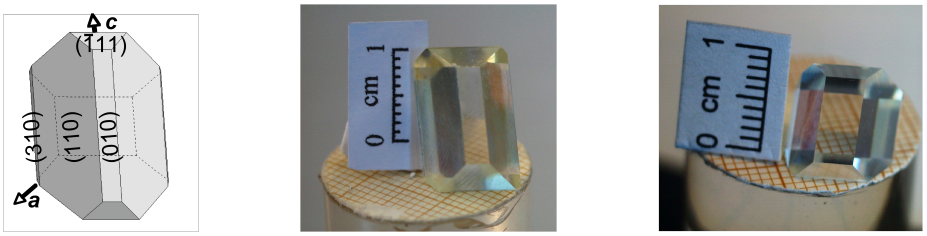

(a) (b) (c)

Figure 3.1: Morphology (a) and single crystal of undoped (b) and 5 at. % Yb-doped (c) KLuW. Data and pictures obtained from the URV, Spain [PPM+07].

Crystal structure

The structure of the monoclinic KLuW was studied by single crystal X-ray diffraction (XRD). KLuW has the structure of KYW, as the other potassium double tungstates of the heavier lanthanides starting from $KSm(WO_4)_2$ (KSmW) for which the unit cell parameters and hence the interatomic distances tend to decrease with the Ln atomic number.

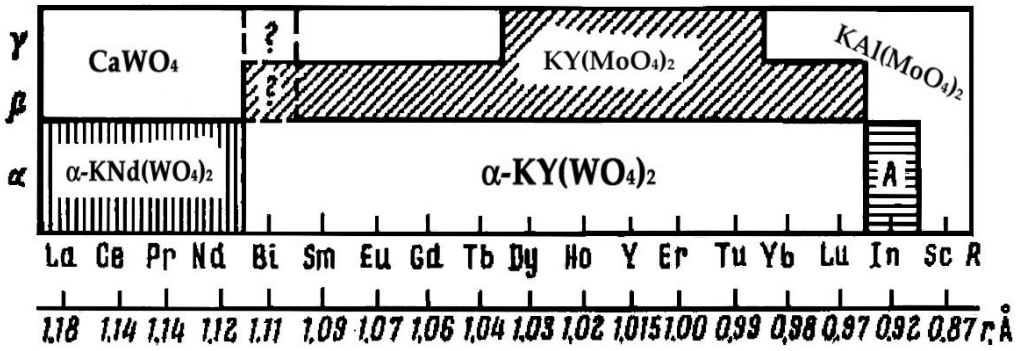

Figure 3.2: Diagram illustrating the $KT(WO_4)_2$ structure types as a function of the T^{3+} ion radius and temperature. $CaWO_4$, tetragonal $I4_1/a$ scheelite. α-$KNd(WO_4)_2$ type monoclinic $C2/m$. α-$KY(WO_4)_2$ type, monoclinic $C2/c$. $KY(MoO_4)_2$ type, orthorhombic $Pbcn$. A= $KIn(MoO_4)_2$ type, orthorhombic $Pnam$. $KAl(MoO_4)_2$ type, $P^{-}3mi$, from [KKK75]

The potassium DT compounds studied belong to the monoclinic system, with the space group C2/c. For KLuW, the unit cell parameters are found to be a=10.576(7) Å, b=10.214(7) Å, c= 7.487(2) Å and β=130.68(4)° for a corresponding volume V of 613.3(6) $Å^3$. The trivalent cation is eight-fold coordinated by oxygen atoms, forming a distorted square antiprism. Its site symmetry is C2 (4e Wyckoff notation), and the doping ions are accommodated in this unique site.

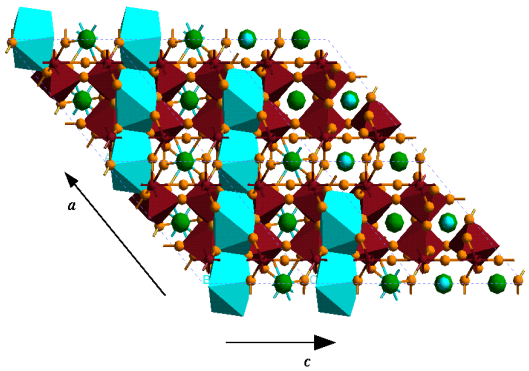

Figure 3.3: Projection of the KLuW structure parallel to the b crystallographic direction [010]. Obtained from the URV, Spain [PPM+07].

This monoclinic symmetry is also maintained for high doping concentration up to the stoichiometric KYbW compound [PSM+02]. For KLuW, the variation of the unit cell parameters with doping is studied and an increase of the unit cell parameters a, b, c is noticed, as expected from the larger ionic radii of Yb in comparison to Lu, while the angle β remains basically constant. The variation of the unit cell parameters with doping is actually found to be minimum for the KLuW compound due to the close ionic radii and masses of Yb and Lu. Thus KLuW is the ideal host for the development of highly doped crystals with low defect probability where the dopant only weakly affects the thermal conductivity, and of composite structures involving both highly doped and undoped layers as the lattice mismatch at the interface is kept minimum (see section 4.2). The distances between Lu-Lu pairs are also important because they affect the energy transfer between the dopant ions. The shortest Lu-Lu distance is in the LuO8 chain parallel to the [101] direction and amounts to 4.045(3) Å. Although the minimum distance between two trivalent ions is found to be slightly smaller for KLuW than for KYW or KGdW, this distance remains in monoclinic DTs substantially larger than in most other hosts keeping the energy transfer as low as possible.

Thermal properties

Two parameters concerning the thermal properties will be shortly discussed here. First, the thermal conductivity, which should be as high as possible to allow high power diode pumping without damaging the crystal and, secondly the linear thermal expansion coefficients. Due to their low symmetry, the monoclinic potassium DTs KREW show strongly anisotropic thermal properties.

The principal thermal conductivity coefficients κ of undoped KLuW at room temperature are very similar to the KYW and KGdW compounds and amount to κ_1= 3.09 $Wm^{-1}K^{-1}$, κ_2=2.55 $Wm^{-1}K^{-1}$, κ_3=4.40 $Wm^{-1}K^{-1}$. This corresponds to an average value of $\sim$ 3.35 $Wm^{-1}K^{-1}$. The orientation of the conductivity ellipsoid is such that one of its axes coincides with the b crystallographic axis and it rotates about this axis when the temperature changes [PPM+07].

For a laser material, the linear thermal expansion coefficients and especially their anisotropy are also important. The linear thermal expansion coefficient in a given crystallographic direction is $\alpha = (\Delta L\ /\Delta T)/L_{RT}$, where L_{RT} is the initial parameter at room temperature, and ΔL is the modification of this parameter when the temperature is changed by ΔT. By diagonalizing the obtained matrix one can obtain the linear thermal expansion tensor in the eigenframe $X_1X_2(//b)X_3$, see fig. 3.4.

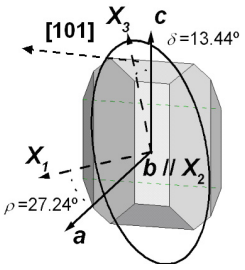

Figure 3.4: Thermal expansion ellipsoid of KLuW. Obtained from the URV, Spain [PPM+07].

Comparing with previous data obtained for KGdW, KYW, KErW and KYbW, KLuW has a similar angle between the X_3 and the c axes. On the other hand, if the ratio α_{33}/α_{11} is considered as a measure of the linear thermal expansion anisotropy in the face {010} one can conclude that this anisotropy decreases along the KLnW series. Thus, KLuW is the host with the lowest thermal anisotropy in the {010} plane. This lowest anisotropy means reduced probability of cracking for thermal reasons when KLuW crystals are used as laser active elements.

3.1.2 Optical and spectroscopic characterization

Optical Properties

The transmission of KLuW is shown in figure 3.5. For this measurement a 1-mm thick b-cut plate was used. At an absorption level of 1 cm^{-1}, the transparency of KLuW extends from 365 to 5110 nm.

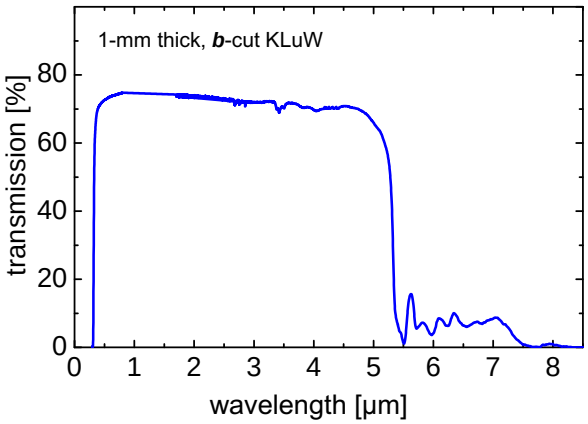

Figure 3.5: Unpolarized transmission of undoped KLuW. Measured at the URV, Spain [PPM+07].

The monoclinic phase of KLuW belongs to the $2/m$ point group. Hence, KLuW is a biaxial crystal with inversion centre. The three orthogonal principal optical axes x, y, z are traditionally labeled for monoclinic crystals as N_p, N_m, N_g. They are defined by the ratio of the corresponding refractive indices $n_x < n_y < n_z$ or $n_p < n_m < n_g$. In monoclinic crystals, one of the principal optical axes coincides with the 2-fold symmetry axis (the crystallographic b-axis). In the case of KYW, KGdW and KLuW this is N_p. The other two principal optical axes lie in the $a - c$ plane. Their orientation was determined at 632.8 nm with two crossed Glan-Taylor polarizers. Figure 3.6 shows the orientation of the optical ellipsoid with respect to the morphology and the crystallographic frame (both frames abc and $N_pN_mN_g$ are right-handed).

The principal optical axis N_g is located at 18.5° with respect to the c crystallographic axis and N_m is located at 59.2° with respect to the a crystallographic axis, Fig. 3.6. These angles are known to vary slightly for other monoclinic potassium double tungstates and, in the case of KGdW for example, amount to 21.5° and 62.3° respectively.

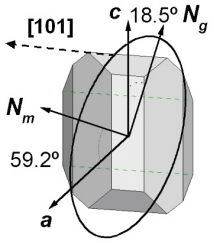

Figure 3.6: Optical ellipsoid of KLuW at room temperature. Obtained form the URV, Spain [PPM+07].

The dispersion curves for the three refractive indices were measured from 410 to 1200 nm by the minimum deviation method using semiprisms. The monoclinic potassium double tungstates are biaxial crystals with significant birefringence. Figure 3.7 shows the experimental values of the refractive indices and the fitted curves using Sellmeier equations containing a single UV pole and an IR correction term, $n^2 = A + B/[1 - (C/\lambda)^2] - D\lambda^2$. The obtained Sellmeier coefficients, valid in the visible and near-IR, are summarized in Table 3.1.

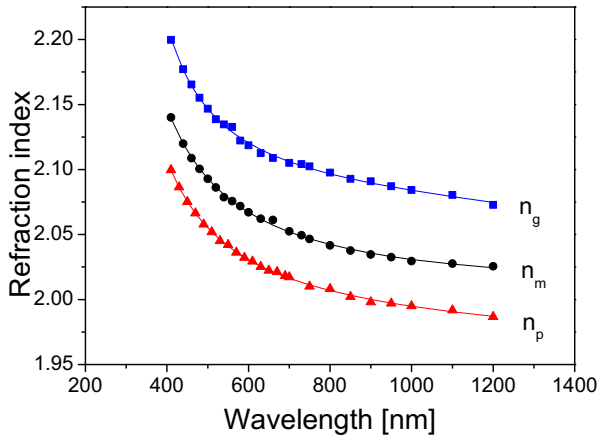

Figure 3.7: Dispersion of the refractive indices of undoped KLuW at room temperature. Measured at the URV, Spain [PPM+07].

	n_p	n_m	n_g
A	3.21749	3.36989	3.58334
B	0.75382	0.74309	0.73512
C [μm]	0.25066	0.26193	0.26700
D [μm^{-2}]	0.05076	0.04331	0.02953

Table 3.1: Sellmeier coefficients of KLuW.

Spectroscopic characterization

Polarized optical absorption measurements of Yb:KLuW at room temperature were performed in order to establish the best conditions for pumping of such lasers and to estimate the absorption and emission cross sections using the reciprocity method [DPC+93]. The optical electronic transition for the $4f^{13}$ configuration of Yb^{3+} can be partially magnetic-dipole allowed and six spectra have to be measured in general for a complete description of such biaxial crystals. However, by neglecting the magnetic dipole-dipole interaction, only three polarizations $E//N_m$, $E//N_p$ and $E//N_g$ have to be investigated.

Figure 3.8 shows the measured absorption and calculated emission cross sections for the single $^2F_{7/2}$-$^2F_{5/2}$ transition of Yb^{3+} in KLuW and the three polarization directions. The maximum absorption cross section at 981.1 nm calculated from the actual Yb^{3+} concentration of 4.5×10^{19} cm^{-3} (0.7 at.% Yb-doped sample) amounts to 1.18×10^{-19} cm^2 for $E//N_m$ (linewidth: 3.6 nm). Both values are very close to those reported for 5 at.% (in the solution) Yb-doped KYW or KGdW [LKM99, KLP+97] and the stoichiometric KYbW (100 at.% Yb) [PSM+02]. The maximum absorption cross section for light polarization parallel to the N_m principal optical axis is about 15 times larger than that of Yb:YAG [DPC+93]. The absorption profiles in Yb:KLuW, for all polarizations, are very suitable for pumping with InGaAs laser diodes operating near 980 nm. The maximum emission cross section in Yb:KLuW amounts to 1.47×10^{-19} cm^2, also for $E//N_m$ at 981.1 nm. This corresponds to the highest emission cross section in any Yb-doped host. Similar to Yb:KYW and Yb:KGdW, the useful polarizations for Yb:KLuW are $E//N_m$ and $E//N_p$ because the emission cross sections for $E//N_g$ are very low.

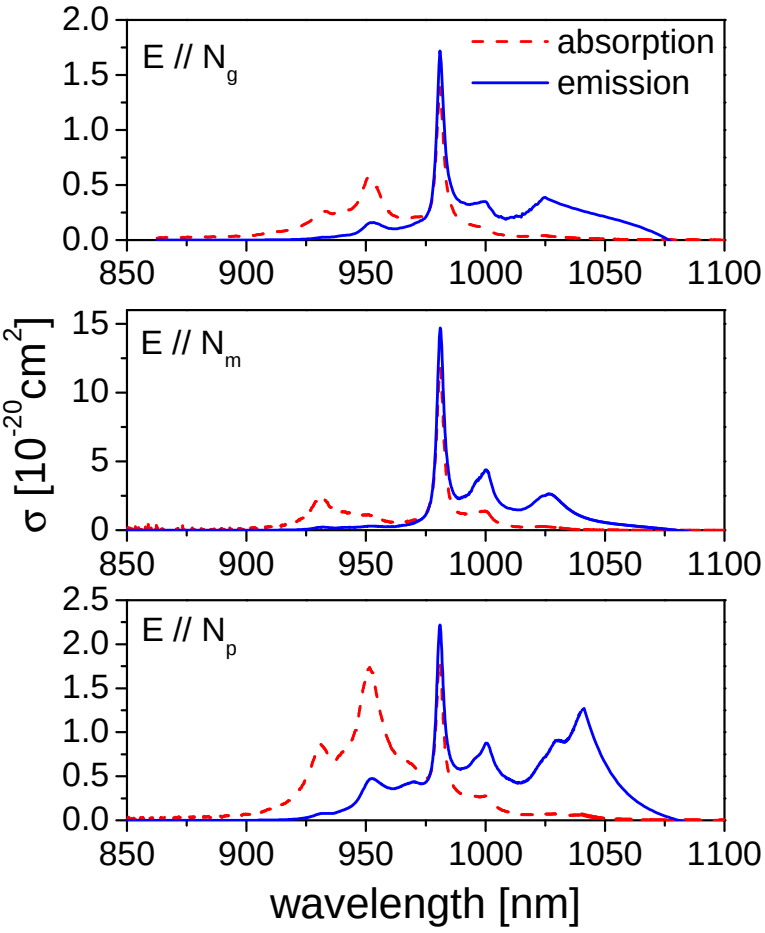

Figure 3.8: Polarized measured absorption (red) and calculated emission (blue) cross-sections of Yb:KLuW. Measured at the URV, Spain [PPM+07].

Polarized absorption and luminescence studies at low temperature (6-10 K) were used to study the Stark splitting of Yb^{3+} in KLuW. The energy position of the four sublevels of the ground state multiplet $^2F_{7/2}$ and the three sublevels of the excited state multiplet $^2F_{5/2}$ of Yb^{3+} in KLuW are obtained from low temperature absorption and emission spectroscopy and can be found in the appendix. The significant Stark splitting of the $^2F_{5/2}$ multiplet is indicative of stronger crystal field in comparison to Yb:KYW and Yb:KGdW [LKM99, KLP+97] which is advantageous for tunable and short pulse laser operation. Figure 3.9 shows emission spectra recorded at room and low temperature and the transitions involved in laser operation.

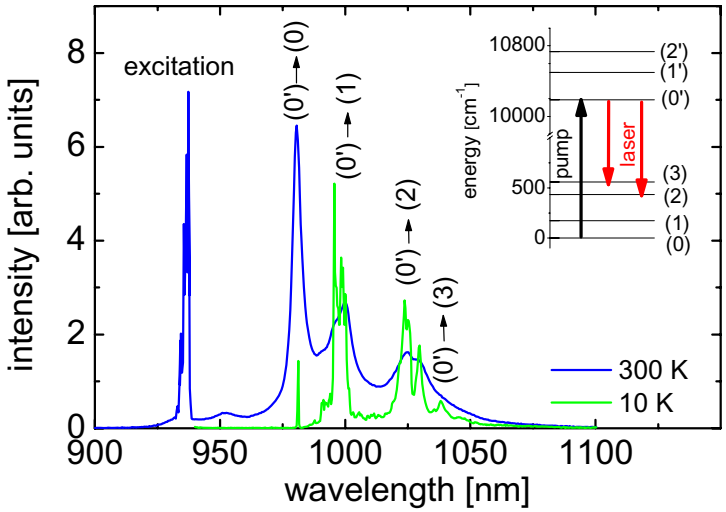

Figure 3.9: Room temperature (blue line) and 10 K (green line) emission spectra recorded with 0.7 at. % Yb-doped KLuW. The inset shows the schematic diagram of the Stark levels and transitions of Yb^{3+}in KLuW. Measured at the URV, Spain [PPM+07].

The fluorescence lifetime is also a fundamental characteristic of a laser gain medium. Special care has to be taken to evaluate its value in the case of Yb. Effectively, in highly doped media, the measured upper state lifetime may be increased by reabsorption of the fluorescence. In particular, radiation trapping due to total internal reflection at the surfaces of the medium strongly increases this effect [SF94]. It is usually avoided by using low doped powder of the substance immersed in a liquid with comparable refractive index, or by the artificial selection with a pinhole of a very small volume where the fluorescence is collected [KFK+07].

Measurements of the fluorescence lifetime performed with a low doped, 0.7 at. % Yb:KLuW resulted in time constant of 375 μs. The use of the pinhole method gave for different samples of 6.8 at. % Yb-doped KLuW values of 299 and 275 μs. Finally, the Yb-fluorescence lifetime was also measured in highly doped epitaxial samples. Compared to the 6.8 at. % doped bulk crystal the lifetime was only slightly lower for a 50 at. % Yb-doped epitaxially grown sample with a value of 224 μs.

3.2 The tetragonal Double Tungstates

Yb-doped tetragonal sodium DTs, $NaT(WO_4)_2$, are of high interest because they offer, as many other hosts, the possibility to be directly pumped by laser diodes and have a low quantum defect that leads to low heat generation. In addition, these tetragonal DTs are characterized by a random distribution of the monovalent Na and trivalent T cations on the same lattice sites. The Yb ion, replacing the trivalent ion of the host, experiences a distribution of crystal fields so that the absorption and emission bands are distinguished by additional inhomogeneous broadening. The larger absorption bandwidth leads to less critical pumping with laser diodes and the larger emission bandwidth denotes higher potential for short pulse generation.

Several different tetragonal DT single crystals were grown and present interesting features. In particular, NaTW with T=Bi, Y, La, Gd and Lu do not exhibit optical absorption bands in the visible and IR so that they are suitable as hosts. In case of Yb-doping, it has been found that the emission cross section increases with decreasing T-ion size, i.e. with increasing crystal field strength. From this point of view, NaLuW would be the preferable host with a ionic radius of Lu that amounts to 0.97 Å [GCH+07]. However, due to incongruent melting, the efficient Czochralski growth method cannot be used for this compound and the TSSG method, which is much slower and produces crystals of smaller sizes has to be used. Contrary to NaLuW, the NaYW compound exhibits congruent melting allowing the use of the Czochralski method and the ionic radius of Y remains rather small (1.015 Å) [GCTS+07]. Following the same idea as in the first section of this chapter, the following section is then focused on the NaYW and the NaGdW compounds, the first exhibiting higher cross sections and the second having been more accurately studied in terms of structure parameters [CSEB+06]. Important differences with other tetragonal sodium hosts will be highlighted when necessary.

3.2.1 Synthesis and structure

Crystal growth

As mentioned in the introduction of this section, NaYW and NaGdW present the advantage that they can be grown by the efficient and industrially matured Czochralski method, while NaLuW has to be grown with the TSSG method. The stoichiometric NaYbW (100% Yb-doped) shows also incongruent melting that sets some limit to the Yb incorporation in NaREW crystals grown with the Czochralski method. With NaGdW for example, crystals doped with up to 20 at.% Yb^{3+} can still be grown free of defects. Seeds with *c*-cut orientation were used and typical dimensions of the pulled boules were 20-25 mm in diameter and 4 to 50 mm in length. In figure 3.10, crystal plates of an undoped NaYW and of a 10 at. % Yb-doped NaLuW are shown.

Figure 3.10: (a) Polished $NaY(WO_4)_2$ (Cz-grown) and (b) 10 at.% Yb-doped $NaLu(WO_4)_2$ (TSSG) plates. Pictures obtained from the ICMM, Spain.

Crystal structure

The unit cell parameters have been obtained from single crystal X-ray diffraction (XRD) measurements and amount to $a = b = 5.2440(5)$ Å, $c = 11.2794(14)$ Å, with a corresponding volume V of 312.93(6) Å^3 for NaGdW. As expected, the unit cell parameters are decreasing with reduced size of the trivalent ion. Thus, the unit cell parameters are $a = b = 5.2014(4)$ Å, $c = 11.2740(12)$ Å, with a corresponding volume V of 305.01(5) Å^3 for NaYW and $a = b = 5.1692(3)$ Å, $c = 11.1832(15)$ Å, with a corresponding volume V of 298.82(5) Å^3 for NaLuW grown by the TSSG method.

Yb:NaTW crystals exhibit at 300 K the noncentrosymmetric $I\bar{4}$ crystalline structure without inversion center. In this symmetry there are two sites, $2b$ and $2d$, shared by Na^+ and T^{3+}/Yb^{3+} cations with specific occupancy factors, see fig 3.11. The T^{3+}/Yb^{3+} occupancy factors are known to vary slightly for different hosts so that their inherent disorder also slightly differs but, in general, the T^{3+}/Yb^{3+} cations occupy preferentially the 2b site, typically 60-65% versus 45-40% in the 2d site for NaGdW. These two crystalline sites have the same S4 local symmetry but different sets of Yb-O distances, i.e., different crystal fields. Moreover, each site is characterized by several environments due to the different Na-T / Yb cationic distributions in the first cationic sphere.

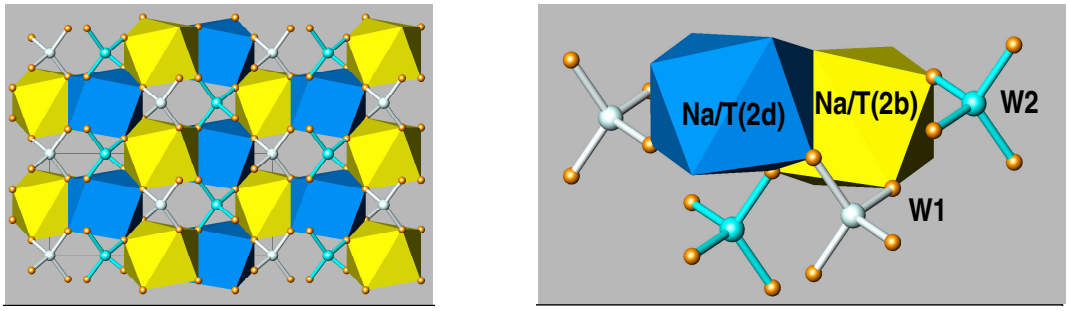

(a) (b)

Figure 3.11: (a) *ac* projection of the tetragonal $I\bar{4}$ crystal structure of $NaT(WO_4)_2$, showing $(Na/T)O_8$ polyhedra from (blue) $2d$(I) and (yellow) $2b$(II) positions and the two kinds of WO_4 tetrahedra. (b) Detail of the environment of edge-sharing $(Na/T)_2O_{14}$ dimeric units. Data obtained from the ICMM, Spain [HCCS+07].

Thermal properties

Due to the strong structural disorder of the NaTW compounds, the thermal features of these crystals are typically inferior in comparison to ordered crystals like YAG, sesquioxides, vanadates or even the monoclinic double tungstate crystals (for a comparison see section 3.3). On the other hand, the thermal conductivity remains still higher than standard glass compounds. The thermal conductivity of NaGdW amounts to 1.096/1.243 $Wm^{-1}K^{-1}$ along the a and c crystallographic axis respectively and is only slightly lower for the NaYW compound.

3.2.2 Optical and spectroscopic characterization

Optical Properties

The optical transparency of the tetragonal sodium double tungstates NaTW typically extends from the effective band gap around 300 nm up to the onset of multiphonon absorption in the IR around 3.6 μm. The refractive indexes, measured by the minimum deviation method using prisms, show that the NaYW and NaGdW crystals are positive uniaxial crystals with a low birefringence (except NaBiW). The measured data of the ordinary (n_o) and extraordinary (n_e) refractive indexes of undoped NaYW at room temperature are shown in figure 3.12. The data can be fitted to a single-pole Sellmeier equation of the type $n^2 = A + B/[1 - (C/\lambda)^2] - D\lambda^2$ with the parameters A, B, C and D given in the Fig 3.12

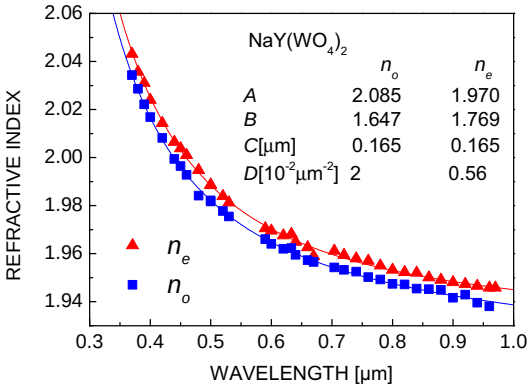

Figure 3.12: Refractive index of undoped $NaY(WO_4)_2$ measured at 300K. The lines represent fits obtained using a single-pole Sellmeier expansion with the parameters summarized in the inset. Data measured at the ICMM, Spain [GCTS+07].

Spectroscopic properties

Low temperature optical absorption and photoluminescence properties have been investigated in order to determine the Yb^{3+} Stark levels. In particular, with a low doped Yb:NaGdW crystal, discrimination of the spectral contributions of Yb^{3+} in the two different sites was possible with the use of the semi-empirical simple overlap model [CSEB+06], which allows to estimate the crystal field parameters from the crystallographic positions of the Gd(or Yb)O_8 coordination polyhedra. The energy of the Stark levels for the two different sites are shown in fig 3.13.

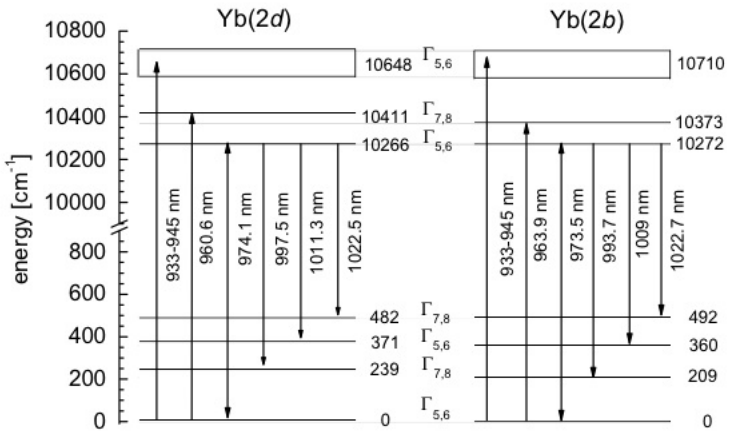

Figure 3.13: Energy level scheme of Yb^{3+} in the 2b and 2d sites of the NaGdW host, taken from [CSEB+06].

With Yb:NaYW crystals, the high Yb concentration in the available samples did not permit the detailed analysis of the spectral distribution of the two individual sites. The energy level scheme was then estimated with an average Yb^{3+} center. The energies of the Stark levels amount then to E($^2F_{7/2}$)=0, 230, 374, 487 cm^{-1} and E($^2F_{5/2}$)=10273, 10397 and 10656 cm^{-1}. As one can see, despite the lack of discrimination of the two sites in Yb:NaYW, the strength of the Stark splitting is very similar in Yb:NaYW and Yb:NaGdW [CSEB+06, GCTS+07]. Similar Stark splitting has also been observed with Yb:NaLuW grown by TSSG [GCH+07].

In a uniaxial crystal, the complete description of the spectroscopic properties requires three polarized optical absorption measurements: α (E⊥c, H⊥c), π (E∥c) and σ (H∥c). The magnetic dipole-dipole interaction is neglected here and the α polarization is then considered to be identical to the σ polarization. From optical absorption coefficient measurement, the absorption cross section σ_{abs} at room can be calculated. With further use of the reciprocity method or the Füchtbauer-Ladenburg method, the emission cross section σ_{em} can be determined for both σ and π polarization. Both are shown in the case of Yb:NaYW in fig 3.14, as well as the measured photoluminescence.

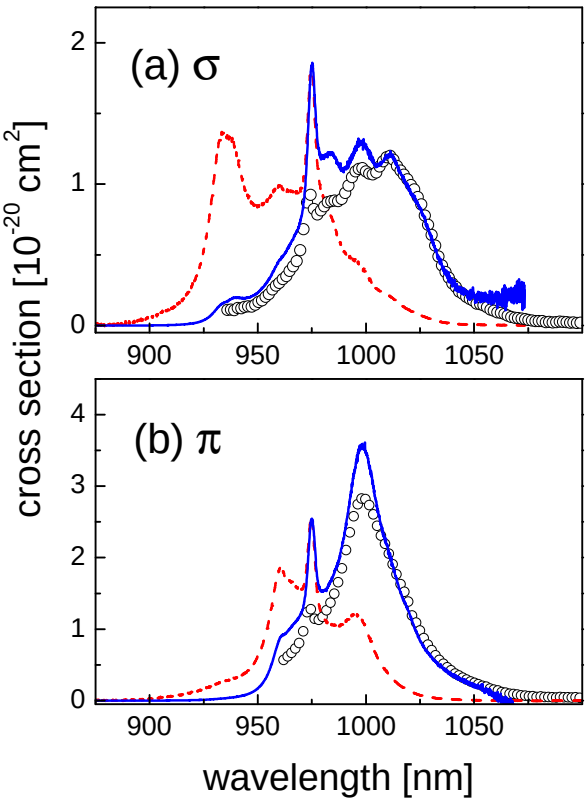

Figure 3.14: Polarized measured absorption (red) and calculated emission (blue) cross sections of Yb-doped NaYW at 300 K. The experimental ${}^2F_{5/2} \rightarrow {}^2F_{7/2}$ fluorescence (circles) obtained with 6.9 at. % Yb-doped NaYW is given for comparison with the emission cross sections, λ_{EXC} = 959 nm. (a) σ-spectra. (b) π-spectra. Data measured at the ICMM, Spain [GCTS+07].

The absorption and emission cross sections of tetragonal sodium double tungstates NaTW are characterized by very broad and smooth lineshapes. This is characteristic of local disorder of these hosts that will induce an inhomogeneous broadening of the spectra. This indicates on the first place relaxed requirement for the wavelength of the high power laser diodes that are used to pump these crystals. Moreover, this also denotes a higher potential for ultrashort pulse generation. In general, one can also observe a tendency to larger cross sections for hosts with smaller lattice parameters, see table 3.2. This is the consequence of the stronger crystal field experienced by the Yb^{3+} ion.

Properties	Cz-NaLaW	Cz-NaGdW	Cz-NaYW	TSSG-NaLuW
$\sigma_{abs}(\sigma/\pi)[10^{-20}$ cm^2],λ [nm]	1.15/1.60, 976	1.36/1.78, 975	1.84/2.52, 975	1.65/2.22, 973.8
$\sigma_{em}(\sigma/\pi)[10^{-20}$ cm^2],λ [nm]	0.94/2.28, 1000	0.75/1.89, 1000	1.3/3.4, 1000	1.4/2.1, 1000

Table 3.2: Absorption and emission cross sections for several tetragonal double tungstates

The Yb-fluorescence lifetime was measured by the pinhole method to minimize radiation trapping effects. The lifetime obtained at 300 K with a 10 at. % Yb-doped NaYW sample was 392 μs. Very similar lifetime have been measured with the Yb:NaGdW and Yb:NaLuW with values of 320 and 350 μs, respectively.

3.3 Comparison of double tungstates with other hosts

In this section, the data provided by the URV and the ICMM, Spain and presented in the previous sections are used to compare the potential of the gain media in the continuous-wave and mode-locked regime. As we will see throughout this work, the potential of a gain medium depends not only on the spectroscopic properties but also on the structural, thermal and optical properties.

3.3.1 Continuous-wave laser operation

At the moment, the market of Yb-doped materials is essentially occupied by the well known Yb:$Y_3Al_5O_{12}$ (Yb:YAG) compound that is characterized by a mature growth technology, a simple cubic structure as well as good spectroscopic and thermal properties. Yb:YAG, however, suffers from several disadvantages that will be detailed in this section. Depending on the application, other hosts can efficiently replace this material.

As we saw in the first chapter of this thesis, the laser characteristics are essentially dominated by the spectroscopic parameters of the different gain media. In particular, a figure of merit taking into account the ground state depletion as well as the laser saturation in the approximation of plane waves was proposed. It allows one to compare the potential of several important families of gain media such as the monoclinic and tetragonal tungstates, the vanadates, the borates, the garnets, the apatite and the sesquioxides compounds. The main spectroscopic characteristics of these hosts are presented in table 3.3 and the maximum theoretical optical efficiency η_{max}, as defined in equation 2.29, is plotted in figure 3.15.

As one can see, the behavior at low incident pump intensity is mainly set by the minimum pump intensity necessary to bleach the crystal at the laser wavelength. In particular, the apatite crystal (Yb:SFAP) with its very long upper state lifetime together with relatively high interaction cross sections provides a high efficiency at low incident pump power. This favorable situation is also found, yet in a reduced way, for the sesquioxides Yb:Sc_2O_3 and Yb:Lu_2O_3. On the other hand, Yb:YAG and Yb:NaYW show relatively pour performance at low incident pump power mainly due to high values of the pump saturation intensity.

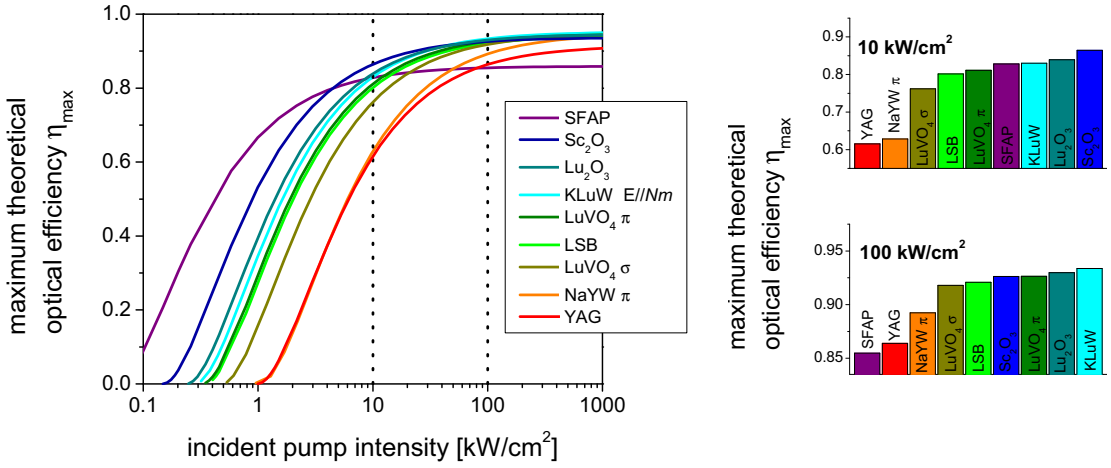

Figure 3.15: Maximum theoretical optical efficiency η_{max} (see equation 2.29) for a set of different prospective hosts. The diagrams on the right report the maximum theoretical optical efficiency for an incident pump intensity of 10 kW/cm^2 and 100 kW/cm^2. The spectroscopic data presented in table 3.3 are used for this comparison.

At high incident pump intensity, the situation turns out to be different with a maximum theoretical optical efficiency basically determined by the ratio of the pump and laser wavelengths. The implementation of gain media showing low quantum defect is then of great importance. One can see that at an incident pump intensity of 10 kW/cm^2, a lot of gain media show similar potential with, however, an advantage for the sesquioxides. At an incident pump intensity of 100 kW/cm^2, the monoclinic double tungstate KLuW (very similar curves can be found also for KGdW and KYW but are not presented here for the sake of simplicity), with its low quantum defect of 4.8% only, surpasses the other gain media. At this level of pump intensity, the apatite crystal Yb:SFAP, as well as the Yb:YAG crystal, are characterized by rather poor potential due to their larger quantum defect of 14% and 9% , respectively.

This tendency is confirmed by another approach based on numerical simulations by Brenier [BB01] taking into account the variation of the pump and laser waists along propagation as well as the variation of the laser intensity along propagation, which leads to very similar results. In this simulation, assuming a pump power of 1 W focused on a spot diameter of 29 μm, the monoclinic double tungstates KYW and KGdW (at that time the KLuW was not introduced) present, as well, the highest potential in terms of slope efficiency and output yield followed by the sesquioxides while YAG and SFAP show lower potential.

Yb-doped gain media .	Structure	λ_P / λ_L [nm]	τ_f [μs]	$\sigma_{abs,P}$ [10^{-20} cm^2]	$\sigma_{em,P}$ [10^{-20} cm^2]	$I_{sat,P}$ [kW/cm^2]	$\sigma_{em,L}$ [10^{-20} cm^2]	$\sigma_{abs,L}$ [10^{-20} cm^2]	$I_{sat,L}$ [kW/cm^2]	I_{min} [kW/cm^2]	Reference
Tungstates											
Yb:KLuW N_m	monoclinic	981 / 1030	320	11.8	14.7	2.39	2.6	0.24	21.2	0.56	[MSG+05]
Yb:NaYW σ	tetragonal	975 / 1030	300	1.83	1.85	18.5	0.62	0.045	96.2	2.89	[GCTS+07]
Yb:NaYW π	tetragonal	975 / 1030	300	2.55	2.54	13.3	0.61	0.044	98.7	2.05	[GCTS+07]
Vanadates											
Yb:$LuVO_4$ σ	tetragonal	985 / 1040	256	2.08	3.53	14.04	0.285	0.007	255.52	0.97	[LMZ+05]
Yb:$LuVO_4$ π	tetragonal	985 / 1040	256	8.45	11.8	3.89	0.3	0.019	233.89	0.65	[LMZ+05]
Borates											
Yb:LSB	monoclinic	981 / 1042	1000	0.98 (σ)	0.89 (σ)	10.83	0.28 (π)	0.009 (π)	66	0.68	[RJM+05]
Garnets											
Yb:YAG	cubic	942 / 1030	950	0.87	0.11	23.87	1.94	0.14	10.05	1.97	[LCW+91]
Sesquioxides											
Yb:Sc_2O_3	cubic	975 / 1041	800	4.4	4.57	2.85	1.44	0.07	15.80	0.3	[PPG+06]
Yb:Lu_2O_3	cubic	976 / 1032	820	3	2.77	4.3	1.28	0.07	17.39	0.48	[PPG+06]
Apatite											
Yb:SFAP	hexagonal	900 / 1047	1260	9.9	~ 0	2.49	6.0	~ 0	1.99	0.19	[MPS+95]

Table 3.3: Relevant spectroscopic parameters of some important laser crystals. These data are used in figure 3.15 to compare the different hosts.

Thermal conductivity

Beside the spectroscopic properties of the Yb-doped compounds, many other structural, optical and thermal parameters play an important role to define the quality of an active medium for a certain application. For high power laser sources in both the continuous-wave and mode-locked regime, efficient heat removal is essential. Uncontrolled temperature rise of the active media leads to thermal lensing effect that can strongly affect the laser operation and ultimately conduct to the damage of the crystal when the thermal shock resistance is exceeded. In general, a large thermal conductivity value of insulating crystals can be obtained by the combination of (i) a low molar mass, (ii) a high melting-point (high-strength atomic bonds), (iii) a compact crystal structure and (iv) a covalent character of the host [GVV03]. Undoped YAG exhibits favorable properties with a thermal conductivity of 10.7 $Wm^{-1}K^{-1}$. Higher thermal conductivities are reported for example with sesquioxides, which are distinguished by a very high melting point denoting difficult growth processes [1], with values as high as 16.5 and 12.5 $Wm^{-1}K^{-1}$ for the Sc_2O_3 and Lu_2O_3 compounds, respectively [PPG+06]. The undoped monoclinic double tungstates show, on average over the orientation directions, a lower thermal conductivity of 3.06 $Wm^{-1}K^{-1}$, which is still about four times higher than typical phosphate glass [HMGM+98]. Finally, the tetragonal DTs, due to the local disorder, exhibit a significant drop of the thermal conductivity with an average value over the orientation directions of $\sim$ 1.17 $Wm^{-1}K^{-1}$ for NaGdW. This could be a strong limitation for applications that require high output power.

Influence of the ytterbium concentration

Moreover, the variation of thermal conductivity with cationic substitution can be very important. This effect can be attributed to phonon scattering on point defects in the crystalline lattice, where the substitution is taking place. With YAG for example, several independent measurement show a drop of roughly 50% of the thermal conductivity, from 10.7 $Wm^{-1}K^{-1}$ for the undoped YAG to $\sim$ 5.5 $Wm^{-1}K^{-1}$ for 25 to 50 at. % Yb-doping as seen in figure 3.16. Modeling of the effect on the thermal conductivity for different substitution level was compared with Yb.YAG and another garnet, the Yb:$Gd_3Ga_3O_{12}$ (Yb:GGG) [GVV03]. Contrary to the case of YAG, where the Yb^{3+}active ion substitutes a cation; the Y^{3+} ion, with a fairly different atomic weight ($\Delta M/M$=0.48), the Yb^{3+}ion replaces the Gd^{3+} cation that has a much similar atomic weight in the Yb:GGG crystal ($\Delta M/M$=0.09). Due to this comparable atomic weight, the phonon scattering and therefore the drop of the thermal conductivity is much weaker for the Yb:GGG compound (Fig. 3.16).

An even better situation can be expected for the case of Yb:KLuW as the Yb and the Lu ions have nearly similar atomic masses ($\Delta M/M$=0.01) leading to a minimization of the influence of the cationic substitution on the thermal properties. This situation seems to be confirmed in Yb:KLuW crystals by initial measurement with reported values of the thermal conductivity of undoped and 5 at. % Yb-doping of 3.06 and 3.09 $Wm^{-1}K^{-1}$, respectively, indicating no drop of the thermal conductivity.

1. Note that recent progress in the manufacture of polycrystalline media (ceramic), associated with a considerable reduction of the scattering losses, permit to obtain ceramic laser gain media based on crystals with cubic structure with high quality. In this way, the manufacture of ceramic gain media is an attractive alternative for materials that usually require high temperature processing with standard single crystal growth methods like the sesquioxides.

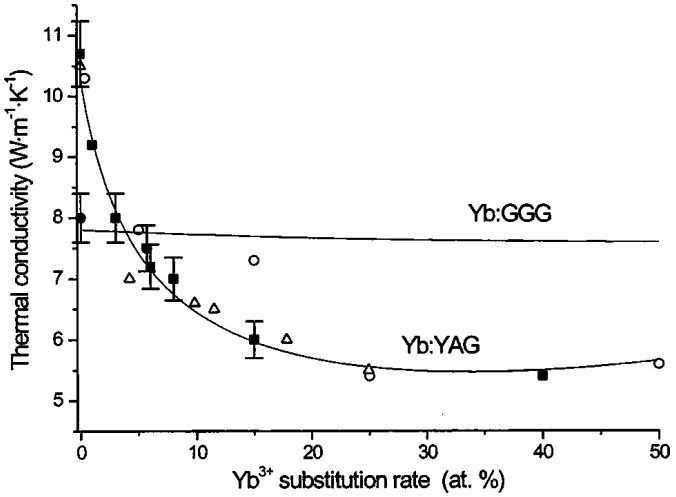

Figure 3.16: Influence of the ytterbium concentration on the thermal conductivity, taken from Gaume [GVV03]

When very high doping concentration is considered, a majority of hosts show strong structural modifications that prevent the growth of crystals with sufficient quality. Moreover, concentration quenching is another detrimental effect that appears at high doping concentration in most gain media. As we already saw in chapter 2, the probability of energy transfer between ions is, in first approximation, determined by the dipole-dipole interaction and becomes important for active ions in proximity to the quenching center with a rate proportional to the inverse sixth power of the distance between ions. Comparatively, the monoclinic double tungstates have here a substantial advantage as they exhibit the largest Yb-Yb ion distance of the established laser gain media [2] (Table 3.4) [PFPJ+05].

In Yb:YAG, the florescence lifetime typically drops quickly for high doping levels [dSMP+03]. Subsequent annealing of this crystal can somehow improve the situation but efficient continuous-wave laser operation of highly doped Yb:YAG, more than 20 at. %, is still not demonstrated. At 100% Yb substitution, corresponding to a stoichiometric material, lasing operation has, as far as I know, been achieved only with YbAG [PHS+01, MIKK07] and KYbW [KPG+03]. In continuous-wave laser operation, the output power was nevertheless very limited for both materials. With YbAG, a maximum output power of 100 mW was achieved while, in spite of the better potential for high doping level, only 20 mW was obtained with KYbW due principally to poor heat management .

2. Actually, the LSB host exhibits an even larger separation between two La sites. Nevertheless, the Yb ion substitutes both the Sc and La sites and the Sc-Sc separation is much reduced in comparison to La. Moreover, at high doping level, Yb:LSB is known to change to the tetragonal huntite structure.

Host	Yb-Yb [Å]	Relative energy transfer probability (R^{-6}) [%]	$\sigma_{em,P}$ [10^{-20}cm^2]	τ_f [μs]	ref.
Yb:Lu_2O_3	3.43	153	1.28	820	[PFPJ+05]
Yb:YAG	3.68	100	1.94	950	[PFPJ+05]
Yb:KLuW	4.05	56	14.7	320	[PPM+07]

Table 3.4: Energy migration in different hosts

Double tungstates doped with other rare-earth ions

It is worth mentioning that the attractive features of the double tungstates when doped with the Yb ion are also obtained with other rare-earth ions. In particular, thulium-doped double tungstates exhibit favorable characteristics with absorption bands that well overlap with AlGaAs diode lasers and high and broad emission cross sections in the 2 μm spectral range. Such lasers have been already extensively studied at the Max-Born-Insitute by some collaborators and myself with both the monoclinic and tetragonal double tungstates [PPM+07, RMP+07, CTHGC+08]. The full description of these results will, however, not be treated in this thesis.

3.3.2 Ultrashort pulse generation

Continuous-wave mode-locking is currently the straightforward method to generate femtosecond pulses. Whereas a laser often oscillates in only one axial mode, in a mode locked laser, additional energy is transferred to adjacent modes with the correct phase. In the time domain, these axial modes that are locked in phase form a short pulse of duration inversely proportional to the width of the emission spectrum. Beside all the criteria that are necessary for efficient continuous-wave operation that have been just discussed in the last section, gain media for mode-locked operation should hence additionally offer a broad emission bandwidth. More precisely, a large range of wavelengths in which a smooth gain spectrum is obtained for a fixed inversion level is desired [PK03]. A simple but approximate evaluation for ytterbium-doped gain media in the mode-locked regime consists in the evaluation of the full width at half maximum FWHM of the gain spectrum for a maximum inversion β of 0.5. The gain cross section with different values of the inversion is shown for both the monoclinic Yb:KLuW and tetragonal Yb:NaYW double tungstates in figure 3.17.

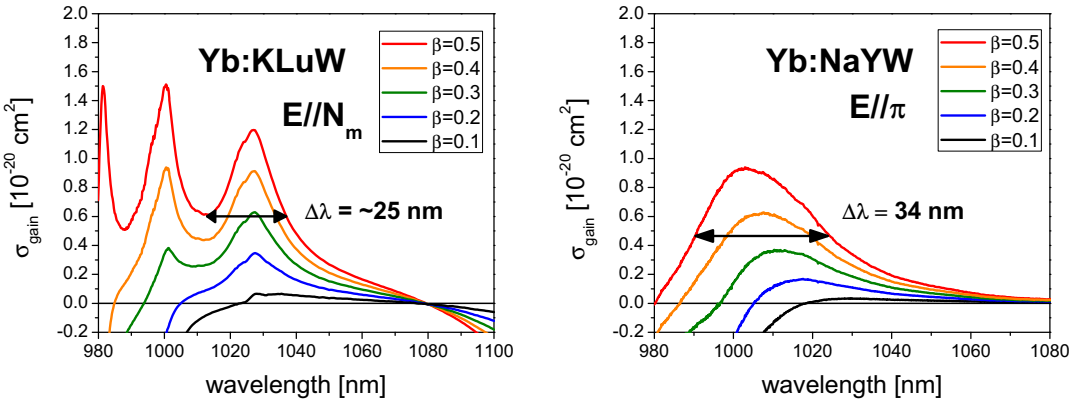

(a) (b)

Figure 3.17: Calculated gain cross section σ_{gain} (equation 2.8) with different values of the inversion β for (a) the monoclinic Yb:KLuW and, (b) the tetragonal Yb:NaYW double tungstates. The FWHM of the gain is indicated for an inversion of 0.5. These two curves are obtained from the measured transitions cross sections presented in figures 3.8 and 3.14 for the monoclinic and tetragonal double tungstates, respectively.

In this figure, the difference between the monoclinic and tetragonal compounds is clear to be seen. While the monoclinic compound exhibits a much higher gain with some strong modulation, the tetragonal compound shows a lower but very broad and smooth gain. The modulation seen for Yb:KLuW arises form the different transitions between the energy levels of the two manifolds. The strong peak around 980 nm corresponds to the zero line; the (0')-(0) transition, while the peak around 1000 nm coincides with the (0')-(1) transition. Finally the rather broad peak at 1030 nm can be associated with the overlap of the (0')-(2) and (0')-(3) transitions that are habitually involved in the laser operation. This apparent modulation of the gain for high inversion in Yb.KLuW is typical of compounds exhibiting high emission cross sections and is also particularly present in sesquioxides crystals for example. This modulation also explains that the achievable mode-locked bandwidth can be considerably smaller than the tuning range achieved in CW lasers. Moreover, the actual inversion that is obtained in Yb-lasers is generally much lower than the maximum theoretical inversion of 0.5 in a three-level laser. This further reflects the limitation of this evaluation and the difficulty to predict the mode-locked spectral width and therefore the pulse duration that can be achieved with a specific Yb-doped gain medium.

Q-switching instabilities

As we will see later in section 6.5, the rise of Q-switching instabilities can be an important limiting factor. In particular, at high output power and repetition rate, this effect becomes significant and typically prevents stable mode-locked operation.

Under certain approximations, a criterion for stable passive mode-locking can be derived and the threshold for Q-switching instabilities is found to depend on the spectroscopic proper-

ties of the gain medium through the term $E_{sat,g}$ as

$$E_{sat,g} = \frac{Ah\nu_L}{\sigma_{em,L} + \sigma_{abs,L}} \tag{3.1}$$

with A the mode area inside the gain medium. In order to supress the tendencies for Q-switching in mode-locking, it is then desirable to use gain medium with a large emission cross section. Unfortunately, as we saw in chapter 2, a large emission cross section is usually connected to a narrow emission bandwidth that does not allow the generation of ultrashort pulses. Thus, we are confronted to a balance between extremely broadband emission cross sections and a high Q-switching instabilities threshold.

Having explained the specific parameters that allow short, stable and efficient pulse generation, it is now interesting to compare a few Yb-doped gain media that are interesting for the mode-locked regime. In table 3.5, some selected spectroscopic parameters are shown for several hosts. The maximum bandwidth corresponds to the full width at half maximum of the gain for an inversion of 0.5 and the minimum duration is the related pulse duration assuming a time-bandwidth limited secant hyperbolic pulse shape (see chapter 6 for more details).

Yb-doped gain media	λ_P / λ_L [nm]	$\sigma_{em,L}$ [10^{-20} cm^2]	Maximum theoretical bandwidth [nm]	Minimum theoretical duration [fs]	Fluorescence lifetime [μs]	Thermal conductivity [Wm^{-1}K^{-1}]
Yb:YAG	942 / 1030	1.94	9	124	950	10.7 - 5.5
Yb:Sc_2O_3	975 / 1040	1.44	11.4	100	800	16.5 - 6.5
Yb:Lu_2O_3	976 / 1032	1.28	12.9	86	820	12.5 - 11
Yb:KLuW N_m	981 / 1030	2.6	25	45	320	∼3.3†
Yb:KLuW N_p	981 / 1045	1.4	26	44	320	∼3.3†
Yb:NaYW σ	975 / 1030	0.62	41	27	300	‡
Yb:NaYW π	975 / 1030	0.61	34	33	300	‡
Yb:$LuVO_4$	985 / 1040	0.3	36	31	256	∼5.5†
Yb:glass	975 / 1020	0.05	35	31	1300	0.8
Yb:$CaGdAlO_4$	980 / 1050	0.8	80	14	420	6.5

†averaged over the orientation directions ‡∼ 1.17 Wm^{-1}K^{-1} for NaGdW

Table 3.5: Comparison of Yb-doped gain media for mode-locked lasers

The broadening of the emission spectra is directly related to a drop of the emission cross section as well as the thermal conductivity. Three distinct classes of gain media can be sorted out. The laser media that exhibit a high thermal conductivity but show rather limited possibilities for the generation of ultrashort pulses like the Yb:YAG and sesquioxide crystals. On the opposite, there are some crystals that present extremely broad and smooth emission spectra with low cross section like the tetragonal double tungstate, the diverse glass compounds as well as the Yb:$CaGdAlO_4$ (Yb:CALGO). In general, such gain media are inevitably related to a low thermal conductivity, at the notable exception of the recently introduced Yb:CALGO. Such type of crystals offer a high potential for extremely short pulse generation but may reveal difficulties in suppressing Q-switching instabilities especially at high output power levels due to their low emission cross section. Finally, Yb-doped monoclinic double tungstates, here represented by

the Yb:KLuW compound, correspond to an intermediate case, where both a large and broad emission cross section is possible thanks to their strong anisotropy. As one can see, the thermal conductivity of these crystals also corresponds to an intermediate situation.

Chapter 4

Tungstate lasers with composite structures

While the focus of last chapter laid on the investigation of laser gain media, this chapter considers the influence of geometrical factors. Here, one has to take into consideration the different possible shapes and structures of the gain media as well as the different pump geometries. As we will see, at these different stages, proper choices can substantially improve the final laser performance.

In general, the thermal management of a laser can be considerably improved by the implementation of composite structures, i.e. crystals composed of several segments of dissimilar materials or different dopant concentration of the same material. Improvements as such will be discussed in section 4.1. In addition, the shape and dimension of a laser gain medium is also known to play an important role. Basically, in the case of a crystalline gain medium, three different categories can be isolated: the rod laser, the slab laser and the thin disk laser geometry [1], Fig 4.1.

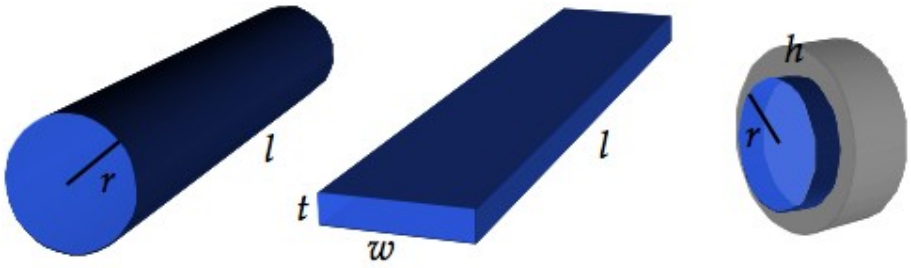

Figure 4.1: The rod, slab and thin disk geometries. The lenght l of the rods and slabs are typically a few mm to cm long while the height h of the thin disk does not exceed 400 μm.

1. In the case of amorphous gain media, the fiber geometry has also to be considered. The strong interest in fiber lasers comes from the guiding effect and the high surface-to-volume ratio that prevent strong thermal problems. Hence, recently developed fiber lasers can typically deliver output powers of several hundred of watts or even kilowatts.

An essential property of rod lasers is that the dissipated heat is dominantly extracted in directions perpendicular to the beam axis. As a consequence the thermal lensing effects inevitably become strong for high output power so that scaling to high output power levels is rather restricted.

A laser slab is thin in one dimension in comparison to the other two directions. The heat management is then superior compared to the rod laser with a temperature gradient that is limited in the two long dimensions. However, as the heat is extracted from the top and bottom faces, a strong temperature gradient still exists in the vertical direction.

Lastly, the concept of the thin disk laser consists in reducing the thickness of the active layer so that it becomes considerably smaller than the laser beam diameter. After proper optical coating, the active element is mounted on a heat sink. In this way, the heat generated is extracted dominantly through one end face, i.e. in the longitudinal rather than in the transverse direction [GHV+94]. The temperature gradients are therefore principally in a direction perpendicular to the disk surface and thus cause only weak thermal lensing. Such thin disk geometry will be studied in detail in section 4.2.

As we will see in the following section, the planar waveguide can be assimilated, due to its similar shape, to a modified slab geometry when thermal effects have to be considered. A guiding geometry offers moreover the substantial advantage that high overlap between the pump and laser modes can be maintained over the whole length of the crystal. As we will see in section 4.3, this is essential in order to keep a high efficiency with a low threshold in a quasi-three level laser. The last section of this chapter 4.4 will shortly review the different methods that successfully engineered composite structures with the highly anisotropic double tungstates.

4.1 Composite crystals

In addition to the advantages that are provided by these different crystal shapes, it is well known that composite materials can significantly improve the laser performance at high power levels [TTKI97]. This is in particular true for Yb-doped laser media whose behavior is temperature dependent due to their quasi-three-level laser character. The addition of an undoped layer to the active crystal is used mainly for managing the thermal effects. This undoped cap acts as a heat sink for the active crystal, reducing the peak temperature at the input face (with respect to the pump beam) and thus the thermal lensing effect.

In figure 4.2, a simulation displaying the temperature profile in (a) - (b) composite crystals and (c) - (d) single bulk crystals is shown [DCB+05]. It can be seen that the peak temperature at the input face is strongly reduced in the case of composite structures (a) and (b). It should be pointed out that the implementation of heterocomposite structures as shown in (a) is restricted with the monoclinic double tungstates due to their large thermo-mechanical anisotropy. Besides, the use of such structures is not always favorable as the high refractive index difference between the two dissimilar materials can generate parasitic reflections or birefringence effects that could strongly affect the femtosecond regime [KFB+92].

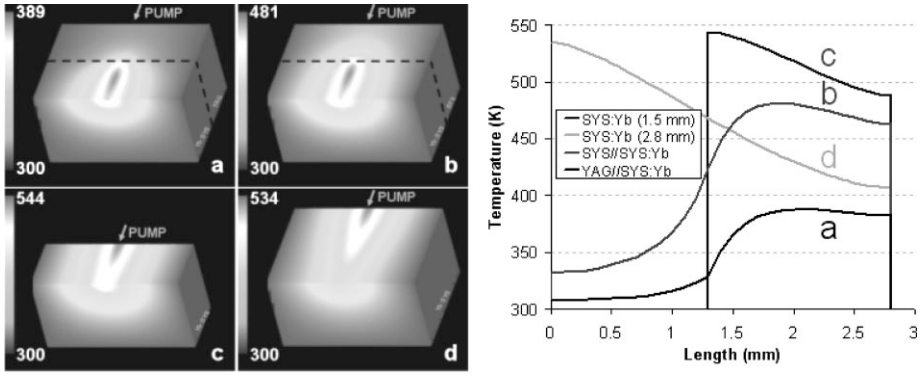

Figure 4.2: Simulation revealing the temperature profiles (obtained with LASCAD software) under 13.2 W of incident pump power in (a) a heterocomposite (Yb:SYS/YAG) crystal, (b) a homocomposite (Yb:SYS/SYS) crystal, and (c), (d) in a single Yb:SYS crystal of 1.5 mm and 2.8 mm thickness, respectively. Saturation of the absorption is not considered. Taken from [DCB+05].

Composite structures also help to reduce the bulging of the surface of the thermally loaded layer; a compressive strain is maintained on the heated surface reducing the risk of fracture. An additional advantage of an undoped cap is the isolation of any optical coating from the doped part of the crystal which is particularly relevant to dichroic coatings that often exhibit temperature sensitivity degrading their performance. Due to the refractive index change between the doped and the undoped part, waveguide structures can be designed. They can serve as guide for the pump light [GGS+00] or as true waveguide lasers [BBST00].

Undoped layers can also act as guides for the pump light resulting in efficient and uniform absorption into the gain medium. Finally, when the fabrication of extremely thin active layers (sub 100 μm) is considered such as in the thin disk geometry, it is of high interest to implement an undoped cap for thermo-mechanical stability.

4.2 The thin disk laser concept

The thin disk laser concept is based on a geometry that enables a very efficient heat extraction from the active element. Thus, thermal problems are kept at a minimum and power scaling to very high output power level is feasible. Moreover, this geometry has the advantage that the use of highly-divergent high-power laser as pump source is possible due to the reduced transversal dimension of the active layer.

Scaling laws

Let us consider a thin disk with an active layer thickness h and a pump mode area A. If one assumes an almost one dimensional heat flow in an isotropic medium, the maximal pump

power that can be delivered to the laser medium can be approximated by

$$P_{max} = \frac{2\kappa \Delta T_{max} A}{qh} \tag{4.1}$$

with ΔT_{max} the maximal increase of the temperature of the medium that is tolerable before deterioration of the performance, κ the thermal conductivity and q the quantum defect as defined earlier in chapter 2. The other limit concerning the maximal pump power is set by the maximum stress that is tolerated by a material. This limit can be expressed in terms of the steady state resistance parameter that depends only on the material parameters [EKK+84] and is given by

$$R_s = \frac{k\sigma_T(1-\nu_{Poi})}{\alpha E_Y} \tag{4.2}$$

where σ_T is the maximal surface stress at which the fracture occurs, ν_{Poi} is the Poisson ratio, α is the expansion coefficient and E_Y is the Young modulus. The maximum pump power can be then expressed as [KBDU06]

$$P_{max} = \frac{3R_s A}{qh}. \tag{4.3}$$

As one can see, the two expressions giving the maximum pump power before deterioration of the laser performance or damage are directly proportional to the aspect ratio A/h of the thin disk. Thus, the thickness of the active layer has to be kept thin enough to allow efficient heat removal and keep a one-dimensional heat flow. The power scalability of the thin disk laser can then be fully exploited by increasing the pump and resonator mode area. In this way, the output power can be doubled by doubling the pump power and the mode area on the disk while keeping the thickness and the output coupler transmission constant. With the well known Yb:YAG gain medium, such scaling procedure allows for output powers of more than 8 kW with a beam quality M^2 of about 24 or more than 225 W with an M^2 better than 1.2 [GS07]. Nevertheless, the principal drawback of Yb:YAG is its very small absorption cross section in combination with difficulties to achieve efficient laser operation at high doping levels. This indicates that efficient absorption of the incident pump beam is not feasible for sufficiently thin active layer and that complex pump designs with parabolic mirrors and up to 16 double passes have to be developed (Fig, 4.3).

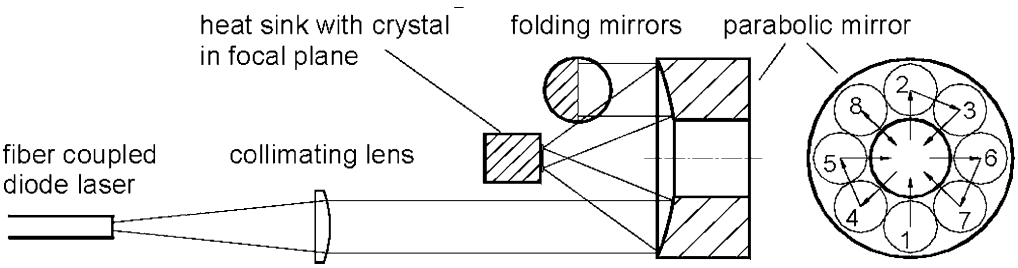

Figure 4.3: Pump design of the thin disk laser with 8 double passes [GS07].

In contrast, Yb:KLuW is ideally suited for efficient absorption of the incident pump beam as it exhibits the highest absorption cross section among the Yb-doped media and allows the development of highly doped active layers with minimum concentration quenching. Ultimately, the absorption length can be extremely short, e.g. 13.3 μm at 981 nm for 100%-doping and polarization parallel to the N_m-optical axis. Unfortunately, moving to the sub-100 μm thickness range, a mechanical challenge for any crystalline material, is even more demanding for the monoclinic double tungstates which exhibit thermo-mechanical anisotropy and thermal conductivity roughly two times lower than Yb:YAG. The implementation of an undoped cap on the top of the active layer can, however, provide substantial improvement of the thermo-mechanical stability of such a thin element. Moreover, an undoped cap has the additional advantage to permit the amplified spontaneous emission (ASE) to effectively leave the active medium. The ASE is one limiting factor of the thin disk laser concept at very high output power levels.

The anti-ASE cap

The amplified spontaneous emission (ASE) can be a crucial limiting factor for the power scaling of thin disks lasers. The introduction of an undoped cap, allowing the ASE to leave from the active medium, was suggested. Very recently, the influence of this undoped cap on the maximum output power in the thin disk geometry was investigated [KBss]. The improvement of performance of an optimized thin disk laser due to such anti-ASE cap can be characterized by the increase of maximum output power achievable at a given round-trip loss α. The ratio of the maximum power that can be obtained with and without anti-ASE cap, $P_{out,cap}$ and P_{out}, respectively, can be expressed as

$$\frac{P_{out,cap}}{P_{out}} \approx 0.2 \left(ln \frac{3}{\alpha} \right)^2 . \tag{4.4}$$

From this equation, it can be seen that for comparable round-trip losses α, the anti-ASE cap should provide some noticeable advantage. On the other hand, it is evident that an imperfect interface between the active part and the undoped cap would affect the round-trip loss. The above analytical model shows in particular that an increase of loss by a factor of the order of four may overrule the advantage of the undoped cap. Special attention has to be paid to keep a very high quality of the interface. It becomes particularly important to minimize the lattice mismatch when the doping concentration is very high. Composite structures based on Yb:KLuW/KLuW are then ideally suited for highly doped composite structures as the lattice mismatch is minimized as a result of the close ionic radii of Yb and Lu ions, see table 4.1

Cell parameters	a [Å]	b [Å]	c [Å]	$< \Delta g >$
KLuW	10.576	10.214	7.487	
KYbW	10.590	10.290	7.478	
difference Δg	0.13%	0.74%	0.12%	**0.33%**
YAG	12.0116			
YbAG	11.9380			
difference Δg	0.61%			**0.61%**
KYW	10.6313	10.3452	7.5547	
KYbW	10.590	10.290	7.478	
difference Δg	0.38%	0.53%	1.01%	**0.64%**

Table 4.1: Minimum lattice mismatch for Yb:KLuW composite structures

4.3 The waveguide geometry

Besides their high potential as bulk and thin disk lasers, rare-earth-ion-doped monoclinic double tungstates also show important prospects for integrated structures. Their high refractive indices make these materials suitable for applications that require optical gain and high power as well as a rather high integration density. Electromagnetic radiation at optical wavelength can be confined by means of total internal reflection at a boundary. Such optical confinement is obtained if the refractive index of the core region is higher than that of the surrounding region.

Reduced threshold

The waveguide geometry is very important for quasi-three level laser as it allows to achieve enhanced confinement and hence improved overlap of the pump and laser modes. It consequently reduces the intrinsic reabsorption losses of such lasers and lowers the threshold. The general drawback of such geometries is that waveguides usually have higher propagation losses than bulk material. This is typically due to the fabrication processes, which lead to spare roughness and scattering losses at the imperfect interfaces. The choice of a suitable method and its optimization is therefore critical for successful manufacturing of active devices where the reduction of the reabsorption losses prevails over the increased scattering losses. It should also be noted that the scattering losses at the optical interfaces usually increase with increasing refractive-index step. It is therefore interesting to develop buried waveguides, where the active layer is surrounded by material of lower refractive index, instead of surface waveguide, where the upper interface presents a big refractive index step between the waveguide material and air, fig 4.4.

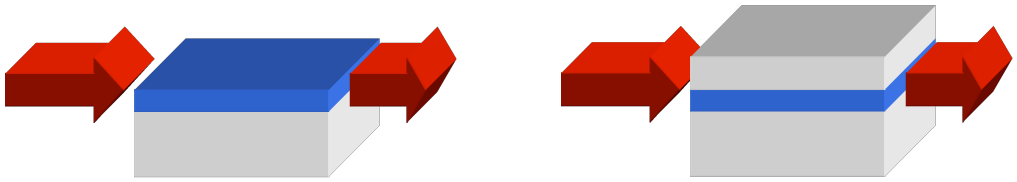

(a) (b)

Figure 4.4: (a) Surface and, (b) buried planar waveguide structures.

In order to express the advantages that such longitudinally pumped planar waveguides lasers have against their bulk counterparts, it is interesting to present an analogous analysis to that of Mackenzie [Mac07] and adapt it here to double tungstate waveguides. An expression for the threshold can be calculated as shown in section 2.4, equation 2.19

$$P_{th} = \frac{h\nu_p(V_{eff}/l_c)}{2\tau_f(\sigma_{abs,L}+\sigma_{em,L})}(L_i + T_{OC} + 2Nl_c\sigma_{abs,L}) \tag{4.5}$$

where the quantity V_{eff} is the effective mode volume defined as in equation 2.20

$$V_{eff} = 1/\iiint_{crystal} r_p(x,y,z)\phi_0(x,y,z)\,dV \tag{4.6}$$

with $r_p(x,y,z)$, the spatial distribution of the pump and $\phi_0(x,y,z)$, the spatial distribution of the laser photons. By adding a term for the losses specific to the waveguide structure (α_p is the exponential propagation loss coefficient for the waveguide) and by introducing a term κ as the ratio of the output coupling to the round trip losses for each laser architecture [Mac07], it is then possible to find an expression for the bulk to waveguide threshold ratio

$$\frac{P_{th-bulk}}{P_{th-wg}} = \frac{V_{eff-bulk}}{V_{eff-wg}}\left(1 - \frac{2\alpha_p l_c(\kappa+1)}{(\kappa+1)L_i + 2Nl_c\sigma_{abs,L}}\right). \tag{4.7}$$

Assuming a Gaussian beam focused at the center of the crystal as in [DG85] , for a given laser medium length, refractive index and pump wavelength, the pump waist w_0 that minimized the average pump beam area inside the active medium is then given by

$$w_0 = \sqrt{\frac{\lambda_P l_c}{\sqrt{3}\pi n_P}} \tag{4.8}$$

for which we obtain an average pump beam area $w_{avg} = \sqrt{2}w_0$. If one assumes that the waveguide with a core of full width d is single mode, the ratio of the effective mode volume can be then calculated for a planar waveguide geometry.

$$\text{planar waveguide: } \frac{V_{eff-bulk}}{V_{eff-wg}} \approx \frac{2w_{avg}}{d} \tag{4.9}$$

If this ratio is introduced in the expression 4.7 for the threshold one obtains a general expression comparing the ratio of the thresholds for a bulk and planar waveguide laser [2].

By relating this general expression to an ideal 4 level laser and a real Yb:KYW laser exhibiting reabsorption losses it is possible to compare the advantage of the waveguiding structure for both laser systems. In figure 4.5, these both operating schemes are compared for different propagating loss coefficients. For this evaluation, the spectroscopic properties of Yb:KYW at 1030 nm were considered, the intrinsic loss parameter L_i was set to be equal to 0.01 and a waveguide structure with a core width d of 10 μm was assumed. Finally, the two loss propagation coefficients were set to 0.05 dB/cm and 0.5 dB/cm as suggested in [Mac07].

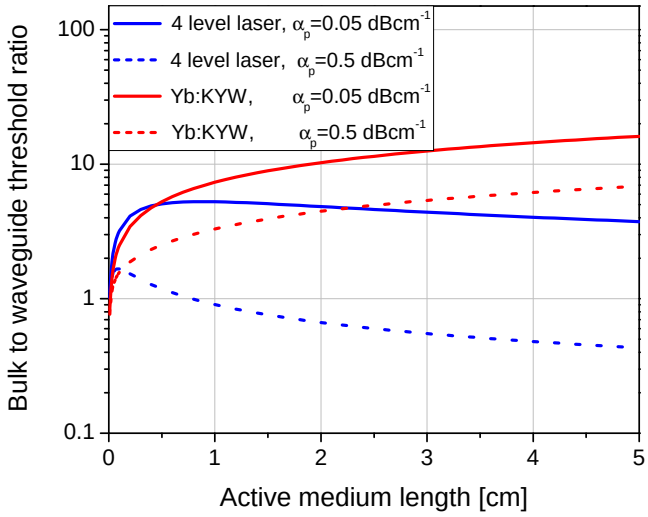

Figure 4.5: Comparison of the laser threshold for a bulk active medium and the same material with planar waveguide configurations. The bulk to waveguide ratio $\frac{P_{th-bulk}}{P_{th-wg}}$ as defined in equation 4.7 is plotted versus the active medium length for different propagation losses α_p. The blue curves correspond to a perfect 4-level laser and the red curves corresponds to the Yb:KYW laser.

As one can see here, the waveguide geometry in a four level laser (blue curves) can bring some advantages in terms of threshold for low propagation losses but as soon as these losses become significant the advantages disappear. On the contrary, with quasi-three level lasers such as Yb:KYW, the benefit of using a guiding geometry can be very important for both propagation losses and particularly for propagation losses inherent to the waveguide that are kept small in comparison to the reabsorption losses. From equation 4.9, one also can conclude that the bulk to waveguide threshold ratio is inversely proportional to the core width d. Thus, a waveguide geometry with very small core width will further favor low laser threshold. The drawback of such thin structures is obviously the critical coupling efficiency of the pump beam

2. Similar analysis can be done when confinement in two directions is obtained, i.e. in linear or channel waveguides. In this case, the guiding effect in two directions corresponds to an even further advantage in terms of threshold.

into thin active layers. An elegant way to bypass this problem is to use the so called double-clad planar waveguide [BBST00] where the thin single mode active layer is surrounded by a large multimode guiding layer where the pump can easily be coupled in.

Thermal management

The waveguide geometry can be associated with a modified slab geometry. It is known that such structures have some significant advantages in terms of thermal management. The theory necessary to analyze thermal stress in a rod or a slab geometry has been developed by Eggleston et al [EKK+84]. Following this formalism, it can be shown that for a rod geometry of isotropic material with radius r, the maximum power per unit length at the stress fracture is

$$\left(\frac{P_{max}}{l}\right)_{rod} = 8\pi R_s \tag{4.10}$$

with R_s the steady state thermal stress resistance parameter depending on material properties as in equation 4.2. As we can see, the maximum thermal loading in this configuration is independent of the rod diameter. For a slab consisting of a rectangular geometry with thickness t, width w and length l, fig. 4.1, the maximum power per unit length at the stress fracture is shown to be

$$\left(\frac{P_{max}}{l}\right)_{slab} = 12R_s\frac{w}{t} \tag{4.11}$$

where we see this time that the maximum thermal loading is inversely proportional to the thickness t.

Since the planar waveguide structures are very close to a slab geometry, the analysis given above has to be slightly modified and then can be extended to such structures [SHL+01] if one assumes that the heat input is only within the core. The final maximum power per unit length at the stress fracture for a planar waveguide of width w, core thickness d and total thickness t changes into

$$\left(\frac{P_{max}}{l}\right)_{wg} = 8R_s\frac{w}{t-(d^2/3t)}. \tag{4.12}$$

For a total thickness much larger than the core ($t \gg d$), one obtains

$$\left(\frac{P_{max}}{l}\right)_{wg} \approx 8R_s\frac{w}{t}. \tag{4.13}$$

We see here that the power per unit length is reduced by a factor of $2/3$ in comparison to the slab (eq. 4.11) but, more important, $\frac{P_{max}}{l}$ remains inversely proportional to the total thickness t of the structure. The ratio of thermal power absorbed per unit length at the stress fracture limit is finally given by

$$\frac{(P_{max}/l)_{wg}}{(P_{max}/l)_{rod}} \approx \frac{1}{\pi}\frac{w}{t}. \tag{4.14}$$

As a consequence, due to the large surface-to-volume ratio of the waveguide geometry, the heat dissipation becomes efficient. The ratio w/t must be greater than three to have superior thermal

handling capability than for the rod geometry. In most practical applications, this condition can be easily fulfilled as the total thickness t can be chosen to be only slightly larger than the core of the waveguide and no direct restriction is set on the width w.

4.4 Manufacture of composite structures based on double tungstates

The advantageous structures detailed in the previous section are based on crystals with multiple segments of different doping concentrations. The introduction of such structures with the strongly anisotropic double tungstates is currently a challenge and, up to now, only three methods have led to successful laser operation. These three methods are shortly discussed in the following sections.

4.4.1 Liquid phase epitaxy

Liquid phase epitaxy (LPE) is a well-known technique for producing oxide films for laser applications, in which a crystalline layer can be grown from a molten solution onto an oriented single-crystal substrate [FCC99]. The major advantage of LPE compared to epitaxial techniques from the vapor phase is that LPE is a near-thermodynamic equilibrium process, and therefore, high-quality single-crystalline layers are feasible [PR07].

LPE was first adapted to the monoclinic double tungstates at the Univesitat Rovira I Virgili (URV), Spain where epitaxial layers for longitudinal pump geometry were produced. In a second time, this method was adjusted for the manufacture of waveguide structures at the Ecole Polytechnique Fédérale de Lausanne, Switzerland. Their work is succinctly summarized here.

Liquid-phase epitaxy (LPE) with vertical substrate dipping has been developed to produce Yb:KLuW and Yb:KYW thin planar layers. The LPE set-up is based on a non-vacuum resistance-heated furnace with vertical loading. Inside the furnace, there is a crucible filled with a molten solution of KLuW or KYW in an appropriate solvent. The tungstate solvent $K_2W_2O_7$ used can offer a large thickness and good layer quality. The $K_2W_2O_7$ solvent offers the additional advantage that it contains no impurity ions and ensures a high solubility for double tungstates [SNR+96].

When cooling the liquid solution down, at a certain temperature it becomes supersaturated. The substrate is immersed partially and rotated in the supersaturated solution, and the KYW layer can be grown. Thus, planar layers with thickness d = 5 to 100 μm and a surface area of $\sim$0.5 cm^2 can be grown at an average growth rate of 18 $\mu m/h$. After the growth, the substrate with layer is withdrawn from the liquid and the whole system is cooled down to room temperature. X-ray diffraction (XRD), optical microscopy, and interferometry confirmed that the layers are single-crystalline and strictly oriented in the [010] crystallographic direction, whereas X-ray fluorescence spectroscopy (XRF) and energy-dispersive X-ray analysis (EDAX) showed that the layer composition corresponds to that of stoichiometric KYW.

When adding a small amount of RE_2O_3 powder to the initial solution, RE^{3+}-doped monoclinic double tungstates layers can be grown, where the RE^{3+} ion substitutes for the Lu^{3+} or Y^{3+}. For the Yb^{3+} ion whose ionic radius has a considerable misfit with that of Y^{3+}, there is a certain maximum concentration above which the grown Yb:KYW layers are cracked because of the accumulated lattice strain. The maximum concentration of Yb^{3+} in crack-free Yb:KYW

layers is about 15 at.% with respect to Y^{3+} [ASA+04]. In the case of KLuW, higher doping concentration can be achieved due to smaller lattice mismatch and high quality Yb:KLuW layers with up to 50 at.% could be successfully produced [PRG+06]. KLuW is thus the ideal compound to manufacture highly doped composite structure for longitudinal pumping in a thin disk geometry 5.3.4. On the other hand, KYW appears to be the most popular tungstate crystal with more mature technology for which raw materials can be obtained with highest purity and at lower price. The KYW compound is then ideally suited for structures requiring relatively low dopant concentration such as planar waveguides.

LPE for waveguide geometry

Since KYW is isostructural to KYbW (100% substitution of Y^{3+} by Yb^{3+}) [KK69, PSM+02] and KYbW presents a higher refractive index for all principal optical axes (fig 4.6), one can assume that the refractive indices of Yb:KYW layers increase linearly with increasing ytterbium concentration. In this way, optical confinement is achieved directly within the doped layer.

Typical dopant concentrations used in the present studies were well below the critical ones and varied from 1.2 to 2.4 at.% for Yb^{3+}. The refractive-index change of a 1.8 at.% Yb^{3+}-doped layer with respect to the undoped substrate is expected to be 6×10^{-4}, which was confirmed experimentally by dark m-line spectroscopy. If higher optical confinement is necessary, significantly larger refractive index change can be obtained in Lu and Gd co-doped Yb:KYW layers, where high concentrations of optically inert Lu^{3+} and Gd^{3+} dopants are incorporated to increase the refractive index change up to 7.5x10^{-3} [GRB+07].

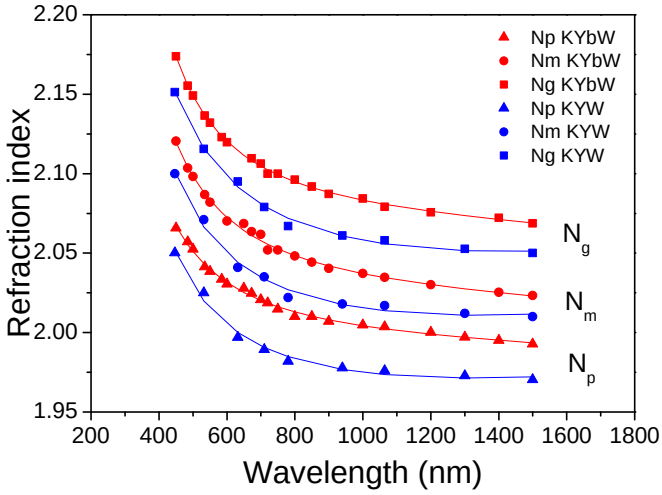

Figure 4.6: Difference of refractive index for the KYW and KYbW crystals. Measurement done at the URV, Tarragona, Spain.

In order to prepare optical waveguides, the surface and both endfaces of the grown Yb:KYW layers have to be accurately polished to remove flux residuals and growth steps. As mentioned above, the substrate is only partially immersed in the solution, and its upper part is not covered with the layer. This uncovered part was employed as a reference plane, which allowed to

precisely polish the layer surface parallel to the interface. Polishing with alumina suspensions resulted in a root-mean-square (rms) value of the surface roughness of 2.3 nm. Both endfaces of the waveguides were also polished to laser-grade quality taking precautions to avoid chamfering the layer edge. Figure 4.7(a) shows the optical image of the polished endface for a Yb:KYW surface layer. The interface is sharp and straight without any detectable defects.

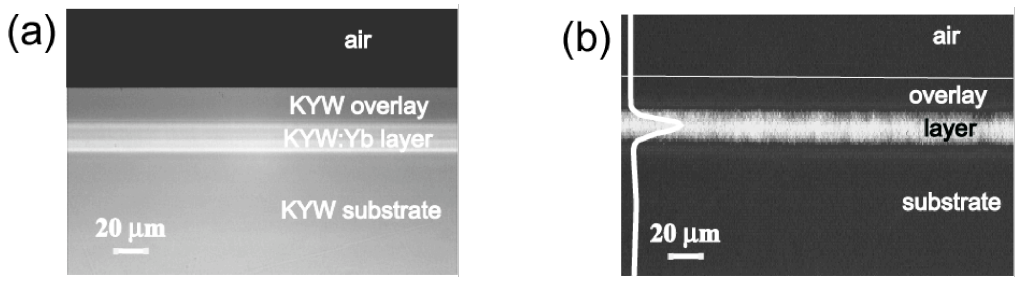

Figure 4.7: (a) Optical photograph of the endface of a 1.2at.% Yb^{3+}-doped KYW surface layer; (b) near-field image of the guided pump light and Yb^{3+} fluorescence outcoupled from the waveguide. Obtained from the EPFL, Lausanne, Switzerland [PRG+07].

The layers were tested as active and passive planar waveguides under laser excitation at 981 nm (InGaAs diode laser), 632.8 nm (He-Ne laser), or 488 nm (Ar-ion laser). The pump light was coupled into the active layer along the crystallographic c-direction by focusing with a microscope objective. The propagated light was imaged onto the sensor of a CCD camera with another microscope objective. For the 11-μm-thick waveguide shown in Fig. 4.7(b), the emitted Yb^{3+} fluorescence was guided together with the 981-nm pump light in the surface Yb^{3+}:KYW layer. The vertical intensity profile of the outcoupled light is close to a Gaussian distribution, since only one TE mode at λ = 980 nm can be supported by the 11-μm-thick planar waveguide in vertical direction.

Propagation losses of the optical waveguides were evaluated by observing the decay of the Yb^{3+}-fluorescence intensity emitted perpendicular to the waveguide plane as well as by evaluating the laser performance and were found to be only 0.1-0.2 dB/cm at 981 nm. This confirms the high structural quality of the LPE-grown Yb:KYW planar layers, which can be used as the starting point for the fabrication of complex buried or channel-waveguide structures.

4.4.2 Segmented growth

Segmented crystal growth is an alternative method developed at FEE GmbH to obtain composite single crystals [Ack02] in which two or more segments of bulk single crystalline material are grown on top of each other. In the simplest case of two segments, the resulting crystal can be used for the fabrication of composite optical elements with two parts of different concentration of dopants if these elements are core drilled across the interface between the segments.

Segmented growth of Yb:KYW on undoped KYW was performed in a standard top-seeded solution growth setup. The first-grown segment could be either doped or undoped. The seed orientation was along the monoclinic b-axis, thus yielding a flat growth interface. This fact is important for the growth of the second segment which had to start on this interface. The two segments were grown from solutions with different Yb concentration (in this case 0 and 13 at.

%). The 13 at. % Yb concentration in the solution (with respect to the total Y+Yb amount), should amount to 10 at. % Yb in the crystal, if one takes into account an empirically determined segregation coefficient of 0.8 for Yb in KYW. The starting materials used for the crystals grown at FEE for the present study were all of purity grades equal to or better than 99.99%. The pulling rates were between 0.05 and 0.1 mm/h. The resulting crystals had typical lengths of 3 to 6 mm for the undoped and 5 to 10 mm for the doped parts, Fig. 4.8. Crack-free boules with 10×10 mm^2 cross-sections were obtained. At present, the interface still shows some inclusions, the bulk material is of comparable quality to standard top-seeded grown samples. The observed densities of inclusions are in the range 500-1000 cm^{-2}, a value much higher than in comparable bonded parts made of more conventional (and isotropic) materials such as YAG. Their origin in KYW is at present still unknown. Segmented growth is thus capable to provide composites with segment length of several millimeters.

Figure 4.8: Segmented grown Yb:KYW/KYW crystal. The top, undoped KYW segment is grown first. The second KYW segment is 13 at. % Yb-doped. Scale grid: 10 mm. Obtained from FEE GmbH, Germany.

4.4.3 Diffusion bonding

Diffusion bonding is a direct-bonding method which permits the production of multi-layer crystal composites with bulk optical properties [BBW+97]. Diffusion bonding also allows to combine rather dissimilar materials. Crystal composites have already been manufactured with various laser hosts, such as YAG, GGG, YVO_4 or SYS including crystal/glass combinations [LBER91, DCB+05]. The strong anisotropy of the monoclinic double tungstates, however, prevented so far the successful manufacture of such diffusion-bonded crystals.

The diffusion bonding of 5% Yb-doped KYW on undoped KYW was performed at FEE GmbH on crystals grown and processed in-house. The diffusion bonding technique involves the assembly by optical contacting of precision finished crystal components and heat treating the composite component to increase bonding strength. In the present case, bonding was performed in air at 650°C. Since no bonding agents are required, residual reflection at the interface is mainly due to differences in refractive indices between the undoped and doped parts.

Chapter 5

Continuous wave double tungstate lasers

This chapter is dedicated to the continuous-wave laser experiments with the double tungstate crystals and the discussion of these results. The monoclinic double tungstates were soon recognized as very promising for the development of compact and efficient laser sources in the 1-μm spectral range. While first investigations were devoted essentially to crystals doped with the popular Nd^{3+} active ion, the evolution of high brightness laser diodes around 980 nm over the past 20 years recentered the attention on the Yb^{3+} active ion. Continuous-wave (CW) laser operation in Yb-doped KYW and KGdW was first demonstrated, with both Ti:sapphire laser and diode pumping in 1997 [KLS+97].

The most efficient end-pumped laser configuration reported appears to be the pumping of Yb:KGdW and Yb:KYW by a gain-switched Ti:sapphire laser [KLP+97]. In this setup, the slope efficiency reached ~87% and the output yield was around 50%.

As a result of the very large doping ion-ion separation, laser operation at high doping level was also achievable. In particular, it was possible to obtain CW lasing with 100% Yb-doping (stoichiometric KYbW) using a 125 μm thick plate but the too high absorption required pumping away from the absorption peak near 981 nm and the poor heat management resulted in an output power of only 20 mW [KPG+03] [1]. The highest doping level used in a bulk Yb:KYW laser to yield a relatively high (47% slope) efficiency was 30 at. % for a 0.8 mm thick free standing plate for which the output power reached 1.62 W [KTS+06]. This laser was, however, also pumped away from the absorption peak.

Very recently, power scaling was studied using Yb:KGdW under end-pumping with high-power diode bars [HBP+06]. A CW output power of 12.4 W for 26 W of incident pump power with an optical-to-optical efficiency of 47% was achieved using a fiber-coupled pump source. The slope efficiency at this power level was 74% with respect to incident pump power

In the thin disk geometry, very optimistic results using thin disks of 5 and 10% Yb-doped KYW and 5% Yb-doped KGdW lead to a maximum CW output power of 72 W [GSP+07]. However, in this geometry, we are not aware of any demonstration with doping exceeding 10% and thin disk crystal thickness less than 100 μm.

Nevertheless, these very promising results were all achieved with single bulk crystals. Effectively, the very strong anisotropy of the monoclinic double tungstates prevented so far the

1. Note that this experiment does not qualify for a thin disk because the aspect ratio A/h was <1.

successful manufacture of composite crystals. Liquid phase epitaxial layers were first successfully produced based on KYW at the Univesitat Rovira I Virgili (URV), Spain in 2004. CW laser operation for Yb-doping was demonstrated at the Max-Born-Institute, Germany with a 25-μm thick 20 at. % doped KYW layer on a KYW substrate, with an output power of 40 mW [ASA+04].

In order to develop highly doped composite structure with minimum lattice mismatch, bulk Yb-doped KLuW was successfully introduced by the two aforementioned institutes in 2004. In a first step, CW laser operation was demonstrated with Yb:KLuW bulk crystal and output power up to 1 W was achieved [MPA+04]. Afterward, power scaling was studied in a simple plano-concave resonator. A maximum output power of 11.0 W with a slope efficiency of 80 % was obtained, illustrating the potential of KLuW for high power output levels [LPG+07].

While the first two sections (5.1 and 5.2) discuss the characteristic of the emission of monoclinic and tetragonal double tungstates as well as presents the employed setup, the central part of this chapter is detailing further improvements in the development of composite monoclinic double tungstates lasers (section 5.3). In particular, composite lasers based on the KLuW compound are presented for the first time (section 5.3.1 and 5.3.4). Laser operation of composite Yb:KYW/KYW based on segmented growth (section 5.3.2) and diffusion bonding (section 5.3.3) and in a waveguide configuration (section 5.3.5) are, to the best of my knowledge, also first demonstrations.

The following part of this chapter (section 5.4) describes the continuous-wave operation of the tetragonal double tungstate Yb:NaYW. Although the thermal conductibility of such tetragonal tungstates is measured to be low, an output power of more than 16 W has been reported recently with Yb:NaGdW in the thin-disk design [PKPH07]. As we saw in section 3.3, this compound is specially adapted for high tunability and ultrashort pulse generation. Finally, a short comparison and summary of these results will be done in the last section 5.5.

Note that for both the monoclinic and the tetragonal compounds, the results presented here correspond to a selection of the most interesting and representative results obtained throughout this work. The reader avid for more details is advised to refer to the original publications.

5.1 Analytical determination of the inversion and laser emission wavelength

As we saw in the first chapter, the emission wavelength varies with the resonator losses in a quasi-three level laser. In order to predict the emission wavelength and understand better the influence of the crystal length and the doping concentration, it is interesting to consider the relation between the inversion β and the resonator losses composed of the transmission of the output coupler $T_{OC}$and the extra losses L_i.

By taking the expression of the gain derived in equation 2.8 , the round trip gain, after integration along the crystal, can be expressed as follows

$$G = 2\int_0^{l_c} N\sigma_{gain,L}dz = 2l_cN\sigma_{gain,L} = 2l_cN[\beta\sigma_{em,L} - (1-\beta)\sigma_{abs,L}]. \tag{5.1}$$

In case of a CW laser oscillator at or above lasing threshold, the round-trip gain G balances the total attenuation δ so that the relation

$$G = 2l_cN[\beta\sigma_{em,L} - (1-\beta)\sigma_{abs,L}] = -\ln[(1-T_{OC})(1-L_i)] = \delta \tag{5.2}$$

is always fulfilled. If the absorption and emission cross sections are known, it is possible to determine the average inversion parameter along the crystal that is necessary to achieve laser operation for given losses in the resonator. By this means, it is moreover possible to estimate at which wavelength the inversion parameter is minimum indicating minimum threshold in the crystal and thus the laser transition wavelength. Two examples corresponding to experiments that have been performed with the monoclinic double tungstates in this thesis are presented in figure 5.1. For these calculations, the internal losses L_i are assumed to be negligible.

It should be noted that this analysis is based on spectroscopic measurements at room temperature. In lasing operation, a substantial heating of the crystal can occur, which inevitably leads to a modification of the absorption and emission cross sections that will in turn lead to additional shifts of the laser emission wavelength. This is particularly relevant at high power levels with diode-pumping where the behavior can differ from this evaluation.

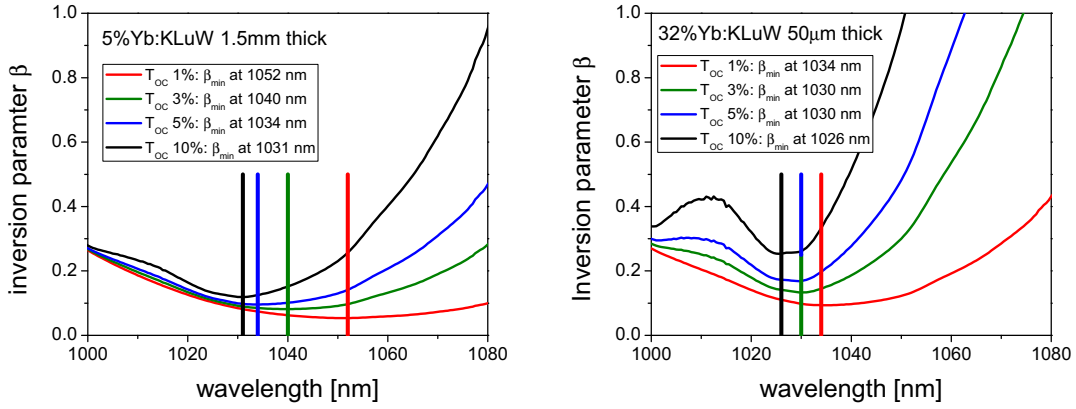

(a) (b)

Figure 5.1: Inversion parameter β (equation 5.2) as a function of the wavelength with different transmissions of the output coupler T_{OC} for (a) a 5 at.% 1.5 mm-thick Yb:KLuW crystal and (b) a 32 at.% 50 μm thick Yb:KLuW crystal. The minimum of each curves corresponds to the predicted oscillation wavelength for two selected Yb:KLuW crystals. For these calculations, the cross sections given in figure 3.8 are used and the extra internal losses L_i are assumed to be equal to 0.

As we can see in these two figures, the behavior can be rather different for the same crystal depending on its length and dopant concentration. On the left, the 5 at.% doped Yb:KLuW with a thickness of 1.5 mm corresponds to a small signal absorption in a single pass configuration of more than 99%. Due to this extremely high absorption, very high pump intensity cannot be maintained easily over the whole length of the crystal and reabsorption losses appear to play an important role. It follows that the average inversion remains rather low and the laser transition encounters an important shift from 1052 nm (for a 1% output coupler) to 1031 nm (for a 10% output coupler). In the second example, the small signal absorption of the 32 at.% doped 50 μm-thick Yb:KLuW crystal is reduced to 75%. In this case, a higher pump intensity along the thin crystal can be preserved leading to higher average inversion and a laser wavelength close to the maximum of the gain for all output couplers. Higher slope efficiency related to the absorbed

power is therefore to expect in the case of the second sample.

Similar consideration can be done with the tetragonal NaYW compound (fig 5.2). As it can be expected, very smooth curves are present in the case of Yb:NaYW due to the inhomogeneous broadening caused by the local disorder in this crystal. In the case considered here, a 1.51 mm thick 6.9 at.% doped Yb:NaYW, a strong dependence of the wavelength on the resonator losses is predicted with an emission wavelength shifting from 1055 nm to 1023 nm as the transmission of the output coupler is increased.

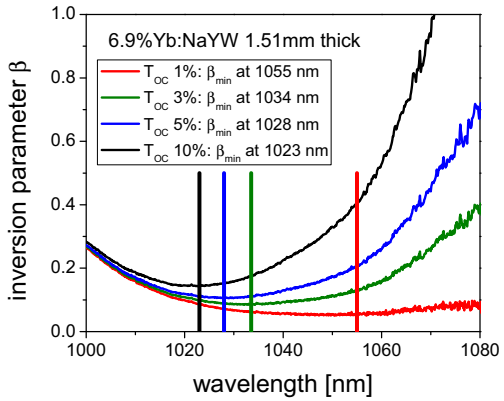

Figure 5.2: Inversion parameter β (equation 5.2) as a function of the wavelength with different transmissions of the output coupler T_{OC} for a 6.9 at.% 1.51 mm-thick Yb:NaYW crystal. The minimum of each curves corresponds to the predicted oscillation wavelength for the selected Yb:NaYW crystal. For these calculations, the cross sections given in figure 3.14 are used and the extra losses L_i are assumed to be equal to 0.

5.2 Experimental Setup

Laser resonator

For the laser investigations, the crystals were placed under Brewster angle between the two curved mirrors (radius of curvature RC=-10 cm) of an astigmatically compensated Z-type cavity (Fig. 5.3). Such cavity is particularly adapted to the investigation of new crystals as it does not require antireflection coating of the active elements and is rather insensitive to imperfect parallelism of the faces of the crystal. Moreover, it can be easily adapted to mode-locking experiments as the two long arms of the cavity present collimated beams where dispersion compensation or saturable absorbers can be implemented.

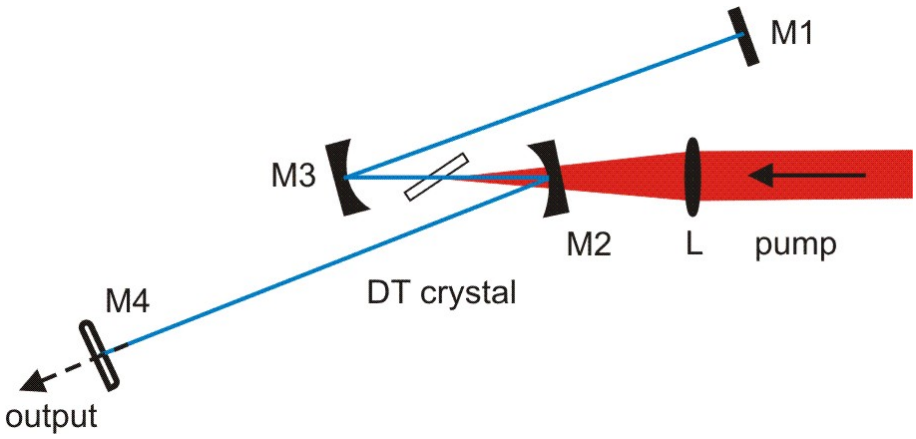

Figure 5.3: Z-shape resonator selected for continuous-wave laser experiments: M1 - planar mirror, M2, M3 - folding mirrors, M4 - output couplers, L - f=6.28 cm focusing lens.

The folding angle of four mirror z-shaped laser cavity has to be adapted to the active crystal depending on its thickness and refractive index [Kan89]. The condition for astigmatism compensation is given by

$$l_c = (R \sin\theta \tan\theta) N^{-1} \tag{5.3}$$

with l_c the crystal thickness, R the radius of curvature of the mirror M1 and M2 and θ the half angle of the folded cavity. In this case, the parameter N is defined as

$$N = (n^2 - 1)(n^2 + 1)^{1/2} n^{-4} \tag{5.4}$$

where n is the refractive index of the active crystal.

Pump sources

Three different pump sources were used with this cavity:

- a Ti:sapphire laser which emitted up to 2 W between 970 and 981 nm with 1 nm linewidth and a beam quality $M^2 \sim 1.2$.
- a tapered diode laser TDL delivering up to 2 W at an $M^2 < 3$ for the slow axis emission. Temperature tuning of this laser was possible between 975-982 nm for operation at maximum power. The emission of the TDL with a spectral bandwidth of only 1 nm was stabilized near 980 nm by feedback of a small amount of the radiation (<0.02%) using a reflection grating. This diode was in the latest experiments replaced by
- a diode laser consisting of a 50 μm broad-stripe single emitter and generating $\sim$ 4 W of output power with a spectral linewidth of about 4 nm. For the collimated beam an M^2 of about 12 was measured.

The astigmatic emission of the diode lasers was collimated by two crossed cylindrical lenses. All three pump lasers were linearly polarized and their output beams were focused by an f=62.8-mm spherical lens through one of the folding mirrors (radius of curvature, RC=-10 cm)

of the resonator. For the Ti:sapphire laser, the pump spot had a Gaussian waist of 35-μm fitting well the parameters of the resonator. In the case of diode-pumping, the pump spot was evaluated to be only slightly larger.

Optical attenuator and isolator

Typically, lasers operating around the threshold exhibit significant fluctuations. Moreover, the temperature, and therefore also the input current, affects the operating wavelength of diode laser due to the change in physical dimensions. In order to operate far from the threshold and at an optimum wavelength, an optical attenuator was implemented. The attenuator is composed of two antiparallel plate with varying reflectivity with varying incident angle. The transmission of the plates changes from > 99% for normal incidence to < 5% for 45°incidence at 981 nm. The two plates rotating in opposite direction permit to avoid a shift in optical path as seen in figure 5.4.

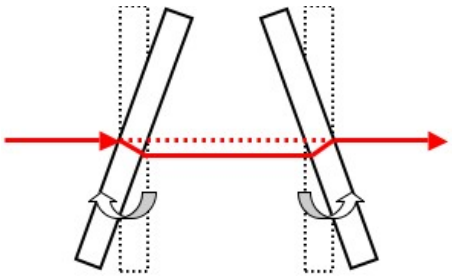

Figure 5.4: Attenuator based on two plates that have varying transmission with incident angle.

An optical isolator was also implemented in order to isolate the pump sources from the Yb laser resonator. With the Ti:sapphire as pump source, a significant coupling between the two laser resonators was noticed. Such effect can be used to enhance the pump power but it is usually connected with strong instabilities and difficulties to measure accurately the actual incident pump power in lasing conditions. An optical feedback when using the laser diode as pump source can be much more detrimental. In our experiement, an important shift of the pump wavelength was noticed, corresponding to an inferior absorption in the active crystal. In the worse case, such optical feedback can even cause the damage of the laser diode. In order to avoid such undesirable effects, a faraday isolator was implemented directly before the focusing lens.
A Faraday isolator consists of three main components, an input polarizer, a Faraday rotator and an output polarizer, as seen in figure 5.5. Faraday isolators, based on the Faraday effect, are passive unidirectional, nonreciprocal devices that utilize the phenomenon of magneto-optic rotation to isolate the pump source. The Faraday effect, manifested as an induced optical activity, is able to rotate the plane of polarization of an input optical beam which propagates parallel to the direction of the magnetic field in the material. The rotation power ρ (angle per unit length) is proportional to the component B of the magnetic flux density in the direction of wave propagation

$$\rho = VB \tag{5.5}$$

where V is the verdet constant for the material. A positive Verdet constant corresponds to

anticlockwise rotation when the direction of propagation is parallel to the magnetic field and to clockwise rotation when the direction of propagation is anti-parallel. Thus, if a ray of light is passed through a material and reflected back through it, the rotation doubles. Thus, a Faraday rotator placed between two polarizers making a 45°angle with each other can be used as an isolator.

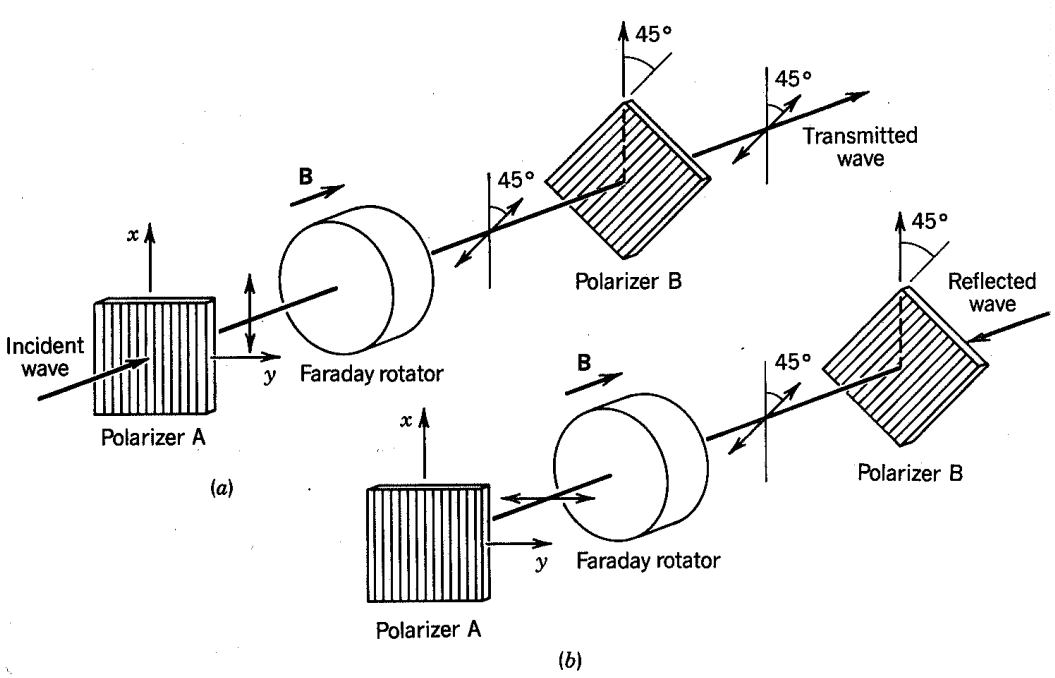

Figure 5.5: An optical isolator using a Faraday rotator transmits light in one direction (a) and blocks the reflected light in the opposite direction (b) from [ST91].

Although the Faraday effect is not itself chromatic, the verdet constant is quite strongly a function of wavelength. The isolators are usually adjustable by varying the degree to which the active rod is inserted into the magnetic field produced by a strong permanent magnet. In this way, the device can be tuned for use with a range of lasers within the design range of the device. In order to have horizontally polarized pump beam, a $\lambda/2$ plate was inserted to rotate the linear polarization to the desired orientation.

Lyot filter

A two-plate Lyot filter placed under Brewster angle was used to tune the laser emission wavelength. Such Lyot filter is made from one or more birefringent plates (usually quartz). In a laser cavity, the plate is tilted to Brewster angle so that p-polarization suffers no loss on the first surface. Due to the birefringence of such plates, the ordinary and extraordinary polarization components of the beam experience a different different phase velocity. Therefore, the polarization state of light with an arbitrary wavelength will in general be modified after a passage through the filter plate. This corresponds to transmission losses, arising from the Fresnel reflection of s-polarized light at the surfaces. For certain wavelengths, however, the optical path

length difference is an integer multiple of the wavelength, so that the losses are very small. Slight rotation of the plate in its plane causes the projections and relative path length to change, thereby changing the wavelength selected. By rotating the plates, one can shift the wavelengths of the transmission peaks and tune the output wavelength of the laser.

5.3 Monoclinic double tungstate lasers with composite crystals

5.3.1 Yb:KLu$(WO_4)_2$ /KLu$(WO_4)_2$ epitaxial lasers

An Yb:KLuW/KLuW epitaxial sample was produced by liquid phase epitaxy (section 4.4.1). The thickness of the Yb:KLuW layer, grown on the (010) face, amounted to 130 μm. For the laser experiments, the (010) faces of the epitaxial crystal were additionally polished with high optical quality, resulting in a layer thickness of 100 μm measured by translating the sample in a ZYGO^{TM} interferometer. The total thickness of the sample amounted to 1.2 mm. Using the ZYGO^{TM}, the surface morphology of the layer of interest exhibited good quality and was flat over large areas. Fig. 5.6 shows the surface profile plot of the (010) epitaxial surface. The radius of curvature of the surface is 0.71 m. The surface roughness with an rms value of 0.8 nm emphasizes the excellent optical quality of the (010) epitaxial surface. No cracks at the epitaxial interface could be identified with the ZYGO^{TM} laser interferometer. The substrate and layer composition was determined by electron probe microanalysis with a CAMECA SX-50 equipment at the URV, Spain. The results obtained show that the Yb content in the layer (7.888×10^{20} Yb^{3+} ions/cm^3) is more or less the same as in the solution, while the Yb content in the substrate is zero, even close to the interface. Thus, the distribution coefficient of Yb^{3+} in these layers is close to unity, which is very favorable for obtaining a homogeneous distribution of ytterbium in the epitaxy. It can be also seen that there is practically no diffusion of Yb^{3+} into the substrate.

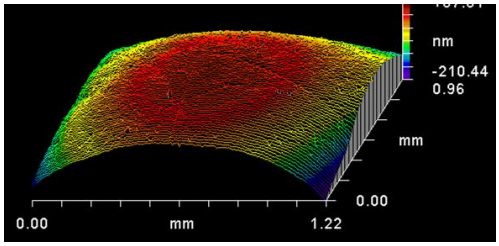

Figure 5.6: Characterization of the epitaxial Yb:KLuW/KLuW crystal. (a) Surface profile plot of the (010) epitaxial layer measured with a ZYGO^{TM} laser interferometer showing a radius of curvature of the surface of 0.71 m and a surface roughness with an rms value of 0.8 nm.

The Yb:KLuW/KLuW crystal was oriented for propagation along the $b(N_p)$ axis with faces parallel to the $N_m - N_g$ plane and polarization along the N_m principal optical axis. The TDL and a Ti:sapphire lasers were used as pumping sources.

Limiting the pump power of the Ti:sapphire laser to 1.85 W (incident on the epitaxy) a maximum output power of 415 mW was achieved with single pass pumping of the 10% Yb-doped

epitaxy using an output coupler of 3% transmission (Fig. 5.7(a)). The resulting pump efficiency was 55% calculated with respect to the absorbed power. The maximum slope efficiency of 66% was achieved with higher output coupling (10%). Both the pump and slope efficiencies were higher in comparison to the previous results with 10% Yb-doped bulk KLuW crystals [MPA+04]. Moreover, the decreased thresholds (of the order of 70 mW absorbed power) and the shorter oscillation wavelength (decreasing from 1040 nm for 1% output coupler to 1026 nm for 10% output coupler) indicate strongly reduced reabsorption of the epitaxy in comparison to the bulk crystals. Even without cooling no damage of this epitaxial crystal occurred regardless of the high power levels (intracavity intensity exceeding 1 MW/cm^2) applied.

Since strong bleaching of the single pass absorption was observed, double pass pumping was implemented, exchanging the end mirror M4 in Fig. 5.3. This really improved the overall absorption and a maximum output power of 515 mW was achieved at 1030 nm with a 3% output coupler.

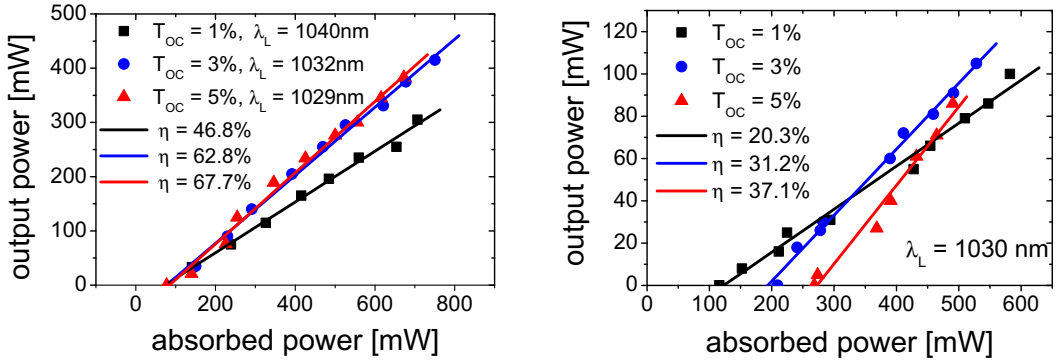

(a) (b)

Figure 5.7: Output power versus absorber pump power of the Yb:KLuW/KLuW laser when pumped with (a) Ti:sapphire and (b) TDL.

Pumping with the TDL in a single pass produced a maximum output power of 105 mW at 1030 nm for a maximum incident pump power of 1.25 W and 3% output coupler (Fig. 5.7(b)). This gives a pump efficiency of 20% with respect to the absorbed power. The highest slope efficiency with respect to the absorbed power was 37.1% using an output coupler of 5% transmission. Thresholds as low as 120 mW (absorbed power) were measured with the 1% output coupler.

5.3.2 Segmented grown $KY(WO_4)_2$ /$KY(WO_4)_2$ laser

For the laser experiments, the (010) face (i.e. the face normal to the crystallographic b axis which coincides with the principal optical axis N_p) of the 13 at. % Yb-doped KYW crystal segment was polished down to 200 μm with high optical quality. The undoped segment was subsequently polished parallel to give a total composite structure thickness of 1.4 mm. The pump spot had a Gaussian waist of 35 μm fitting well the parameters of the resonator which helped to avoid the inclusions in the interface present in segmented grown crystals. The Yb:KYW/KYW sample was mounted on a copper holder without active cooling. It was subsequently oriented for pump (and laser) polarization parallel to the N_m principal optical axis.

It was possible to obtain CW laser operation for output coupler transmission (T_{OC}) between 1% and 10% with laser wavelengths (λ_L) between 1031 and 1024 nm, respectively. The laser performance of the segmented grown Yb:KYW/KYW composite crystal is presented in Fig. 5.8(a). A maximum output power of 375 mW was achieved for an absorbed power of 591 mW and T_{OC}=3%. As no saturation in the output power was observed, further power scaling should be possible. The maximum slope efficiency (η=80%) with respect to the absorbed power was obtained for T_{OC}=5%. The corresponding optical-to-optical efficiency with respect to the absorbed power was 68%. The thresholds for the different output couplers ranged from 139 mW down to only 52 mW of absorbed power for the 1% output coupler.

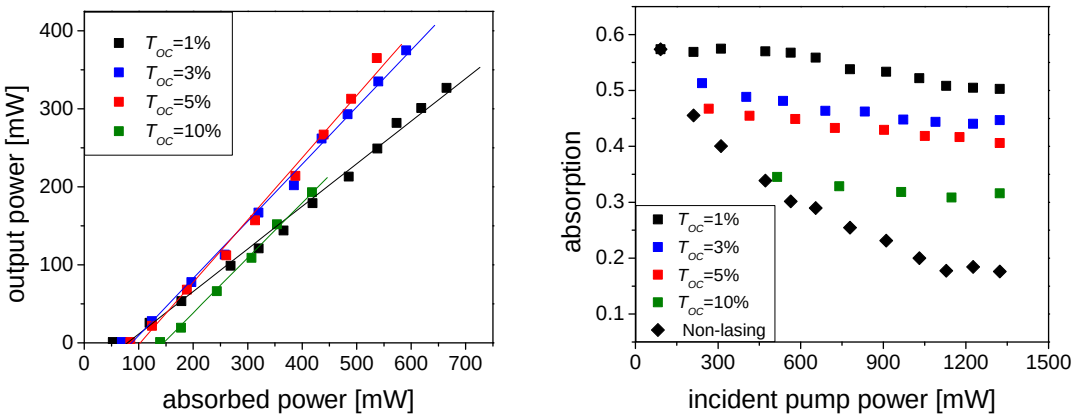

(a) (b)

Figure 5.8: CW output power versus absorbed pump power of the segmented grown Yb:KYW/KYW laser for different output coupler transmission T_{OC}(a), and single pass absorption versus incident pump power (b).

The high slope efficiency together with the very low thresholds obtained with the segmented grown Yb:KYW/KYW composite crystal is an evidence of its high quality as well as the excellent quality of the interface between the two segments, at least those parts which are free of inclusions. Moreover, these results were achieved without active cooling which points out the good thermal management due to the undoped KYW segment.

The absorption was measured in the lasing and non-lasing state, as shown in Fig. 5.8(b). The measurement reveals strong bleaching effect in the non-lasing state as expected from the quasi-three-level nature of ytterbium lasers. The absorption decreases from 57% for low input power down to 18% for maximum incident power. Under lasing conditions, however, the strong bleaching is counterbalanced by the recycling effect, which leads to a decrease in the absorption from 57% to only 50% for the 1% output coupler.

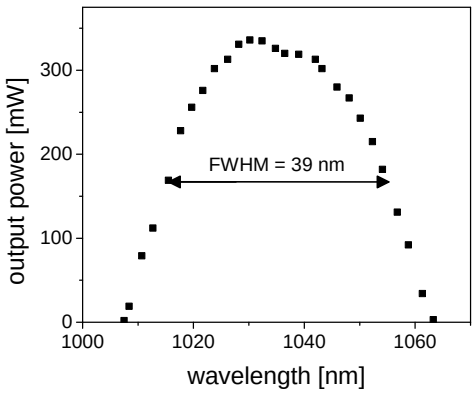

Figure 5.9: Tuning of the Yb:KYW/KYW laser for T_{OC}=1% using an intracavity Lyot filter.

The tunability of the Yb:KYW/KYW laser was investigated by inserting inside the cavity a Lyot filter; a two-plate birefringent filter, under Brewster angle close to the output coupler. At an incident pump power of 1.4 W, laser oscillation with an output coupler of 1% was obtained for wavelengths from 1007 to 1063 nm, as shown in Fig. 5.9. The corresponding FWHM was 39 nm. The broad tunability is an indication of the high potential of segmented grown Yb:KYW/KYW crystals for short pulse generation.

5.3.3 Diffusion bonded $KY(WO_4)_2$ /$KY(WO_4)_2$ laser

For the laser experiments, the {010}-faces of the bonded 5 at.% Yb-doped and undoped KYW part were both polished down to 1.5 mm, giving a total crystal thickness of 3 mm. The plane-parallel {010}-faces of the diffusion-bonded crystal were normal to the N_p-principal optical axis and the sample was first oriented for polarization parallel to N_m and propagation approximately along the N_p-optical axis. The uncoated Yb:KYW/KYW bonded sample had a rectangular aperture of 5.2×4.8 mm^2 (Fig. 5.10).

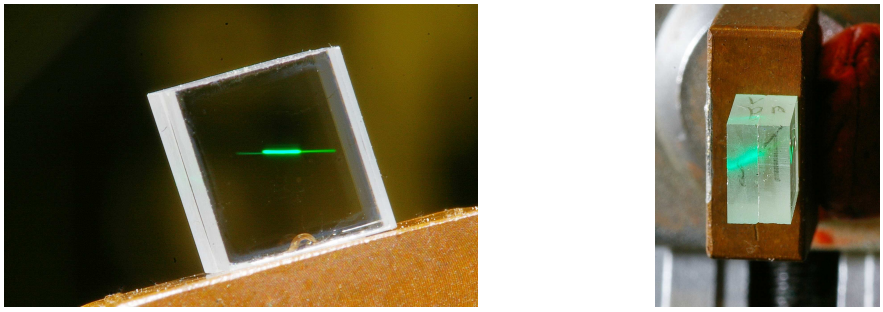

(a) (b)

Figure 5.10: Diffusion bonded KYW crystal in lasing state with (a) a face and (b) a top view. The fluorescence indicates the Yb-doped region.

CW laser operation was obtained for transmissions T_{OC} of the plane output coupler between 1% and 10%. The output power versus the absorbed pump power, measured in the lasing state, for different T_{OC} is shown in Figure 5.11(a). The laser threshold achieved with the bonded Yb:KYW crystal was as low as 81 mW for T_{OC}=1%. The maximum CW output power of 811 mW corresponds to a slope efficiency of 69% with respect to the absorbed pump power. The measured absorption under lasing conditions of the 5% Yb-doped bonded crystal at 981 nm was larger than 98.5% for all output couplers used, so that very similar optical conversion efficiencies of 61% and 60.5% related to the absorbed and input power were obtained, respectively. This indicates a high crystal quality of the Yb-doped KYW part because the strong bleaching effect under non-lasing conditions is nearly compensated by the recycling effect for all output couplers used. The emission wavelength decreased for increased output coupler transmission from 1047 to 1031 nm due to the higher inversion level in the active crystal (Fig. 5.11) as expected from the analysis [2] done in figure 5.1(a).

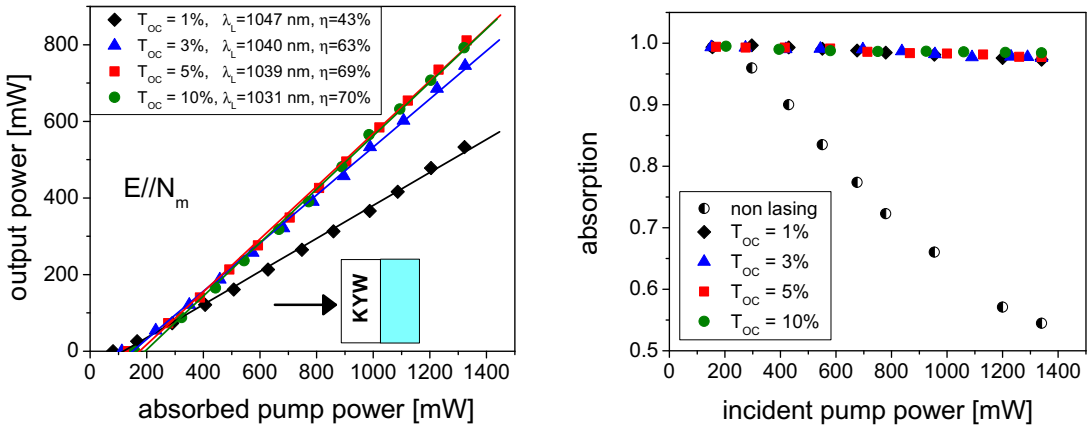

(a) (b)

Figure 5.11: (a) Output power versus absorbed pump power of the Ti:sapphire laser pumped diffusion-bonded Yb:KYW/KYW laser obtained for different transmission of the output coupler and polarization parallel to N_m-optical axis and (b) measured single pass absorption versus the incident pump power under non-lasing and lasing conditions for the used output couplers (b).

To further characterize the bonding quality of the anisotropic crystal, the CW laser performance of the Yb:KYW/KYW structure was investigated by rotating the crystal around the N_p-axis, so that the polarization was parallel to the N_g-optical axis. N_g is the unfavorable orientation compared to N_m due to the more than 5 times lower absorption and emission cross sections.

2. Although this analysis was performed with Yb:KLuW and the experiment with a Yb:KYW crystal, the comparison of the laser wavelength is yet feasible as the spectroscopic variations between these two gain media are minimal.

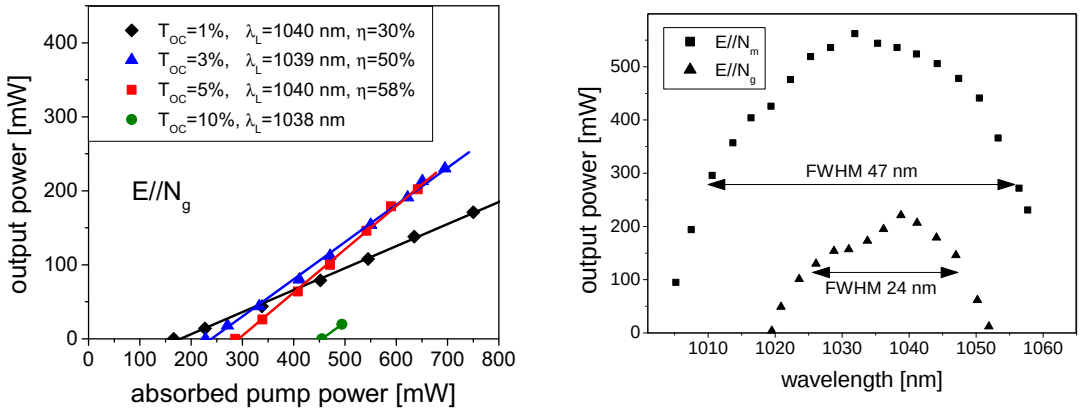

(a) (b)

Figure 5.12: (a) Output power versus absorbed pump power of the Ti:sapphire laser pumped diffusion-bonded Yb:KYW/KYW laser obtained for different output coupler transmissions and polarization parallel to N_g-optical axis. (b) Spectral tuning curves of the CW Yb:KYW/KYW laser with polarization parallel to the N_m and N_g-optical axes for an incident pump power of 1.3 W.

The CW laser operation depicted in figure 5.12(a) are to the best of my knowledge also the first laser demonstration of a monoclinic double tungstate crystal oriented for N_g-polarization. The laser results confirm the expected lower maximum output power and the slightly higher threshold compared to the N_m-orientation. Despite these laser parameters the rather high maximum slope efficiency of 58% indicates the excellent quality of the bonded anisotropic laser crystal.

CW tuning operation of the laser was investigated for the N_m- and N_g-polarization by inserting a birefringent filter in the resonator. For an incident pump power of 1.3 W the laser wavelength was tunable from 1005 to 1058 nm in the case of N_m-polarization and from 1019 to 1052 nm for the N_g-polarization (Fig. 5.12(b)). The broad tunability obtained of up to 47 nm (FWHM) at the present pump power level confirms that bonded Yb:KYW crystals are also promising for the generation of sub-100 fs pulses.

Finally, diode laser pumping of the same diffusion-bonded sample was studied for polarization parallel to the N_m-optical axis with the broad-stripe diode laser (Fig. 5.13). The maximum incident pump power on the composite crystal was limited to 1.6 W. The maximum output power achieved with the diode pumped Yb:KYW/KYW laser was 235 mW corresponding to P_{abs}=1.05 W. In terms of absorbed pump power the maximum slope efficiency amounted to 39% for T_{OC}=10%. The laser wavelength was 1030 nm and got longer for decreasing T_{OC} as in the case of Ti:sapphire laser pumping. The lowest laser threshold achieved was 272 mW for T_{OC}=1%. The measured absorption of 88% was lower compared to Ti:sapphire laser pumping due to the roughly 20-times broader linewidth of the laser diode, exceeding the width of the main Yb:KYW absorption peak at 981 nm. Absorption bleaching took place also in the case of diode-pumping despite the lower pump intensity. The higher thresholds and lower efficiencies in comparison to Ti:sapphire laser pumping are a consequence of the imperfect overlap of the pump and laser modes in the crystal.

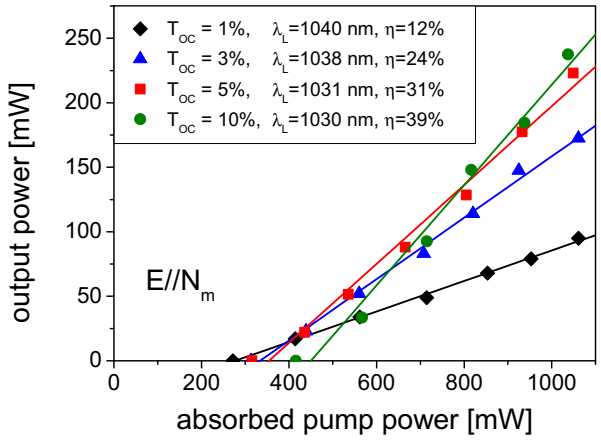

Figure 5.13: Input-output characteristics of the diode-pumped Yb:KYW/KYW laser (symbols) and fits for calculation of the slope efficiencies (lines)

5.3.4 Thin disk Yb:KLu$(WO_4)_2$ /KLu$(WO_4)_2$ lasers

In this section, the first thin disk laser pumped in a single pass in the absorption maximum is presented. It is based on a 50 μm thick epitaxial layer of heavily doped Yb:KLuW grown on a 0.35 mm thick KLuW substrate. A simple plano-concave cavity was employed (Fig. 5.14(a)) to evaluate this thin disk crystal. The unpolarized pump laser used was a fiber-coupled CW diode-bar whose wavelength varied between 973 and 982 nm (linewidth: $\sim$4 nm) with increasing power level. The 200 μm fiber had a NA=0.22 and the maximum power after the f=3 cm optics at the fiber end was 33 W. Two identical samples with 32 at.% Yb-doping and one sample with 48 at.% Yb-doping (measured in the crystal) were investigated. All crystals were b$\equiv N_p$-cut with a diameter of 5 mm and were prepared with the epitaxial side serving as a back side, glued to a copper block with water cooling. One of the 32 at.% Yb-doped samples is shown in Fig. 5.14(b).

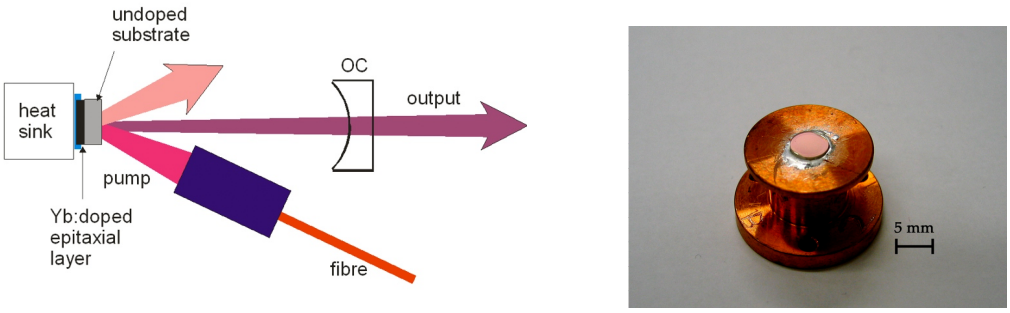

(a) (b)

Figure 5.14: (a) Laser set-up, (b) epitaxial Yb:KLuW sample 1 soldered on a Cu block.

Note that the flatness of the three coated samples (see Fig. 5.15) was roughly an order of

magnitude better in comparison to the conventional 10% Yb-doped, 110-115 μm thick plates of KYW used before by other groups, which showed deformations after coating and focal lengths of the order of 20 cm [LBNG07, PSSM07].

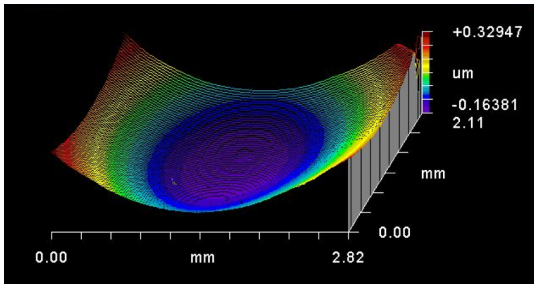

Figure 5.15: Surface profile of the soldered sample measured with a laser interferometer. It indicates focal lengths of -1.4 and -2.1 m in two perpendicular cuts (not correlated with the position of the N_m and N_g principal optical axes).

32 at.% Yb-doped KLuW thin disk

The small signal absorption estimated from the cross sections at 981 nm amounts to ~61% (double pass) for unpolarized light. The thin disk laser was first pumped by directly using the focusing fiber-end optics, as shown in figure 5.14(a). The thin disk sample 1 was positioned behind the focal spot ($2w_0$=340 μm) at a place where the pump diameter had increased to $2w \simeq$500 μm and the pump beam had an angle with the normal of roughly 25°. Optimum performance with an output coupler having a radius of curvature equal to RC=-5 cm was achieved at a cavity length of 42 mm which better matches the two beams on the thin disk but mechanical limitations did not allow to try yet shorter separations.

The obtained input-output characteristics are shown in figure 5.16 for two values of the output coupler transmission T_{OC}. The results are plotted against the measured absorbed pump power under lasing conditions. The absorption of the crystal increased with the pump power basically due to the changing pump wavelength but above 28 W of incident pump power it was almost constant (50-55%) and no bleaching was observed. The two output couplers with T_{OC}=1% and 3% performed almost equally well and there was only a slight wavelength shift from 1033 to 1031 nm at higher T_{OC} as expected from the analysis in figure 5.1(b). The output of the laser was polarized parallel to the N_m-principal optical axis which is related to the maximum gain cross section. The maximum output power of 9 W corresponds to an optical-to-optical efficiency of 53.4%. No saturation in the power dependence is observed, which means that the temperature of the thin disk actually does not increase. However, increasing the output coupler transmission to T_{OC}=5% resulted in crystal crack, which can be attributed to the higher inversion level.

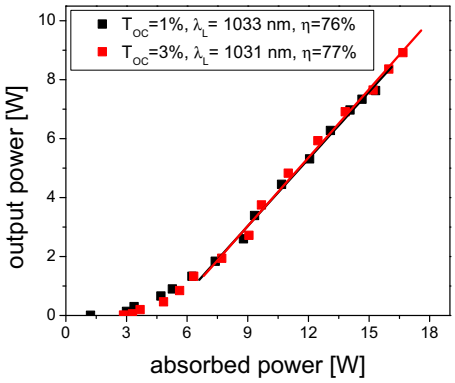

Figure 5.16: CW output power versus absorbed pump power (symbols) and linear fits (lines) to estimate the slope efficiency η.

Therefore, the further experiments with sample 2 were performed at slightly larger pump spots. An additional folding mirror for the pump was used in this case in order to reduce the angle between the pump and laser beams and to enable shorter cavity length. Using again an output coupler with a RC=-5 cm, the actual optimum cavity length was found to be 25 mm, corresponding to maximum resonator waist. In this configuration, a slope efficiency of 67% and a maximum output power of 8.43 W were obtained for T_{OC}=1%, resulting in an optical-to-optical efficiency of 51%, Fig. 5.17(a). With a T_{OC}=3% output coupler the slope efficiency decreased to 58%. The slightly lower efficiencies are related to the larger pump spot size which had a diameter of $2w \simeq$550 μm. The quality of the laser beam was evaluated for T_{OC}=1% and different pump levels. The degree of imperfection of a real beam can be characterized by the dimensionless M^2 parameter. The lower the value of M^2, the closer the beam is to a diffraction-limited TEM_{00} Gaussian beam. The M^2 parameter can be introduced in the equation describing the propagation of a Gaussian beam:

$$w(z) = w_0 \sqrt{1 + \left(\frac{M^2 z \lambda}{\pi w_0^2} \right)^2} \tag{5.6}$$

where w_0 is the waist of the beam, z is the direction of propagation of the beam and λ its wavelength. Thus, the M^2 parameter can be extracted from the measured evolution of the beam radius along the propagation direction.

An M^2 factor of 2.8 was measured at low pump power and it increased to 5.4 at high pump levels. The corresponding output beam diameters measured 23 cm behind the output coupler were 3.7 and 4.8 mm, respectively. This change is related to the increased pump spot size at maximum power.

Minimizing the risk of damage is related to further increase of the pump spot. To investigate this possibility and potentially improve the beam quality, we employed an output coupler with RC=-10 cm and T_{OC}=1%. For a pump spot diameter of $2w \simeq$800 μm, the optimum cavity length giving maximum output power (7.41 W), amounted to 43 mm. The slope efficiency reached 69%, Fig. 5.17(b). The M^2 value at high power (4.8) was found to be slightly lower than with the RC=-5 cm output coupler. By decreasing now the pump spot diameter to $2w \simeq$500 μm in

order to better match it with the fundamental laser mode (calculated waist diameter of 255 μm for a cavity length of 43 mm), laser operation with better beam quality was achieved. In this arrangement, more than 4 W of output power with an M^2 value of 1.8 were obtained for a slope efficiency of 39%. Further optimization of the pump spot size and cavity parameters, by using output couplers with different RC, could possibly lead to even better results.

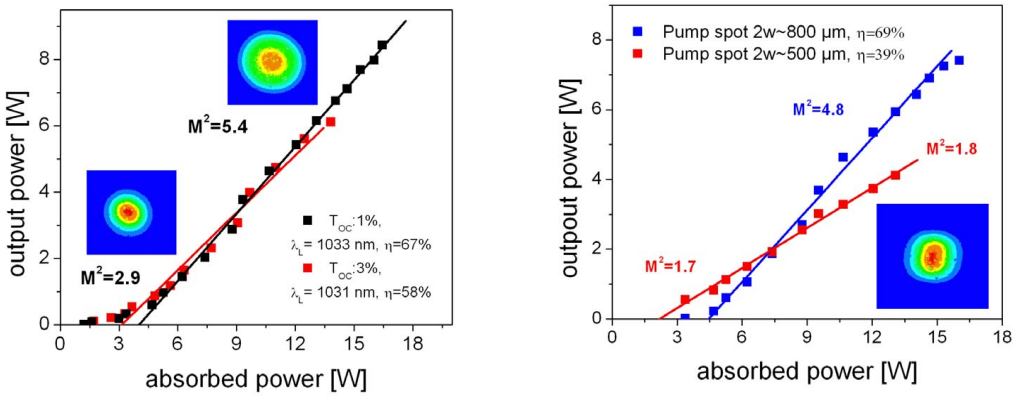

(a) (b)

Figure 5.17: . (a) CW output power versus absorbed pump power for an OC with RC=-5 cm. The far field laser beam profiles with the corresponding M^2 values are indicated for T_{OC}=1% only. (b) CW output power vs. absorbed pump power for a T_{OC}=1% OC with RC=-10 cm: Optimum alignment for maximum output power (blue) and lower M^2 value of the laser output beam (red)

48 at.% Yb-doped KLuW thin disk

For the investigation of a 48 at.%-doped 50 μm-thick sample, the resonator was changed back to a direct pumping configuration as for the investigation of sample 1. The output power was investigated with different transmission of the output couplers and different duty cycles of the chopper. The absorption in lasing condition amounted to ∼70-75% at high pump power. The best performance was obtained with an output coupler of 1% (RC=-10 cm) and a resonator length of 48 mm. Using a chopper with duty cycle of 1/12 , a maximum output power of 306 mW was achieved with a corresponding slope efficiency with respect to the average absorbed power of 30%, see Fig. 5.18(a). For a peak absorbed power of ∼20 W, a strong saturation of the output power versus absorbed power was observed and increasing further the input power prevented lasing operation (without damaging the crystal, however). With 3% output coupler, the performance deteriorated with a slope efficiency of 23% and a strong saturation was observed for absorbed power higher than ∼15 W.

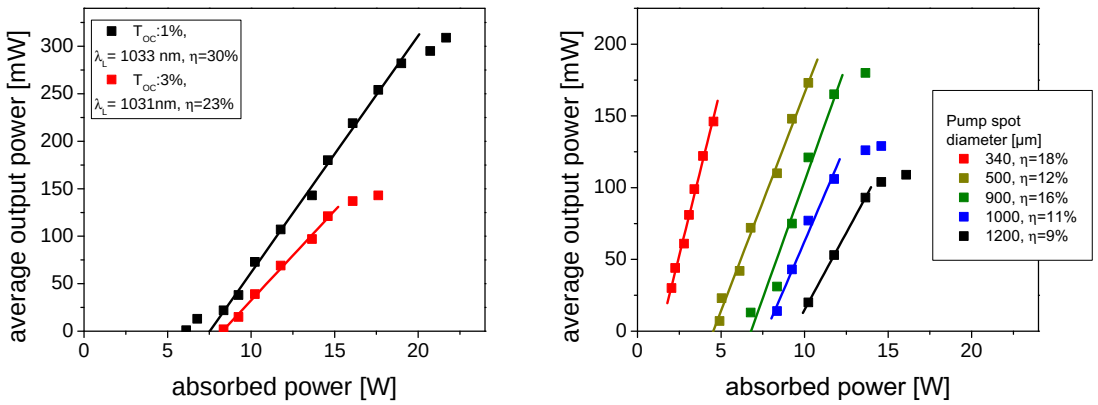

(a) (b)

Figure 5.18: Average output power vs. peak absorbed pump power (a) with a chopper of 1/12 duty cycle and T_{OC} of 1 and 3 %, (b) with a chopper of 1/4 duty cycle and varying pump spot diameter.

Investigation with lower duty cycle (1/4) indicated further deterioration of the laser performance. The slope efficiencies were reduced to 9-18% depending on the diameter of the pump spot and the saturation of the output power occurred very early as seen in figure 5.18(b). A maximum output power of 180 mW was obtained with a pump spot diameter of $\sim$ 900 μm. With 50% chopper, stable laser operation was not achieved and a slightly increase of the input power above the threshold resulted in damaging the crystal.

The very pronounced degradation of the performance of the 48 at.% doped sample denotes very serious thermal problems. The relatively high thickness of the doped layer for such high doping concentration suggests that sufficient heat removal is not possible at the interface between the doped and undoped layers, where the higher temperature rise is expected. The development of yet thinner highly doped layer is expected to improve considerably the heat removal and should not be more critical to produce as the undoped cap provides for the mechanical stability.

5.3.5 Planar Yb:$KY(WO_4)_2$ /$KY(WO_4)_2$ waveguide lasers

One buried (d = 17 μm) and two surface (d = 17 and 35 μm) waveguides with polished end-surfaces, each about 6 mm long and uncoated, were selected for laser experiments. The waveguide orientation corresponded to propagation approximately along the N_g principal optical axis and polarization along the N_m-axis (Fig. 5.19). The samples were mounted on a copper plate without active cooling. The Yb:KYW layers were pumped in a single-pass by a tunable CW Ti:sapphire laser at 980.5 nm. The measured single-pass low-signal absorption of the 1.8 at.% Yb:KYW layer at 981 nm amounted to 56%, in good agreement with the calculated value.

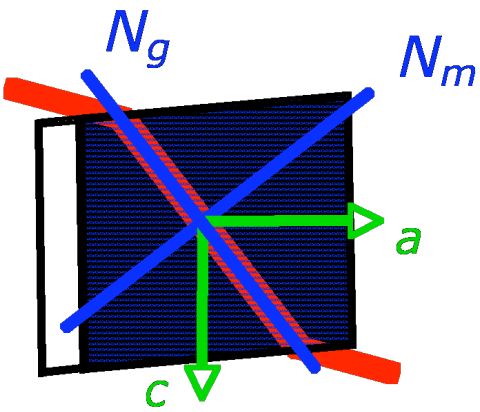

Figure 5.19: Orientation of the Yb-doped planar waveguide.

Independent of the output coupler transmission T_{OC}, which was chosen between T_{OC}= 1.7 and 13.5%, stable CW oscillation near λ_L = 1025 nm could be achieved for all waveguides investigated (Fig. 5.20). Since reabsorption of oscillating laser light in this three-level laser system could be greatly reduced due the high pump-light confinement in the active layer, the spectral laser emission corresponds to the maximum of the gain curve. The output was 95% linearly polarized.

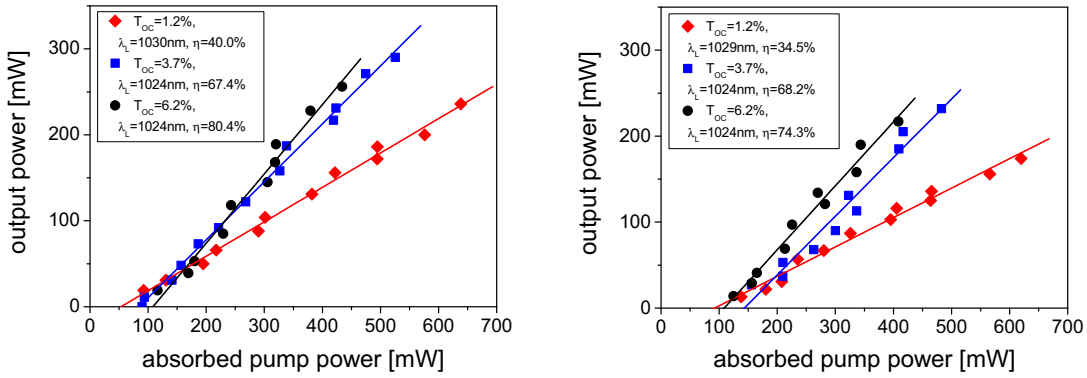

(a) (b)

Figure 5.20: Laser output power versus absorbed pump power of (a) 17-μm thick surface and (b) 17-μm thick buried Yb:KYW planar waveguides for different transmissions of the output coupler.

The best laser performance was achieved with the 17-μm thin surface waveguide doped with 1.2 at.% Yb^{3+}. With a 3.7%-transmission output coupler the laser threshold was only 80 mW of absorbed pump power and the maximum output power amounted to 290 mW, resulting in a slope efficiency versus absorbed pump power of 67.4%. A maximum slope efficiency of 80.4% was obtained for T_{OC}= 6.2%, corresponding to a pump efficiency of 58.9% (Fig. 5.20a)). Although a buried waveguide should in principle exhibit lower propagation losses, the laser performance in the buried 2.4 at.% Yb:KYW waveguide was slightly inferior (Fig. 5.20b)) presumably as a result of the higher doping concentration, which led to higher reabsorption losses. When applying a chopper with a duty cycle of 10%, the output power decreased ten times. Hence, it can be concluded that no thermal problems occur up to the maximum applied pump power of 2 W despite the absence of cooling. A cavity round-trip loss of ~4.8% was derived from the obtained slope efficiencies. Attributing it completely to waveguide propagation losses leads to an upper limit of 0.2 dB cm^{-1} for the waveguide losses.

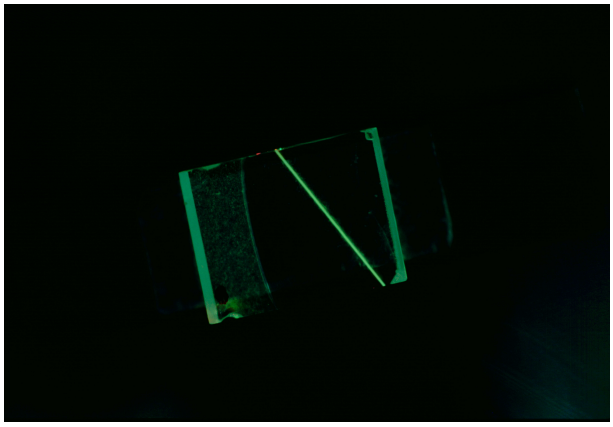

Figure 5.21: Photograph of the Yb:KYW waveguide placed on a Cu-plate in the lasing state.

Despite the highly multimode structure of the waveguide, the observed far-field intensity distribution indicates that the laser output is close to the diffraction limit and the resonator mode is well matched within the physical dimensions of the planar crystal waveguide.

In order to demonstrate the waveguiding effect of the layers, a simple linear laser cavity was used. In this second resonator setup (inset Fig. 5.22), a comparison of the laser performance of bulk and waveguide samples versus the resonator length L was completed. For the chosen, nearly hemispherical resonator with RC of the output coupler equal to -5 cm, the losses are expected to increase rapidly when the resonator length L exceeds this RC and the resonator becomes unstable.

The active media were positioned as close as possible to the plane mirror and index matching was used to minimize the Fresnel loss. The samples were end-pumped through the plane dichroic mirror by the same CW Ti:sapphire laser near 980 nm. The focused pump spot had a waist diameter of 22 μm. The CW output powers measured versus resonator length for an Yb:glass bulk sample and the 17-μm thick Yb:KYW surface waveguide are shown in figure 5.22. The bulk laser operated for resonator lengths between 43 mm and 49.9 mm. No lasing could be achieved for resonator lengths longer than 49.9 mm, as expected from the resonator stability

criterion. When replacing the 6-mm long bulk by the waveguide sample, laser operation could be achieved for resonator lengths extending to 54 mm.

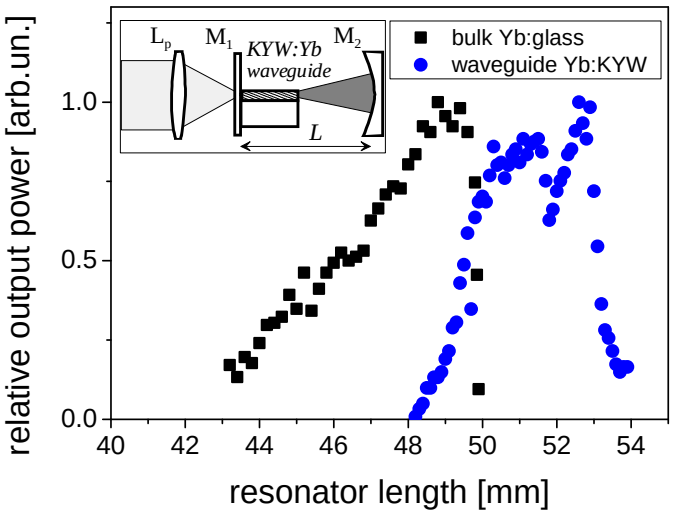

Figure 5.22: Comparison of relative laser output power versus resonator length L for a 6-mm long Yb:glass bulk sample and a 6-mm long 1.2 at.%Yb:KYW surface waveguide. Inset: setup of the linear laser cavity; L_p : focusing pump lens, M_1 : plane dichroic mirror, M_2 : output coupler; (RC = -5 cm).

The shift between the two curves in figure 5.22 indicates that the waist of the resonator mode is moved from the plane mirror to the opposite waveguide end-face without substantially changing the resonator losses, i.e., the laser resonator remains stable even for L $>$ RC. This is a clear indication of the guiding behavior of the active layer.

In this simple resonator configuration, maximum output powers of 158 mW at 1040 nm and 121 mW at 1025 nm for resonator lengths of 48.8 mm and 52.6 mm were obtained at T_{OC}= 1% with the Yb:glass bulk sample and the Yb:KYW waveguide, respectively. The strong decrease of the output powers for smaller resonator lengths is due to the inferior overlap between the pump and resonator modes as well as inferior coupling into the waveguide.

5.4 Tetragonal double tungstate lasers

Throughout this work, several disordered double tungstates and molybdates have been studied. In the case of Yb-doped tetragonal tungstates, the emission cross section is known to increase with decreasing trivalent ion size. The most favorable compound regarding this consideration is NaLuW but unfortunately, it presents incongruent melting requiring a complex growth method. With very similar ionic size along with congruent melting, the NaYW compound is thus potentially most advantageous for efficient CW and mode-locked operation. Thus, results with the Yb:NaYW compound only will be described in the following section.

5.4.1 Yb:NaY$(WO_4)_2$ laser

The Yb-doped NaYW crystals tested were a-cut samples, which allowed to study both σ and π laser polarizations and the pump always had the same polarization as the Yb:NaYW laser. Three different samples with the same Yb concentration but increasing thickness, 0.72, 1.09 and 1.51 mm were tested. Most efficient CW laser operation was obtained with the thickest sample used, which had an absorption of 60% and 75% for the σ and π polarizations, respectively, see Fig. 5.23. Without lasing, the actual pump absorption of this sample was reduced by the bleaching effect. Laser operation had a recycling effect which recovers the pump absorption. This recovery is stronger at higher intracavity intensity, i.e. it increases when decreasing the transmission T_{OC} of the output coupler.

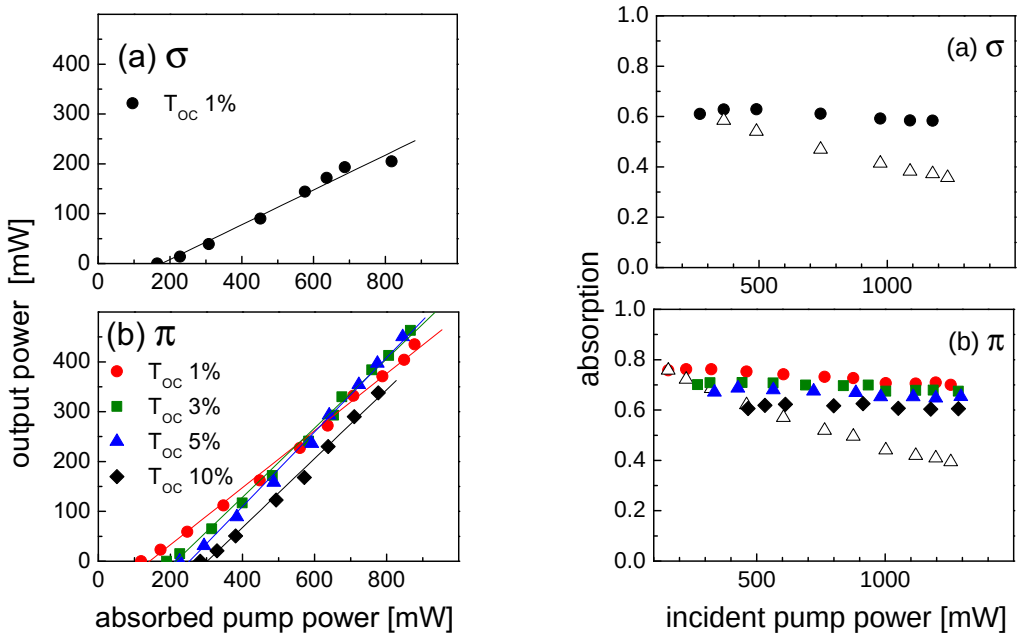

Figure 5.23: Output power versus absorbed pump power at 974.7 nm of the CW Yb:NaYW laser with the 1.51-mm-thick 6.9 % Yb-doped sample for (a) σ - and (b) π-polarization and several output coupler transmissions T_{OC}.

CW laser operation was obtained both for σ and π polarizations, but in the latter case the laser threshold was lower and the output power and slope efficiency were higher for all three samples used. This can be explained by the higher gain cross section for the π -polarization, see Fig. 3.14. The maximum output power achieved for π-polarization with the 1.51 mm thick sample was 463 mW (T_{OC}=3%) for an absorbed power of 866 mW which gives an optical-to-optical efficiency of 53.5%. The slope efficiency was 69.4% with this mirror and it increased to 74.6% for T_{OC}=5%. The laser emission wavelength decreased for smaller values of T_{OC}, from 1045 nm for a 1% output coupler to 1021 nm for a 10% output coupler. This wavelength shift

is approximately expected from the calculation presented in figure 5.2 where a shift between 1055 nm and 1023 nm is given. For this crystal, a very accurate prediction of the wavelength for an output coupler of 1% transmission is, however, difficult to obtain due to the extremely low variation of the inversion in the range between 1040 nm and 1070 nm.

The laser tunability was studied by inserting the Lyot filter. Figure 5.24 shows the results obtained for T_{OC}= 1%. For the π-polarization which provides higher output powers, the full tuning range extends continuously from 1003.7 nm to 1073 nm, with a FWHM of 47 nm.

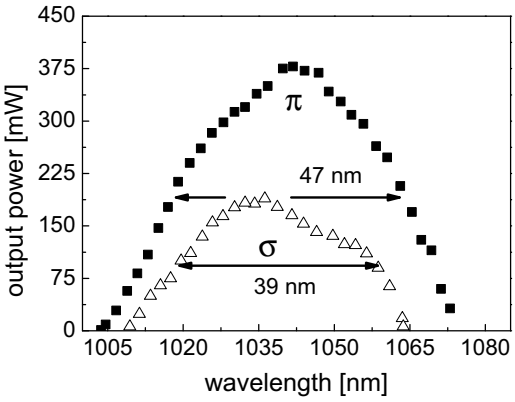

Figure 5.24: Wavelength tunability obtained with the 1.51-mm-thick 6.9 at. % Yb-doped NaYW sample for T_{OC}= 1% and the two polarizations. The incident pump power was ≈1.33 W.

5.5 Comparison and summary of the CW results

Some very new and promising results have been presented in this chapter. More precisely, some composite structures, based on the strongly anisotropic monoclinic double tungstates, have been successfully implemented and laser operation has been achieved with slope efficiencies close to the theoretical limit. In the transversal geometry, laser operation has been studied with composite crystals based on three different production procedures: the liquid phase epitaxy, the segmented growth and the diffusion bonding method. All three methods have leaded to highly efficient laser operation, indicating a great potential for the development of composite geometries based on the monoclinic structure. The good control and versatility of the liquid phase epitaxy technique has also enabled the manufacture of more complex structures such as highly doped thin disk or waveguide geometries by collaborating institutions. In this work, the conitnuous-wave laser performance of these elaborated structures was studied for the first time showing extremely efficient operation. These results demonstrate the great potential of such laser sources for high output power level operation or for integrated optics. With the disordered Yb:NaYW crystal, the first laser operation has also been achieved. The π-polarization has shown to give the best results in term of slope efficiency as expected from the spectroscopic features. Moreover, a very broad tunability has been obtained, confirming the strong potential of this host for femtosecond pulse generation. A comprehensive comparison of the results pre-

sented in this chapter and other results obtained with different laser cavity or gain media will not be done here. Indeed, most of the experiments described are initial results based on new structures or new Yb-doped gain media. Moreover, the cavity used in these experiments is not optimized to demonstrate highly efficient laser operation with high output power but rather adapted for preliminary CW results and subsequent operation in the mode-locked regime.

However, an important information about these results is the absence of saturation in the power dependence (except for the thin disk experiment where the damage of the crystal has been noticed for tight focusing). This indicates that the output power levels achieved with all the crystals investigated do not correspond to an upper limit. Recognizing this, the low threshold and the extremely high slope efficiencies reaching the value of 80 % for the Yb:KYW waveguide and segmented growth structures in particular, indicate the excellence of these results and the high potential for future development of compact and efficient laser sources in the 1 μm spectral range. In table 5.1, the most important results in the CW regime are recapitulated and compared with results obtained previously with bulk Yb:KLuW crystals.

Laser gain media	**Minimum threshold [mW]**	**Maximum slope efficiency [%]**	**Maximum output power [mW]**
Monoclinic structure:			
5%Yb:KLuW bulk laser [MPA+04]	∼270	51	965
10%Yb:KLuW bulk laser [MPA+04]	∼270	50	1010
10% Yb:KLuW epitaxy laser	70	66	515
Segmented grown Yb:KYW laser	**52**	**80**	375
Diffusion bonded Yb:KYW laser	81	70	**811**
Epitaxial thin disk Yb:KLuW laser	∼ 1.2 [W]	77	**9 [W]**
Epitaxial Yb:KYW planar waveguide laser	80	**80.4**	290
Tetragonal structure:			
Yb:NaYW bulk laser π pol	119	69	463

Table 5.1: Comparison of the different lasers studied in this work

Chapter 6

Passive mode-locking

This chapter is devoted to the general theory of passive mode-locking. In the first part of this chapter, the three different mechanisms that can lead to the formation of ultrashort pulses are introduced. Then, the fundamental processes that are involved for passive mode-locking with a slow saturable absorber and without gain saturation are described. In particular, this chapter details the role of the chromatic dispersion, the self-phase modulation as well as the saturable absorber in the pulse formation, shortening and stabilization processes. Finally, in the last section of this chapter, these elements are recapitulated in order to highlight the strong interactions between them and to discuss the stability range of the passive mode-locked regime. This is usually a complex problem when one tries to achieve extremely short pulse durations or very high average output power. Thus, specific features of the gain media, the saturable absorbers or the design of the laser cavity that can help to control or suppress such instabilities are emphasized.

6.1 Pulse formation and temporal shape

The generation of very short pulses from lasers was observed very soon after the demonstration of the first CW laser. A passively Q-switched mode-locked solid-state laser was demonstrated and characterized in 1966 already [DMSH66]. The development of the Ti:sapphire laser in 1986 [Mou86] and later the discovery of Kerr-Lens mode-locking (KLM) [SKS91] of this laser in 1991 pushed the frontier in ultrashort pulse durations into the few femtosecond regime. Kerr-lens-mode-locked Ti:sapphire oscillators are currently very popular but suffer however from a few inherent disadvantages that stimulated the development of new ultrashort lasers sources.

As a matter of fact, KLM is not the most flexible method to generate ultrashort pulses and cannot be adapted to every laser sources. KLM is based on the creation of a self-focusing effect in the crystal that modifies the laser mode profile and produces a saturable absorber effect. Usually, it is required to operate the cavity close to the stability limit so that a high sensitivity to small self-focusing effects is obtained. Furthermore, KLM exhibits problems to self-start from the small fluctuations of the CW operation. This is due to the fact that the peak intensity changes about five orders of magnitude when the laser switches from CW-operation, where the energy is distributed over about 10 ns, to a 100-fs pulse [PK03]. The Kerr-Lens effect depends directly on the third order susceptibility, which is a characteristic of the material. While this mechanism is widely used to mode-lock Ti:sapphire lasers, it can obviously not be extended to all laser hosts

and specially to all wavelengths. The best way to rule out the inherent problems of Kerr-Lens mode-locking is the implementation of saturable absorption modulation based on the ultrafast relaxation of semiconductor devices. In this way, the gain media and the saturable absorber are dissociated offering more optimization and design parameters.

The two aforementioned operational modes are, nevertheless, based on fundamentally different pulse shaping mechanisms. In general, three elementary pulse formation and stabilization mechanisms are distinguished (Fig. 6.1).

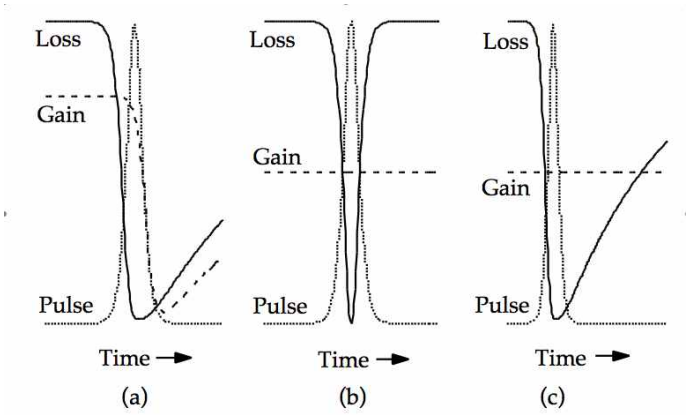

Figure 6.1: Pulse-shaping and stabilization mechanisms due to gain and loss dynamics in a mode-locked laser in case of using: (a) a slow saturable absorber with slow gain saturation, (b) a fast saturable absorber, and (c) a slow saturable absorber without gain saturation, from [KJK96]

(a) Pulse shaping using a slow saturable absorber with slow gain saturation: in such situation, dynamic gain saturation, denoting a fast pulse induced saturation of the gain which recovers between consecutive pulses, contributes to the pulse formation. If the absorber saturates faster than the gain, a net-gain window is offered so that pulse durations much shorter than the absorber recovery time are supported. This mechanism is typically found in dye laser and some semiconductor lasers.

(b) Pulse shaping using a fast saturable absorber: in the case of an ideally fast saturable absorber, self-amplitude modulation directly follows the intensity of the pulse and no dynamic gain saturation is necessary. A short net-gain window is directly produced by the fast recovery time of the saturable absorber. These conditions are found in Kerr-lens mode-locked solid-state lasers as the Kerr effect is known to be almost instantaneous.

(c) Pulse shaping using a slow saturable absorber without gain saturation: in this last situation, the pulse formation is related to the interplay of group velocity dispersion and self-phase modulation. In the case of net intracavity negative dispersion, the effects of dispersion and self-phase modulation can be balanced so that the conditions for soliton propagation are encountered. In this configuration, the saturable absorber essentially provides a starting and stabilization mechanisms. Therefore, a saturable absorber with extremely short relaxation time is not necessary and pulse durations shorter than its recovery time can be generated. This pulse shaping mechanism corresponds to the situation of passively mode-locked solid-state lasers with a semiconductor saturable absorber and is the technique selected to obtain

passive mode-locking in this work.

Although the pulse shaping mechanisms are dissimilar in these three regimes, the theoretical formalism of passive mode-locking can be unified and described with the Haus's master equation formalism [Hau00]. This analytical method consists in the examination of the effect of the different pulse shaping mechanisms such as gain and loss, dispersion, self-phase modulation or saturable absorption on the pulse envelope within a single resonator round trip. For this method, the slow varying envelope approximation is assumed, which requires that the pulse duration is much longer than an oscillation period of the electrical field. If this condition is respected, the various shaping effects can be treated as a modification of the complex envelope $A(z,t)$ of the electric field only. The slow varying envelope approximation is, indeed, appropriate for oscillators based on Ytterbium doped materials where the pulse duration is much longer than an oscillation period.

The case of passive mode-locking with slow saturable absorber without dynamic gain saturation has been notably treated and adapted by Kärtner et al. [KK95, KJK96]. The theoretical approach gives a fundamental relation that is known as a generalized Ginzburg-Landau equation. No analytic solutions to the full master equation are known, however, without the dissipative terms due to gain and losses, the equation reduces to the nonlinear Schrödinger equation. The gain dispersion and losses can then be treated as perturbation of the nonlinear Schrödinger equation. In the particular case of negative group velocity dispersion and positive self-phase modulation, the soliton pulse is a stable solution and a temporal shape which can be described by a secant hyperbolic function

$$A(t) = sech(t/\tau) = \frac{1}{cosh(t/\tau)} \tag{6.1}$$

is found. It follows a fundamental relation between the pulse duration and the spectral width originating from the Fourier transform that connects both values together. For a secant hyperbolic pulse shape it can be expressed as

$$1.76\tau\Delta\nu = \tau_{FWHM}\Delta\nu \geq 0.315 \tag{6.2}$$

where τ_{FWHM} and $\Delta\nu$ are the pulse duration and spectral width measured at Full Width at Half Maximum, respectively. This time-bandwidth product indicates how close the pulse duration is to the limit which is set by its spectral width. As a result, a bandwidth-limited pulse is associated with a minimum time-bandwidth product, while higher values indicate uncompensated chirp.

Now that the basic concepts of passive mode-locking are described, let us detail the principal mechanisms responsible for the pulse formation in an Yb-doped passively mode-locked medium with a slow saturable absorber. As we just saw, three aspects are fundamental for soliton formation and stabilization, i) the chromatic dispersion (section 6.2), ii) the self-phase modulation (section 6.3) and iii) the semiconductor saturable absorber (section 6.4).

6.2 Dispersion

Dispersive media are characterized by a frequency-dependent susceptibility $\chi(\omega)$ (and therefore refractive index $n(\omega)$). On a fundamental level, this dependence arises from resonances in the medium that are related to the motion of bound electrons. Dispersion plays a crucial role in

the propagation of short pulses as each frequency components of a short light pulse experiences a different time delay so that the pulse is finally dispersed in time and its width broadens (Fig. 6.2)

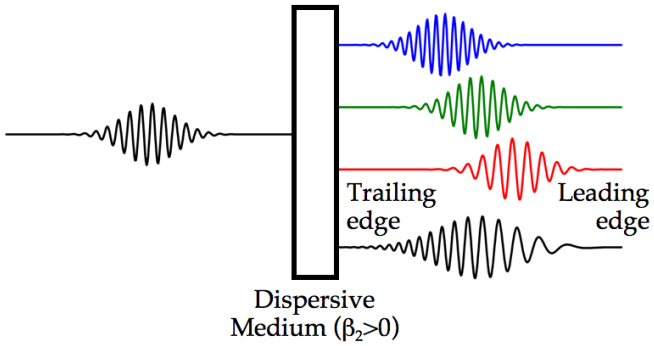

Figure 6.2: Pulse broadening in a dispersive medium.

Dispersive pulse broadening

Let us consider an optical pulse with linear polarization propagating in the z direction. It can be described as

$$E(z,t) = \frac{1}{2}A(z,t)exp(i\{\omega_0 t - k_0 z\}) \tag{6.3}$$

with $A(z,t)$, the complex envelope which can be generally written as a combination of an instantaneous amplitude $|A(z,t)|$ and a term incorporating the instantaneous phase $\phi(t,z)$ as follow.

$$A(z,t) = |A(z,t)|exp(i\phi(z,t)) \tag{6.4}$$

As we have seen, the fundamental theory of passive mode-locking predicts secant hyperbolic pulse shape. Unfortunately, no analytic solution of the propagation equation exists for such pulse shape. However, Gaussian and secant hyperbolic pulse shape present a lot of similarities so that the results obtained assuming Gaussian pulse can be extended phenomenologically to secant hyperbolic pulse shape. Let us then consider an initially unchirped Gaussian pulse, the complex envelope $A(z,t)$ before propagation in a medium can be expressed as

$$A(0,t) = A_0 exp\left(-\frac{t^2}{2\tau_0^2}\right) exp(i\phi(t)). \tag{6.5}$$

In a transparent and dispersive medium, the instantaneous phase ϕ of a pulse propagating in the z direction can be written

$$\phi(\omega) = k(\omega)z \tag{6.6}$$

where the wave number $k(\omega)$ depends on the frequency and can be written in a Taylor series expansion:

$$k(\omega) = k(\omega_0) + k'(\Delta\omega) + \frac{1}{2}k''(\Delta\omega)^2 + \frac{1}{6}k'''(\Delta\omega)^3 + ... \tag{6.7}$$

with $\Delta\omega = \omega - \omega_0$, $\beta_1 \equiv k' = \frac{\partial k}{\partial w}|_{\omega=\omega_0}$, $\beta_2 \equiv k'' = \frac{\partial^2 k}{\partial \omega^2}|_{\omega=\omega_0}$, and $\beta_3 \equiv k''' = \frac{\partial^3 k}{\partial \omega^3}|_{\omega=\omega_0}$.

The first derivative $\beta_1 \equiv k'$ corresponds to the group delay and is responsible for an overall time delay that has no influence on the pulse shape. As we will see in detail in the following section, the second derivative $\beta_2 \equiv k''$ is equivalent to the group velocity dispersion (GVD) or to the group delay dispersion (GDD) per unit length and is responsible for a pulse broadening. In general, in the visible and near infrared spectral region, dielectric media exhibit a decrease of the group velocity with increasing frequency so that positive group velocity dispersion (β_2>0) is obtained. In the opposite case, that is for β_2 <0, negative group velocity dispersion is achieved.

If one, at first, considers only the second order dispersion (β_3 and higher order terms = 0) and neglects nonlinear terms, the analytic expression for the complex envelope after propagation in a dispersive medium of length z can be written [Agr01]:

$$A(z,t) = \frac{\tau_0^2}{\tau_0^2 - i\beta_2 z} exp\left(-\frac{t^2}{2(\tau_0^2 - i\beta_2 z)}\right). \tag{6.8}$$

Thus, the shape of a Gaussian pulse is maintained on propagation but its width increases in a dispersive medium. Moreover, it gives rise to a linear frequency chirp, i.e. a frequency that changes linearly across the pulse. This linear chirp depends on the sign of the group velocity dispersion. For positive GVD (β_2>0), the instantaneous frequency increases linearly across the pulse and the opposite occurs for negative GVD ($\beta_2 < 0$). Finally, the pulse broadens with a related broadening factor τ_1/τ_0 of

$$\frac{\tau_1}{\tau_0} = \sqrt{1 + (\frac{\beta_2 z}{\tau_0^2})^2} \tag{6.9}$$

where τ_0 and τ_1 are the half widths at 1/e.

Similar consideration including the third order dispersion (TOD) shows that distortion of the pulse shape occurs. In that case, the shape becomes asymmetric with oscillatory structure near one of its edges, depending on the sign of the third order dispersion term. For the case of positive β_3, the oscillations appear near the trailing edge of the pulse. Analysis of the pulse broadening effect of the second and third order dispersion on an initially unchirped Gaussian pulse is also possible. However, as distortions of the pulse appear due to higher order dispersion terms, 1/e or the FWHM evaluation of the pulse duration cannot be used properly anymore. The rms width, defined by $\sigma = (< \tau^2 > - < \tau >^2)^{1/2}$, has therefore to be introduced so that finally the expression giving the pulse broadening is

$$\frac{\sigma_1}{\sigma_0} = \sqrt{1 + (\frac{\beta_2 z}{\tau_0^2})^2 + (\frac{\beta_3 z}{2\tau_0^3})^2} \tag{6.10}$$

where σ_0 and σ_1 are this time the rms widths of the pulse.

In order to better apprehend the effect of GDD and TOD, one can plot the pulse broadening factor for femtosecond pulses due to both order of dispersion (Fig. 6.3). The left figure considering the group delay dispersion GDD, that is the GVD multiplied by the length of the dispersive media ($\beta_2 z$), shows that compensation of the second order dispersion is essential for sub 100 fs pulse generation. Effectively, one can see that an initial pulse duration of 50 fs (FWHM) is broadened by a factor $\sim$1.5 after only 1000 fs^2, which corresponds to a propagation in less than 1 cm of KLuW as we will see. In a laser resonator, as the pulse executes numerous round-trips within the cavity lifetime, second order dispersion becomes rapidly critical and its compensation is indispensable. On the other hand, one can see on the second figure that the influence of the TOD is, as expected, much lower and plays an important role for very short pulse duration only.

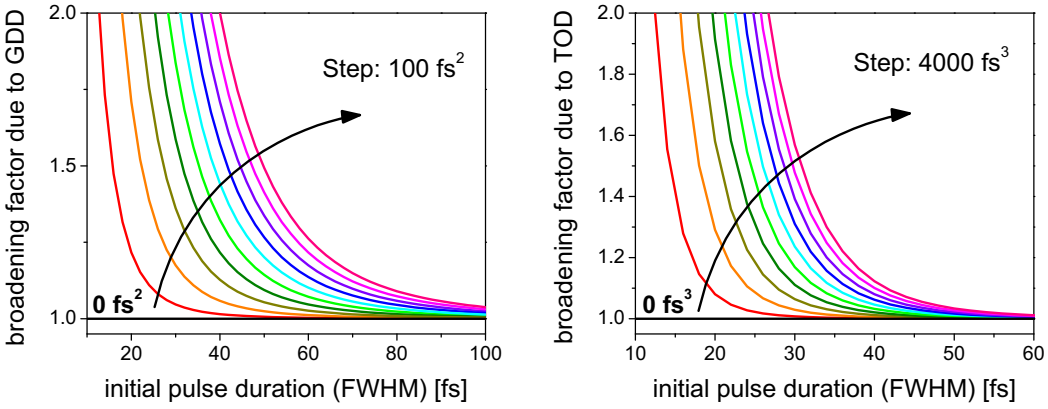

(a) (b)

Figure 6.3: Dispersive pulse broadening due to the group delay dispersion and third order dispersion. The broadening factor $\frac{\sigma_1}{\sigma_0}$ as given by equation 6.10 is plotted for different initial pulse durations taking into account (a) the GDD ($\beta_3 = 0$) and (b) the TOD ($\beta_2 = 0$) only. Between two lines, steps of 100 fs^2 and 4000 fs^3 are considered for the second and third order dispersion, respectively.

Dispersion introduced by double tungstates

In order to perceive the amount of dispersion that can be introduced by the gain media, it is interesting to calculate the different orders of dispersion for both the monoclinic KLuW and tetragonal NaYW double tungstates. Away from the resonance, the dependance of the refractive index with the wavelength can be well approximated with the Sellmeier equation [1]. Hence the second and third order dispersion can be calculated with the Sellmeier coefficients that have been presented in chapter 3 for each host. The derivations can be expressed as a function of the refractive index $n(\lambda)$ using the relation $k = \frac{n\omega}{c} = \frac{2\pi n}{\lambda}$.

1. Actually Yb-doping of these crystals gives rise to a new resonance around 1μm that will generate some additional modulation in this spectral range. This effect is however neglected here

1^{st} order, group delay:

$$\beta_1 \equiv k' = \frac{1}{c}\left(n + \omega\frac{dn}{d\omega}\right) = \frac{n}{c}\left(1 - \frac{dn}{d\lambda}\frac{\lambda}{n}\right) \tag{6.11}$$

2^{nd} order, group velocity dispersion GVD:

$$\beta_2 \equiv k'' = \frac{1}{c}\left(2\frac{dn}{d\omega} + \omega\frac{d^2n}{d\omega^2}\right) \simeq \frac{\lambda^3}{2\pi c^2}\frac{d^2n}{d\lambda^2} \tag{6.12}$$

3^{rd} order dispersion TOD:

$$\beta_3 \equiv k''' \simeq \frac{-\lambda^4}{4\pi^2 c^3}\left(3\frac{d^2n}{d\lambda^2} + \lambda\frac{d^3n}{d\lambda^3}\right) \tag{6.13}$$

The curves for the GVD and TOD for both compounds are shown in figure 6.4 and 6.5, respectively.

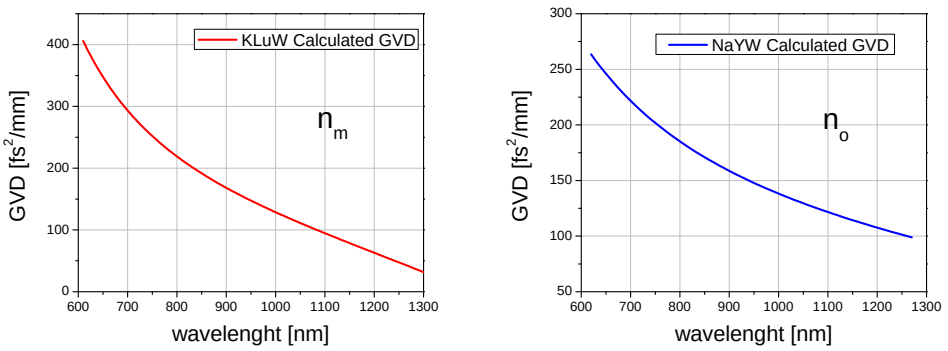

(a) (b)

Figure 6.4: Group velocity dispersion introduced by the KLuW (a) and the NaYW double tungstates (b). The Sellmeier coefficient used to calculate the different order of dispersion are given in table 3.1 and figure 3.12 for the KLuW and NaYW, respectively.

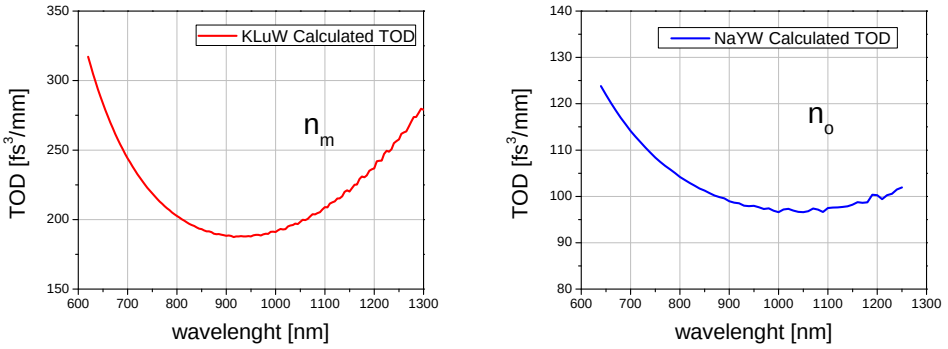

(a) (b)

Figure 6.5: Third order dispersion introduced by the KLuW (a) and the NaYW double tungstates (b). The Sellmeier coefficient used to calculate the different order of dispersion are given in table 3.1 and figure 3.12 for the KLuW and NaYW, respectively.

As expected, both the GVD and TOD are positive in the visible and near infrared and decrease with increasing wavelength. At 1040 nm, the group velocity dispersion amounts to 115 fs^2/mm in KLuW and 131 fs^2/mm in NaYW. These values are high compared to most other insulating crystals that exhibit a larger band gap. This shows once again the importance of an effective method to generate negative GDD inside the resonator.

The third order dispersion amounts to 197 fs^3/mm and 97 fs^3/mm for the KLuW and NaYW compounds, respectively. It can be seen that these values are negligible when compared to the amount of TOD that leads to substantial broadening of femtosecond pulses.

Dispersion compensation

As we just saw, obtaining transform limited pulse in the femtosecond regime requires intracavity dispersion compensation. In the visible and near infrared region, positive GDD (β_2>0) is normally introduced by the gain material so that methods generating negative GDD have to be implemented. For this purpose, many different methods have been developed, the most common being Gires-Tournois Interferometer (GTI) [GT64], chirped mirror [SFSK94] and prism pair compressor [FMG84]. While most of the methods allow only a stepwise increase of the second order dispersion, the prism compressor is a very convenient method that allows the continuous adjustment of the dispersion over a certain range by control of the insertion of the prisms into the beam. This can be a substantial advantage in order to reach the optimum dispersion compensation as new gain media are investigated, in which the chromatic dispersion is usually not well characterized [2].

The prism compressor consists of two prisms that are placed in opposition and aligned for minimum deviation (Fig 6.6). The dispersion consists of two terms, the positive dispersion introduced by the beam path in the two prisms and the negative dispersion introduced by the

2. The saturable absorber mirror can also add some substantial amount of dispersion. Effectively, the nonlinear refractive index n_2 is typically an order of magnitude higher in semiconductor than in insulating crystals. Additionally, the antiresonant structure of the saturable absorber itself may introduce some GTI effect. The transient response of the saturable absorber to a short light pulse with the generation of free carriers renders the accurate analysis very difficult and confirms the importance to implement a method permitting a continuous adjustment of the dispersion.

angular dispersion of the prisms. Effectively, it can be seen that the refraction is stronger for shorter wavelength leading to a larger optical path and therefore a longer delay. By reflecting the beams back through the original prism pair with a mirror (or the output coupler in our case), the beams can be spatially recombined and the dispersion is doubled.

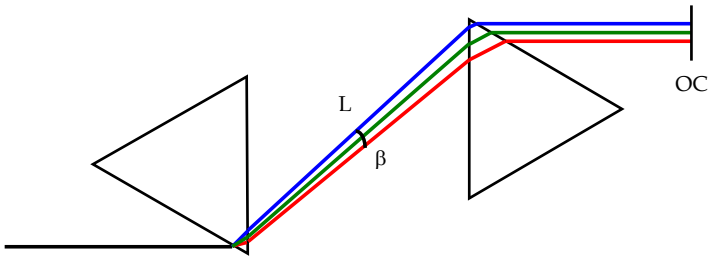

Figure 6.6: Negative dispersion obtained with a prism pair.

If one takes into account the back and forth passes into the prism pair, the second order dispersion can be written in a similar way as in equation 6.12

$$\frac{d^2\phi}{d\omega^2} = \frac{\lambda^3}{2\pi c^2}\frac{d^2P}{d\lambda^2} \tag{6.14}$$

where $P = L\cos\beta$ is the total optical path that contributes to the dispersion. The second derivative of P can be re-expressed as

$$\frac{d^2P}{d\lambda^2} = 2\left[\frac{\partial^2 n}{\partial\lambda^2}\left(\frac{\partial\theta_2}{\partial n}\right)\left(\frac{\partial^2\theta_2}{\partial n^2}\right)\left(\frac{\partial n}{\partial\lambda}\right)^2\right] L\sin\beta - 2\left(\frac{\partial\theta_2}{\partial n}\frac{\partial n}{\partial\lambda}\right)^2 L\cos\beta \tag{6.15}$$

with L, the distance between the two prisms apices and β, the angle between the beam that passes from apex to apex and the other ray considered. For minimum deviation and Brewster-angle incidence, this expression can be simplified and becomes

$$\frac{d^2P}{d\lambda^2} \approx 4\left[\frac{\partial^2 n}{\partial\lambda^2} + \left(2n - \frac{1}{n^3}\right)\left(\frac{\partial n}{\partial\lambda}\right)^2\right] L\sin\beta - 8\left(\frac{\partial n}{\partial\lambda}\right)^2 L\cos\beta. \tag{6.16}$$

In this expression, the first term corresponds to the normal dispersion that is introduced by the material itself while the second term corresponds to the angular dispersion. For a tip-to-tip distance L large enough, the angular dispersion counterbalances the chromatic dispersion of the material so that overall negative group delay dispersion is obtained. The amount of negative GDD that can be obtained with a prism pair depends then directly on the tip-to-tip distance and dispersive nature of the material (second term $\propto \left(\frac{\partial n}{\partial\lambda}\right)^2$). Highly dispersive material such as SF10 is usually selected for the prisms in the IR so that sufficient negative GDD is achieved for a reasonable distance between them and a compact setup is obtained.

With a similar approach, the third order dispersion TOD of a prism pair in a double pass configuration can be calculated following equation 6.13

$$\frac{d^3\phi}{d\omega^3} = \frac{-\lambda^4}{4\pi^2 c^3}\left(3\frac{d^2P}{d\lambda^2} + \lambda\frac{d^3P}{d\lambda^3}\right) \tag{6.17}$$

and the third derivative of the total optical path for minimum deviation and Brewster-angle incidence becomes

$$\frac{d^3P}{d\lambda^3} \approx 4\frac{d^3n}{d\lambda^3}L\sin\beta - 24\frac{dn}{d\lambda}\frac{d^2n}{d\lambda^2}L\cos\beta. \tag{6.18}$$

The terms related to the normal dispersion of the material (first term of the equation) and the angular dispersion (second term of the equation) become apparent again in this expression. The term $L\sin\beta$ expresses the distance between the two extreme beams into the second prism. By introducing $L\sin\beta = 4w$, where w is the beam radius and $\cos\beta \approx 1$ and finally assuming a beam radius $w = 1$ mm, all the terms contributing to the GDD and TOD can be easily estimated. The GDD and TOD generated by two SF10 prisms are shown in Figure 6.7 for several tip-to-tip separation.

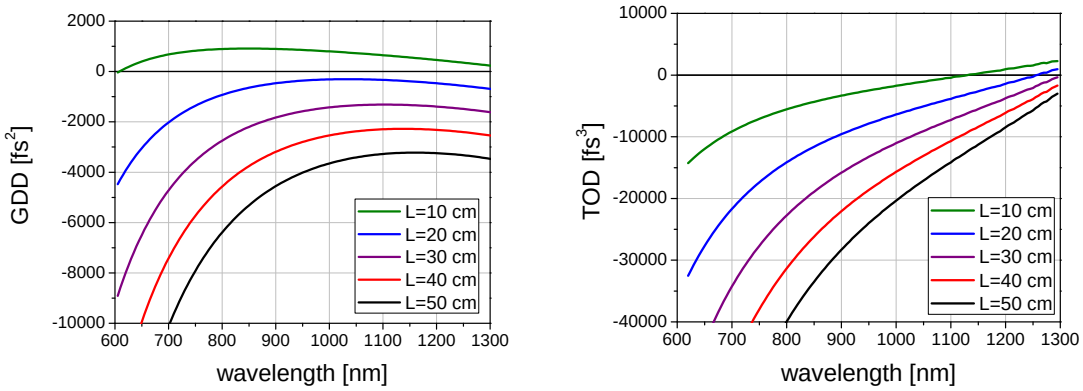

(a) (b)

Figure 6.7: Calculated GDD and TOD obtained from a SF10 prism pair with different separations (equations 6.14, 6.16 6.17 and 6.18). Minimum deviation and Brewster-incidence is assumed. The Sellmeier coefficients of the SF10 glass used for the calculations are given in the Appendix.

As expected from the above expressions, a negative GDD is obtained at all wavelengths for a tip-to-tip separation larger than 20 cm. For a separation of 40 cm, a negative group velocity dispersion of approximately -2400 fs^2 is generated per round-trip at 1040 nm. This negative GDD can be reduced by further insertion of the prisms as each supplementary millimeter into the prism adds +215 fs^2. It can also be seen that for a similar separation, the third order dispersion induced by the SF10 prism compressor is significant and amounts to as much as -13600 fs^3 per round-trip. Each supplementary millimeter of SF10 would introduce only +198 fs^3. Although we have seen that the gain material does not introduce critical third order dispersion

for pulse durations that are considered here, we see that the prism compressor, depending on prism material, introduces a large amount of third order dispersion that can play a critical role.

6.3 Self-phase modulation

For a nonlinear material , the electric polarization field **P** will not depend linearly on the electric field **E**. The polarization can be expressed by a Taylor series with coefficients corresponding to the nonlinear susceptibilities:

$$\mathbf{P} = \epsilon_0 \left(\chi^{(1)}\mathbf{E} + \chi^{(2)}\mathbf{EE} + \chi^{(3)}\mathbf{EEE} + \dots \right) \tag{6.19}$$

In a Kerr medium, the third order susceptibility gives an intensity dependent refractive index

$$n(I) = n_0 + n_2 I(r,t) \qquad \text{with} \qquad n_2 = \frac{3}{8n}\chi^{(3)} \tag{6.20}$$

While the Kerr lensing effect refers to the radial variation of the refractive index in function of the intensity, self-phase modulation (SPM) is related to the time-varying refractive index. If the effect of dispersion is neglected, the pulse shape remains unchanged after propagation but the SPM produces a time-varying refractive index and the intensity-dependent phase shift ϕ can be written as

$$\phi = -\frac{2\pi}{\lambda} n(I) z = -\frac{2\pi}{\lambda} \left(n_0 + n_2 I(t) \right) z = \frac{2\pi}{\lambda} n_0 z - \gamma |A(t)|^2 \tag{6.21}$$

where γ is defined as the self-phase modulation coefficient. For a Gaussian pulse the on-axis intensity dependent phase ϕ becomes

$$\phi = \frac{2\pi n_0}{\lambda} z + \frac{2\pi n_2}{\lambda} z I_0 exp\left(-\frac{t^2}{\tau^2} \right). \tag{6.22}$$

Consequently, new frequencies are generated by SPM and the instantaneous optical frequency differs across the pulse from its central frequency ω_0 by a difference

$$\delta\omega(t) = -\frac{\partial\phi}{\partial t} = \frac{4\pi n_2 I_0 z}{\lambda} \frac{t}{\tau^2} exp\left(-\frac{t^2}{\tau^2} \right) = \frac{4 n_2 z P_o}{\lambda w^2} \frac{t}{\tau^2} exp\left(-\frac{t^2}{\tau^2} \right) = \gamma P_0 \frac{t}{\tau_0^2} exp\left(-\frac{t}{\tau_0} \right)^2 \tag{6.23}$$

where we used the relation of the peak intensity of a Gaussian beam $I_0 = 2P_0/\pi w^2$ [PK03]. The intensity $I(t)$ as well as the variation of the optical frequency $\delta\omega(t)$ can be plotted assuming a Gaussian pulse shape (Fig. 6.8)

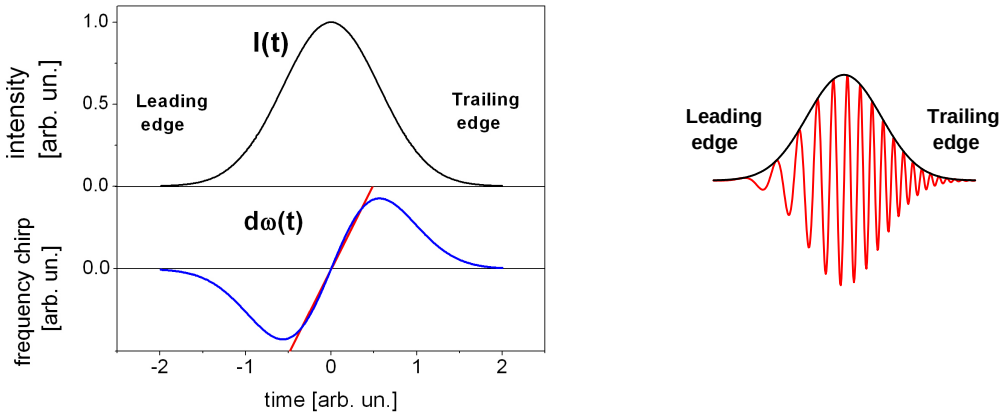

Figure 6.8: Effect of the self-phase modulation on an initially unchirped Gaussian pulse.

In this figure, we can see that, due to self-phase modulation, lower frequencies are generated at the leading edge of the pulse and, on the opposite, higher frequencies are generated at the trailing edge of the pulse. More important for the case of passive mode-locking operation, it can be seen that SPM induces a nearly linear increase of the frequency in the center of the pulse. Thus it is to understand that linear chirp induced by SPM and GDD can balance each other for certain particular conditions.

In a laser cavity, if moderate net negative GDD is obtained, the linear chirp induced by SPM and GDD compensate each other and the so-called fundamental soliton can be achieved. In this case, the pulse propagates in the medium with constant temporal and spectral shape. In the case of a sech^2 temporal profile, the fundamental soliton is formed for a certain amount of negative GDD that satisfies the condition

$$\tau = \frac{2|\beta_2|l_c}{|\gamma|E_p} \tag{6.24}$$

for an interactivity pulse energy E_p and a crystal length l_c.

Values of the nonlinear refractive index n_2 are typically of the order of 10^{-16} cm^2/W for most laser host materials. The nonlinear refractive index can be extrapolated from the value of the band-gap, by using the Kramers-Krönig theory developed for semiconductors [SHHV91]. Such model and initial measurements done with Yb:KGdW and KYW seems to confirm that the nonlinear refractive index in monoclinic double tungstates is large in comparison to other conventional laser hosts. For Yb:KGdW, the nonlinear refractive indices in the 800 - 1600 nm range were found to be $\sim 20 \times 10^{-16}$ cm^2/W and $\sim 15 \times 10^{-16}$ cm^2/W for $\text{E}//N_m$ and $\text{E}//N_p$, respectively [MNA+03]. Hence, significant Kerr-lensing effect and self-phase modulation can be expected.

The soliton propagation is a remarkably stable physical phenomenon. Compared to propagation in a homogeneous medium, the discrete structure of solid-state lasers results in a variation of pulse properties within a round trip but still enables soliton formation. In this case a stationary solution means that the pulse properties are restored after a round trip (aside from a

phase shift) and the mode-locked regime is often identified as *soliton-like mode-locking*, referring to the discrete nature of the diverse shaping elements .

Nevertheless, a starting and stabilizing element is necessary as solitons are not stable without saturable absorber in a laser resonator. Effectively, it has been shown that the background noise called continuum in soliton perturbation theory typically exhibits a higher gain than the soliton [Kel04]. Ultimately, the continuum getting more significant would prevent soliton propagation. Therefore, an additional mechanism is required to initiate and stabilize the soliton. This can be achieved with saturable absorption modulation based on the ultrafast relaxation of semiconductor devices.

6.4 Saturable absorbers

Saturable absorber based on semiconductors are devices that allow the accurate control of diverse parameters that are essential for stable mode-locked operation of solid-state lasers with long upper state lifetimes. Typically a semiconductor saturable mirror (SAM) designed for operation in the 1 μm spectral range is composed of two principal elements, a Bragg reflector composed of multiple AlAs/GaAs quarterwave layer pairs that provide a high reflection coefficient, and a saturable absorber typically composed of one or multiple InGaAs quantum wells embedded in a GaAs layer, Fig 6.9(a).

The saturation of the absorption of a semiconductor saturable absorber results from the accumulation of carriers in the conduction band, so that initial states for the absorbing transition are depleted while final states are occupied [PK03]. Consequently, if a saturable absorber is integrated into a mirror structure, one obtains a structure that reflects more light for more intense incoming light, so that pulse operation regime perceives less absorption than the CW regime and is ultimately favored.

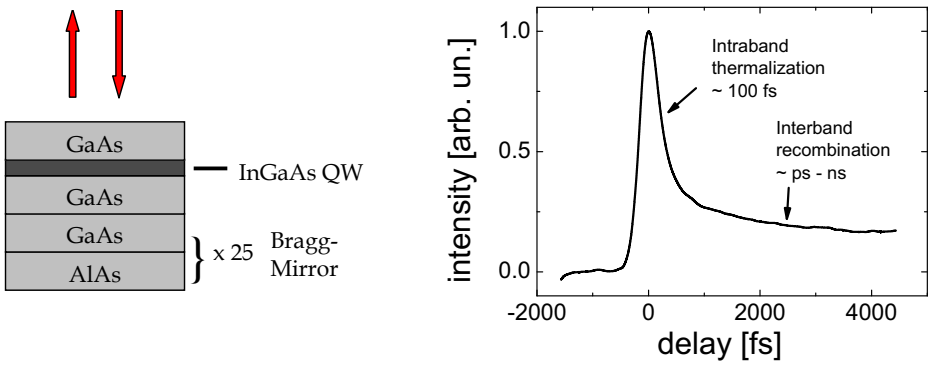

(a) (b)

Figure 6.9: (a) Schematic structure of a saturable absorber mirror. (b) Typical impulse response for a semiconductor saturable absorber.

The recovery of semiconductors absorber typically shows a bitemporal response (Fig. 6.9(b)) with a fast component (50-100 fs) related to the intraband carrier-carrier scattering and thermalization processes and, in a second place, slow interband trapping and recombination processes [KWK+96]. Yet, normally grown semiconductor mirrors have a carrier recombination time in

the nanosecond range, which tends to lead to Q-switching instabilities. In order to decrease this carrier recombination time, three methods were developed these last years; the use of low-temperature grown semiconductor, the implantation of ions into the quantum well layer and the use of surface quantum wells. While the first two methods rely on the creation of defects, the surface SAM relies on the acceleration of the saturable absorber relaxation by surface states without introducing internal defects [SSG+06].

In this work, two different types of SAM prepared at the Ferdinand-Braun-Institute, Germany were investigated; As-ions implanted SAM and surface SAM. Although both SAMs have very similar characteristics (saturation fluence, modulation depth, nonsaturable losses and relaxation time), the surface SAM proved to offer better results in term of pulse duration in the passive mode-locked regime with double tungstates. Thus, only the properties of the surface SAM's will be shortly described here.

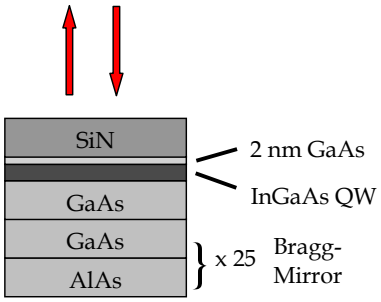

Figure 6.10: Schematic structure of the single surface quantum well saturable absorber mirror.

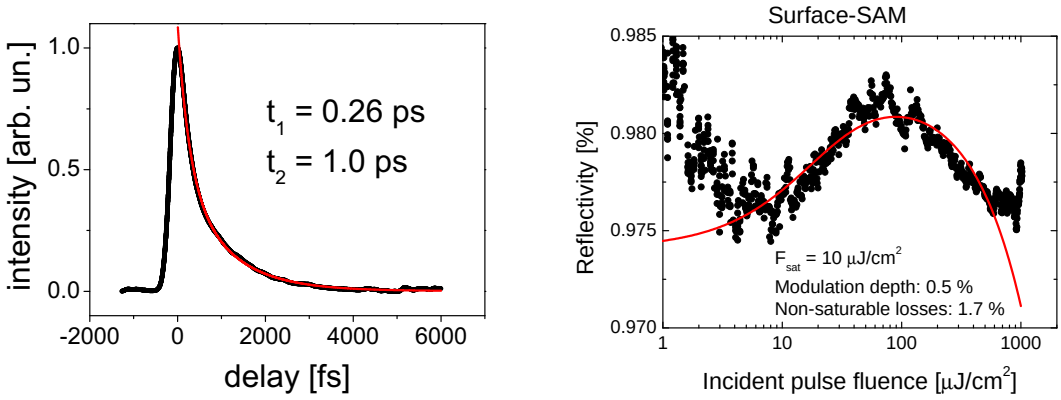

(a) (b)

Figure 6.11: (a) Pump probe trace of the single surface-QW SAM (excitation wavelength: 1060 nm) showing the measured data (black) and the double exponential fit (red) $y=y_0+A_1e^{-x/t_1}+A_2e^{-x/t_2}$. (b) Saturation fluence measurement with <200 fs pulses at 1060 nm. Measurements done by the group of G. Steinmeyer at the MBI.

The SAMs were grown on a 2" GaAs substrate by metal-organic vapor phase epitaxy (MOVPE). The structure consists of a Bragg mirror comprising 25-AlAs/GaAs quarter-wave layer pairs. The high reflectivity band of the Bragg mirror with R > 99 % extends from 990 to 1080 nm. The absorbing part is a single InGaAs quantum well which is embedded in a GaAs layers. The top GaAs layer has a thickness of only 2 nm, Fig. 6.10. An additional SiN layer of 108 nm is added by plasma enhanced chemical vapor deposition which acts as an antireflection coating, and a roughly 200 K lower growth temperature is chosen to accelerate the interband relaxation. The relaxation time as well as the nonlinear absorption was measured by G. Steinmeyer at the Max-Born-Institute. The relaxation time was measured by the pump-probe technique and indicates a very fast interband relaxation of 1 ps and an intraband relaxation time of $\sim$ 260 fs (Fig. 6.11(a)). The modulation depth amounted to $\sim$0.5%, the non-saturable losses to 1.7 % and the saturation fluence was 10 μJ/cm^2 (Fig. 6.11(b)). The significant drop of the reflectivity that can be noticed for an incident pulse fluence larger than 100 μJ/cm^2 is attributed to two photon absorption processes [TKJ+99].

6.5 Instabilities in the mode-locked operation

Two types of instabilities are here to be considered; Q-switching mode-locking and multiple-pulsing operation. Q-switching mode-locking designates a regime of operation where the mode-locked pulse train is modulated by the long time constant Q-switched envelope. As a result, variable and uncontrollable pulse energy is observed. Under the assumptions that the saturable absorber is fully saturated, that the nonsaturable losses R_{ns} are negligible in comparison with the transmission of the output coupler T_{OC} and that the laser operates far above threshold, a general stability condition in the picosecond mode-locking regime can be expressed as

$$E_p^2 > E_{sat,g} E_{sat,a} \Delta R \tag{6.25}$$

where E_p is the intracavity pulse energy, $E_{sat,g}$ is the saturation energy of the gain medium, $E_{sat,a}$ is the saturation energy of the saturable absorber, and ΔR is the modulation depth of the absorber [HPMG+99]. The saturation energy of the gain is defined as the saturation fluence at the laser wavelength multiplied by the mode area inside the gain medium as in equation 3.1. Similarly, the saturation energy of the saturable absorber is defined as the product of the absorber saturation fluence $F_{sat,a}$ and the mode area on the saturable absorber A_a.

In the femtosecond mode-locking regime when soliton effects and gain filtering are significant, substantially higher stability towards Q-switching instabilities in the mode-locking regime has been observed. The left-hand side of the above expression can be further modified with an additional term taking into account gain filtering and spectral broadening effects [HPMG+99] while the right-hand side of the expression remains yet unchanged. In any case, the stability criterion for Q-switching mode-locking depends directly on three terms that have to be minimized if possible; the saturation energy of the gain medium $E_{sat,g}$, the saturation energy of the saturable absorber $E_{sat,a}$ and the modulation depth ΔR.

Unfortunately, a strong focusing on the saturable absorber leading to a low value of the saturation energy of the saturable absorber can lead to other instabilities, i.e. multiple pulsing operation. Effectively, a strongly saturated absorber cannot provide enough stabilization mechanism and the single pulse circulating in the laser cavity may thus break up into several pulses [KAdAK98]. As a result, the pulses have a reduced energy with a generally unstable pulse spacing.

Design considerations for stable mode-locked operation

As we saw in the last sections, many variables are involved in the pulse shaping and stabilization mechanisms in the mode-locking regime. In order to clarify the principal dependences, let us examine a few important design parameters that have to be taken in consideration when passive mode-locking experiments with a saturable absorber mirror are concerned.

- **Saturable absorber parameters:** In general, a small modulation depth ΔR is desirable as it roughly scales with the non saturable losses. These latter are undesired losses and only deteriorate the laser performance. Moreover, a small modulation depth denotes a reduced tendency for Q-switching mode-locking. On the other side, a small modulation depth is also related to a weaker self-starting tendency and to some extent to longer pulses. The other main parameter, the absorber saturation energy: $E_{sat,a} = A_a F_{sat,a}$, can be easily adjusted by control of the focusing on the SAM. While a weak focusing leads to a high value of the absorber saturation energy and thus to Q-switching mode-locking, a very tight focusing can lead to multiple pulse operation or even eventually to the damage of the saturable absorber.
- **Gain medium:** This part has already been discussed in section 3.3.2. Gain media with high emission cross section are desired to prevent Q-switching mode-locking but unfortunately, such characteristic is habitually related to a narrow gain bandwidth indicating restricted possibilities for ultrashort pulse generation.
- **Laser cavity and pump source:** Since the pulse energy E_p is inversely proportional to the pulse repetition rate, a long resonator length L (denoting a low pulse repetition rate as $F_{rep} = c/2L$) helps to prevent Q-switching instabilities. Some applications in data transmission for example require very high repetition rates up to 10 GHz. For such special applications, the use of extremely small resonator is needed and the suppression of instabilities becomes particularly critical. However, for most applications, a repetition rate around 100 MHz corresponding to a resonator length of $\sim$1.5 m is satisfactory and coincides with a larger stability range.
  The laser mode area inside the gain medium A can also be modified to reach stable mode-locking operation. It is seen that a small laser mode area is expected to prevent Q-switching instabilities. Moreover, we have also seen that it corresponds to a lower laser threshold. Small laser mode area can be obtained by a proper design of the laser resonator. Nevertheless, the limiting parameter arises from the pump laser source. Effectively, similar pump mode area and laser mode area have to be chosen so that higher order transverse modes are not appearing. As high power laser diodes usually deliver beams with low quality, tight focusing of the pump beam is inevitably related to a high divergence. Thus, the development of highly doped thin active layers, where the divergence of the pump beam becomes uncritical, can be also particularly interesting for passive mode-locked operation. Moreover, with the addition of undoped layers, self-phase modulation and pulse shaping effects can be well managed as the overall thickness of the crystal (doped and undoped layer) can be varied as desired.

Chapter 7

Double tungstate passively mode-locked oscillators

This chapter is focused on the mode-locked laser experiments with the double tungstate crystals and the discussion of these results. Yb-doped monoclinic double tungstates are especially adapted for the development of compact and efficient oscillators in the 1-μm spectral range. When compared to other prospective gain media, they stand out as they exhibit simultaneously very high and broad transition cross sections, which can be attributed partly to the strong anisotropy of the host.

Soon after the first demonstration of CW laser operation in Yb-doped monoclinic double tungstates, passive mode-locking with this group of materials was investigated. In 2000 already, passive mode-locking was demonstrated based on Yb:KGdW with output powers on the order of 1 W [BSAdA+00]. Soon after, Kerr-lens mode-locking was investigated with KYW and pulse durations as short as 71 fs were obtained [LNM01]. Mode-locked operation was studied at the Max-Born Institute with saturable absorber mirrors based on both the Yb:KGdW and Yb:KYW compounds and pulse durations of $\sim$ 100 fs were reported [KPGE02]. Power scaling in the femosecond regime was also investigated with monoclinic double tungstates. Using Yb:KGdW, more than 5 W and 10 W of output power were reported with pulse durations of 134 and 433 fs, respectively. End-pumped by two 23-W laser diodes at 981 nm, the oscillator was operating at 45 MHz [Hol06]. In the thin disk geometry, the highest average power of 22 W was obtained with pulse durations of 240 fs, corresponding to a pulse energy of 0.9 μJ for a repetition rate of 25 MHz [BTI+02]. Furthermore, high pulse energies were achieved with a femtosecond regenerative amplifier using a thin disk of Yb:KYW that produced up to 116-μJ pulses with a duration of 250 fs at a repetition rate of 40 kHz [LBNG07]. Cavity-dumped femtosecond oscillators with 3-μJ pulse energy at 1 MHz based on a thin-disk Yb:KYW were also demonstrated [PSSM07].

As one can see in the selected results shortly listed above, ultrashort pulses and power scaling in terms of average power and pulse energy has already been successfully demonstrated with the monoclinic double-tungstates. In particular, the use of the thin disk geometry has shown promising results for ultrashort pulse generation with simple or cavity-dumped oscillators as well as in regenerative amplifiers. As described in the former chapters, such thin-disk concept requires the implementation of very thin active layer and composite structures can ef-

ficiently contribute to ensure the thermo-mechanical stability of such elements. More generally, composite structures are advantageous for mode-locking operation as superior thermal management is possible. In this way, higher inversion in the active layer is maintained and the generation of shorter pulse durations is supported. As already mentioned, the use of structures where active layer and substrate consist of the same crystal host can provide some advantages compared to heterocomposite structures like bonded crystals of Yb:YAG on sapphire [BBST00]. Effectively, they could reduce the problem of parasitic reflections and birefringence effects, which could alter the mode-locked operation [KFB+92].

The present chapter deals with passive mode-locked experiments with both Yb:KLuW and Yb.KYW, two crystals that are especially adapted for the development of composite structures. At first, passive mode-locking based on bulk Yb:KLuW crystals is investigated (section 7.2.1) and, in a second time, based on an epitaxial Yb:KLuW structure (section 7.2.2). Follows femtosecond operation with the newly developed structures based on the KYW compound, i.e. the segmented grown Yb:KYW/KYW crystal in section 7.2.3 and the diffusion bonded Yb:KYW/KYW (section 7.2.4). In the second part of this chapter, the first laser operation in the femtosecond regime of the disordered Yb:NaYW crystal is presented (section 7.3.1). Finally, a short sum up as well as a discussion and comparison with results achieved by other research groups is presented (section 7.4)

7.1 Experimental setup

Laser resonator

The laser resonator used for CW investigation shown in figure 5.3 has to be modified to allow passive mode-locking. For dispersion compensation, two SF10 prisms were inserted in the cavity arm containing the output coupler with different tip-to-tip separation and prism insertion into the beam depending on the crystal investigated. In the other arm, an additional focusing mirror M4 (RC= -10 or -15 cm) was added in order to increase and control the pulse fluence on the semiconductor saturable absorber mirror, see Fig 7.1.

The same three pump laser sources as described previously were used 5.2. The laser resonator was usually aligned to obtain the shortest pulse. Additionally, for the majority of the crystals investigated, the stability range both in terms of input-output power and spectral tunability was examined. As is has been detailed in section 6.2, the prism pair creates a spatial chirp, i. e. a wavelength dependent position of all spectral components of the beam. Thus, an optical filter is obtained by conscientious insertion of a knife edge between the second prism and the output coupler so that tunability in the mode-locked regime can be studied.

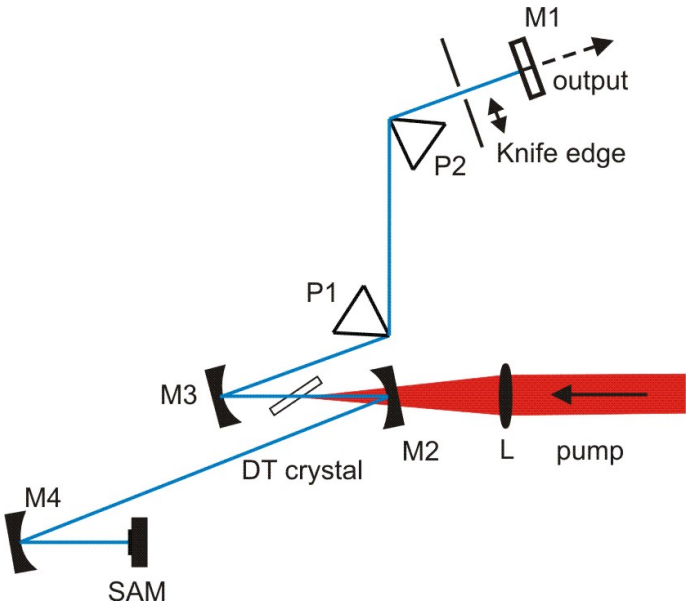

Figure 7.1: Setup of the resonator selected for passive mode-locking: SAM - saturable absorber mirror. M1 - output couplers, M2, M3 - folding mirrors, M4 - focusing mirror, L - f=6.28 cm focusing lens.

Autocorrelator

The pulse duration was measured with a conventional intensity autocorrelator and stable single pulse operation was confirmed by monitoring the pulse train on an oscilloscope with a fast photodiode as well as by the control of the autocorrelation trace on the large range of the autocorrelator (150 ps). Eventually, the optical spectrum was also examined with a spectrum analyzer.

The intensity autocorrelation is a standard method to characterize an ultrashort pulse. In a background free intensity autocorrelator as shown in figure 7.2, the input pulse is split into two arms of an interferometer, and one of the pulse is delay by τ. The two pulses are spatially overlapped in some instantaneous responding nonlinear optical medium such as a second-harmonic-generation (SHG) crystal.

Due to momentum conservation, one may suppress a possible background coming from the simple SHG of the individual pulses alone with an iris diaphragm and keep the only signal related to the product:

$$E_{SHG} \propto E(t)E(t-\tau). \tag{7.1}$$

This field has an intensity that is proportional to the product of the intensities of the two pulses given by

$$I_{SHG} \propto I(t)I(t-\tau). \tag{7.2}$$

This optical signal is finally detected by a photo detector, which integrates the signal because its response is much slower than the pulse width so that finally, the intensity autocorrelation I_{ac}, defined as

$$I_{ac} = \int_{-\infty}^{\infty} I(t)I(t-\tau)dt \tag{7.3}$$

is measured.

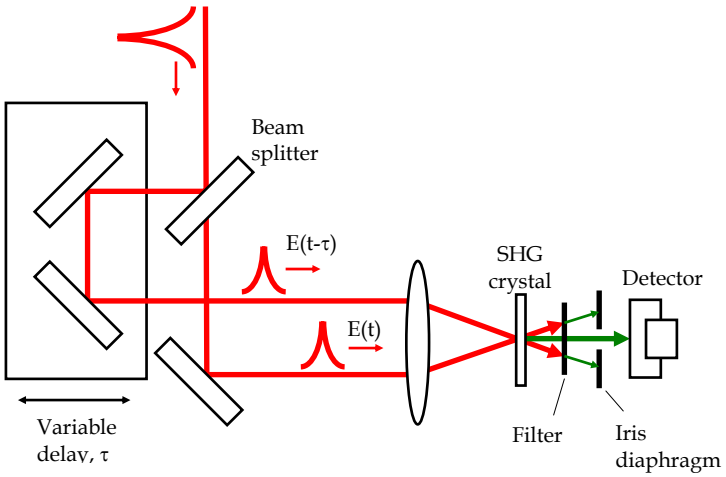

Figure 7.2: Layout of a background-free intensity autocorrelator using second-harmonic generation.

Note that the intensity autocorrelation is symmetric by construction $I_{ac}(\tau) = I_{ac}(-\tau)$ and that it does not contain full information about the electric field of the pulse since the phase of the pulse in the time domain is completely lost. Thus a pulse intensity shape and phase must typically be assumed when using autocorrelation measurement. Fitting the recorded autocorrelation with a theoretical curve for that assumed pulse shape gives an primary check. For sech^2-shaped pulses, the width of the autocorrelation signal is 1.54 times the width of the pulse duration.

7.2 Monoclinic double tungstate mode-locked oscillators

7.2.1 Bulk Yb:KLu$(WO_4)_2$ oscillator

As already mentioned several times throughout this thesis, the monoclinic double tungstates offer very favorable spectroscopic properties for a certain crystal orientation corresponding to polarization along the N_m-crystallo-optic axis. Careful examination of the emission cross section (Fig. 3.8) reveals that the broad and rather smooth emission cross section for polarization along the N_p-crystallo-optic axis also exhibits suitable features for femtosecond pulse generation. Here, passive mode-locking based on Yb:KLuW is investigated for the first time and both polarizations are studied. In order to estimate the potential gain bandwidth for the mode-locked operation in the N_m- and N_p-orientation, the gain cross section for several realistic population

inversion rates is calculated and presented in figure 7.3. Although the gain cross section is slightly higher for the N_m-polarization, very similar spectral width can be anticipated for these two polarizations.

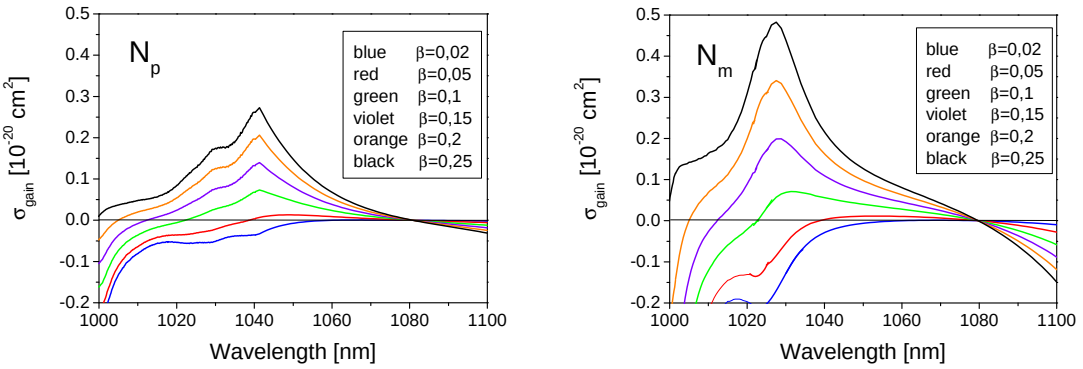

(a) (b)

Figure 7.3: Calculated gain cross section σ_{gain} (equation 2.8) for polarization along the (a) N_p- and (b) N_m-crystallo-optic axes of Yb:KLuW and different realistic population inversion rates β. The two curves are obtained from the measured transitions cross sections presented in figure 3.8.

For the mode-locked experiments a 2.8-mm thick crystal oriented for N_m-polarization and a 3-mm thick crystal oriented for N_p-polarization were prepared, both doped with 4.3×10^{20} Yb^{3+}-atoms/cm^3. In a first time, the cavity design was optimized in order to obtain the shortest pulse duration using the N_m-oriented Yb:KLuW crystal. To this aim, two SF10 Brewster prisms with a tip-to-tip separation of 38 cm were inserted in the arm containing the output coupler and a surface semiconductor saturable absorber mirror SAM was selected.

Stable mode-locked operation was obtained at a pulse repetition rate of 95 MHz. The deconvolved FWHM of the shortest pulse duration was 81 fs with an average power of 70 mW for 3% OC transmission. The corresponding output spectrum was centered at 1046 nm and had a bandwidth of 14.3 nm. This results in a time-bandwidth product of 0.318 corresponding to nearly transform-limited $sech^2$-pulses. The obtained pulse duration for a SAM mode-locked Yb-doped tungstate laser is substantially shorter than the 100 fs limit reported for Yb:KGdW and Yb:KYW [PHS04, KPGE02]. The intensity autocorrelation trace together with the corresponding fit and the spectrum of the shortest pulses are shown in Fig. 7.4(a).

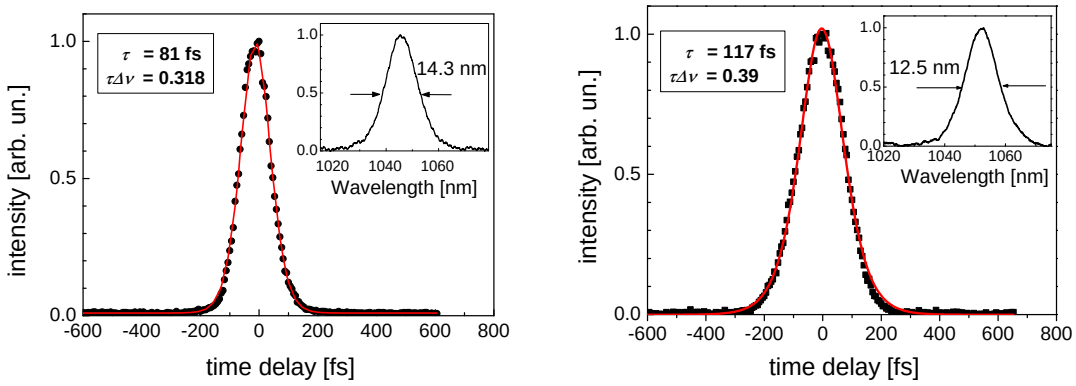

Figure 7.4: Autocorrelation traces and spectra (insets): (a) N_m-oriented, Ti:sapphire-pumped; (b) N_p-oriented, TDL-pumped.

Femtosecond operation was then investigated with the N_p-oriented Yb:KLuW crystal. The results achieved for polarization parallel to the N_m- and N_p-axes with the same resonator configuration, but with slightly different dispersion compensation, are compared in Fig. 7.5. Only minor differences could be detected, contrary to the prediction of [LNM01] where potentially shorter generated pulses for crystal orientations along the N_p-direction due to the broader spectrum of the emission cross section was anticipated. As indicated by the calculated gain cross sections in figure 7.3, the achievable bandwidth at the same population inversion rate is nearly identical for both orientations and from the experimental results in the different operation regimes similar population inversions can be deduced. For both crystal orientations mode-locking was achieved with output coupler transmissions T_{OC} between 1% and 5%. The shortest pulse duration for the N_p-oriented crystal was 83 fs (FWHM) with an output power of 36 mW at 1049 nm using an 1% OC. A much higher average power of 295 mW could be generated for a pulse duration of 100 fs (Fig. 7.5).

Using the TDL as a pump source, only the N_p-oriented crystal was investigated. By inserting the prisms into the cavity, stable mode-locking was achieved for T_{OC} between 1% and 3%. A 1-W pump power incident on the crystal resulted in a maximum mode-locked output power of 56 mW with a 3% OC. The lower efficiency compared to the experiments with Ti:sapphire laser pumping is caused by the imperfect match of the pump and resonator modes and the lower beam quality of the diode emission. At a pulse repetition frequency of 95 MHz a pulse duration of 117 fs (FWHM) was achieved, as shown in Fig. 7.4(b). The corresponding spectrum, centered at 1053 nm, had a spectral bandwidth of 12.5 nm, which yields a time-bandwidth product of 0.39, such that the pulses are almost transform-limited.

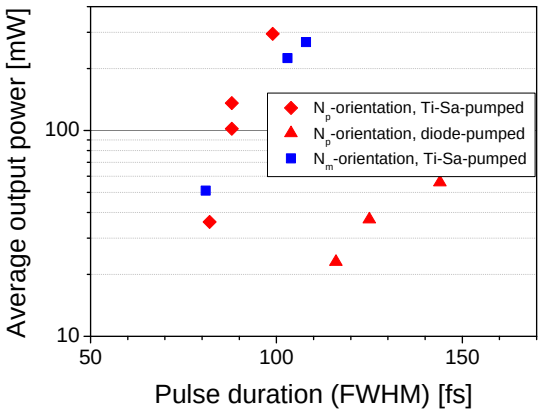

Figure 7.5: Comparison of the Yb:KLuW femtosecond laser performance (average power vs. pulse duration) for polarization oriented parallel to the N_p- and N_m-crystallo-optic axes.

7.2.2 Epitaxial Yb:KLu$(WO_4)_2$ /KLu$(WO_4)_2$ oscillator

The 100 μm-thick 10 at.%-doped epitaxial Yb:KLuW crystal described in section 5.3.1 was investigated in the mode-locked regime. The epitaxial crystal was orientated for polarization parallel to the N_m-crystallo-optic axis. The femtosecond mode-locked regime was realized by inserting two SF10 Brewster prisms with a tip-to-tip separation of 31 cm into the arm containing a 1% output coupler. In the other arm of the resonator, a surface SAM was selected. Stable mode-locking was achieved and the measured autocorrelation traces are well fitted assuming a sech^2-pulse shape. Pulses as short as 114 fs (Fig. 7.7) at a central wavelength of 1030 nm could be achieved. This corresponds to average output power of 31 mW for an absorbed pump power of 725 mW and the cavity round trip time was 101 MHz. The time-bandwidth-product of 0.43 is slightly above the Fourier limit (inset fig. 7.7). The lower limit for the pulse duration and the observed deviation from the transform-limited pulse performance can be related to the reflection characteristics of the folding mirrors which are restricted by the close separation between the pump and lasing wavelengths. The output power could be increased using a 3% output coupler and 94 mW were obtained, again at 1030 nm, for an absorbed power of 785 mW. The generated pulses had a FWHM of 200 fs in this case and were almost bandwidth-limited (time-bandwidth product: 0.32).

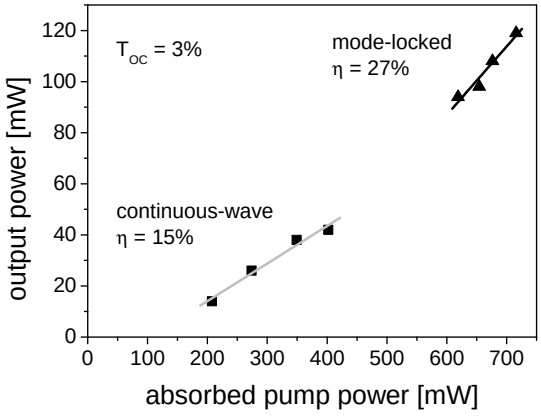

Figure 7.6: Output power versus absorbed pump power above and below the mode-locking threshold (CW); η: slope efficiency

The output power versus the absorbed pump power below and above the mode-locking threshold is shown in Fig. 7.6. Mode-locked operation was obtained with a maximum output power of 119 mW applying a 3% transmission output coupler. From these experimental data the measured slope efficiency amounted to 27% and the pump efficiency reached 17%. The slight increase in the slope efficiency by the transition from the CW to the mode-locked regime is due to the saturated loss of the SAM.

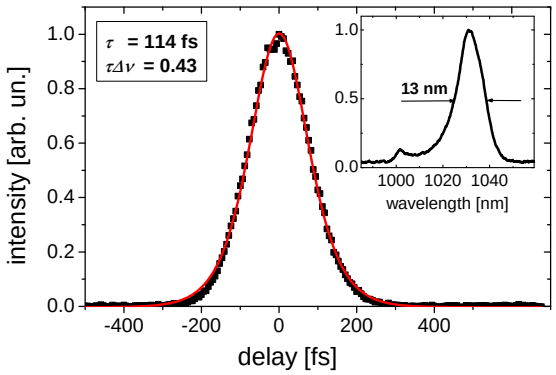

Figure 7.7: Autocorrelation and spectrum (inset) in the femtosecond regime of the epitaxial composite 100-μm-thin Yb(10%):KLuW layer on a 1.1-mm thick KLuW substrate.

In order to illustrate that the 114 fs pulse duration is not the limit, one can compare the femtosecond performance of the epitaxial Yb:KLuW with that of the bulk Yb(5%):KLuW (2.8-mm thick) single crystal (Section 7.2.1, Fig. 7.4(a)) achieved under the same experimental conditions - polarization also oriented parallel to N_m. A larger gain bandwidth is expected for the epitaxial structure, which is attributed to the reduced reabsorption leading to a higher population inversion level β. The last point can be clearly observed in Fig. 7.3, visualizing the estimated

gain bandwidth for different population inversion levels. From the generated spectrum of the bulk Yb:KLuW (inset Fig. 7.4) with a center wavelength of 1045 nm, it can be deduced that the gain cross section corresponds to a population inversion β of $\approx$0.08. The pulse spectrum of the epitaxial composite is centered at 1030 nm with a broadened shape of the short wavelength wing extending below 1000 nm, meaning a fully covered gain bandwidth in this range (Fig. 1), concluding a β >0.2. This gives rise for the generation of pulses much shorter than the 81 fs obtained with Yb:KLuW bulk crystal due to the strongly reduced reabsorption, resulting in potentially broader gain bandwidths.

Neither in the emitted spectrum nor in the field distribution of the Yb:KLuW/KLuW laser, indications of modulations could be detected. For all arrangements investigated, the mode-locked operation was stable for hours, without evidence of dropping out or tendencies to passive Q-switching and remained basically TEM_{00}.

7.2.3 Segmented grown Yb:$KY(WO_4)_2$ /$KY(WO_4)_2$ oscillator

The segmented grown Yb:KYW/KYW composed of a 13 at.%-doped 200 μm-thick Yb-doped KYW segment on top of a 1.2 mm-thick undoped KYW crystal was studied in the mode-locked regime. For dispersion compensation, the two SF10 prisms with a tip-to-tip separation of 39 cm were inserted in the cavity arm containing the output coupler. In the other arm, a surface SAM with features as described earlier was chosen.

The shortest pulses obtained with the Yb:KYW/KYW laser using an output coupler of 1% had a FWHM of τ=99 fs with an average power of 69 mW at a repetition rate of 92 MHz (Fig. 7.8(a)). The corresponding output spectrum was centered at 1029 nm and had a bandwidth (FWHM) of 12.6 nm. The related time-bandwidth product was 0.353, which is close to the Fourier limit for a $sech^2$-pulse shape. The achieved pulse durations correspond to the shortest pulses for a SAM mode-locked Yb:KYW oscillator. Using Yb:KYW single crystals, shorter pulses of 71 fs were obtained only with Kerr-Lens mode-locking [LNM01] which is usually not self-starting and requires critical alignment. For SAM mode-locked lasers, previous work reported pulse durations of 101 fs with bulk KYW [KPGE02] and sub-100 fs pulses (τ=81 fs) were achieved with Yb:KLuW single crystals as reported in section 7.2.1 [GRP$^+$05]. Composite crystals were also investigated for short pulse generation. In particular, pulse durations of 114 fs were obtained with a 100 μm thick, 12 at. % epitaxial Yb:KLuW/KLuW laser, see section 7.2.2 [RPG$^+$05]. Diode-pumped hetero-composite structures based on the uniaxial Yb:SYS/YAG produced 100 fs pulses for an average power of 70 mW [DCB$^+$05].

The slope efficiency with respect to the input power was investigated with an alignment approximately giving the shortest pulses, Fig. 7.8(b). CW operation was obtained for incident pump powers below 680 mW. Above this level, the laser switched to the mode-locked regime. Additional CW peaks were observed in the spectrum near the mode-locking threshold but then, when increasing the input power, mode-locked operation was stable and no tendencies for Q-switching were observed.

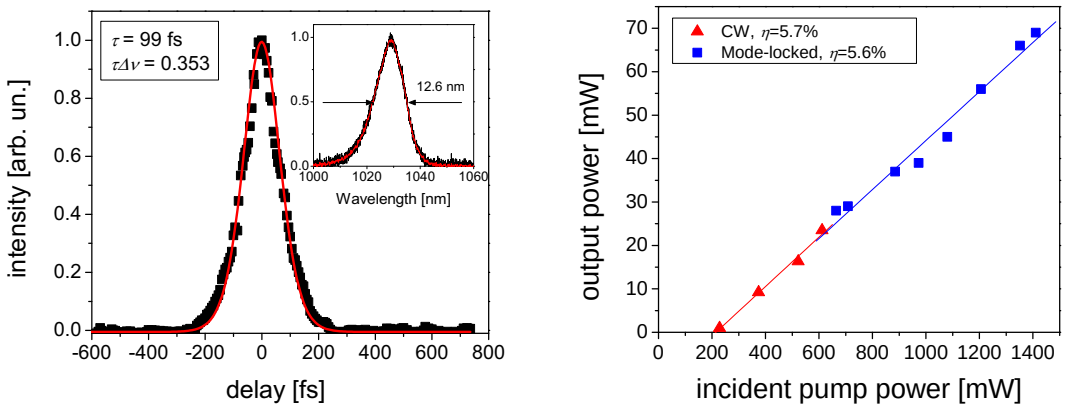

(a) (b)

Figure 7.8: (a) Autocorrelation trace and spectrum (inset) of the shortest pulses obtained with the Yb:KYW/KYW laser and, (b) output power of the laser below and above the mode-locking threshold versus incident pump power.

In general, pulses tended to shorter durations when the incident power was increased reaching an optimum around 1.4 W. The slope efficiencies in the CW and mode-locked regimes calculated with respect to the incident pump power were comparable, Fig. 7.8(b). Changing to output coupling of 3%, the average output power increased to 164 mW but the pulse durations increased, τ=130 fs.

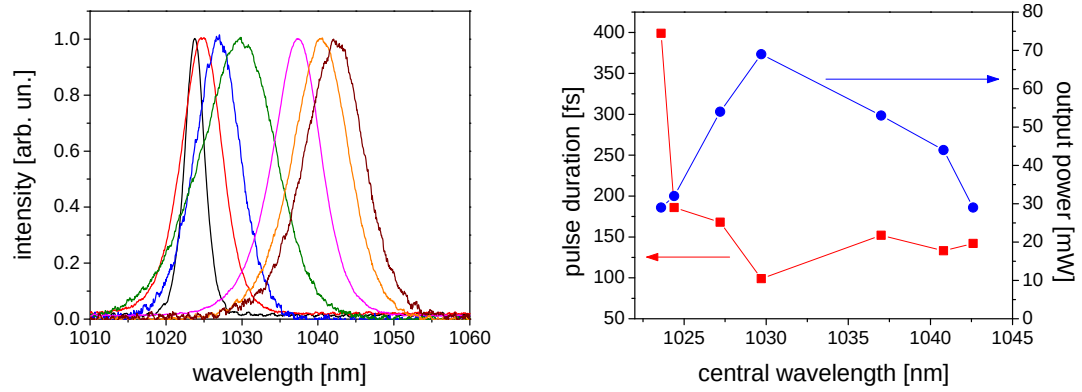

(a) (b)

Figure 7.9: (a) Tunability of the Yb:KYW/KYW laser in the mode-locked regime with T_{OC}=1%, and (b) the corresponding pulse durations and average output powers for different central wavelengths.

The spectral tunability in the mode-locked regime was investigated using a slit placed between the second prism and the output coupler. Stable mode-locking was achieved for central wavelengths from 1023 to 1043 nm, Fig. 7.9. Sub-200 fs pulses were obtained for almost the entire tuning range, from 1024 nm to 1043 nm.

7.2.4 Diffusion bonded Yb:$KY(WO_4)_2$ /$KY(WO_4)_2$ oscillator

Passive mode locked regime was investigated with the 5 at.% Yb-doped KYW/KYW diffusion bonded crystal. It was realized by placing a surface SAM at one end of the resonator and the two SF10 Brewster prisms with a tip-to-tip separation of 37 cm for intracavity optimization of the group-velocity dispersion into the other arm. The shortest pulses were achieved with a 5 % output coupler and the resulting pulse repetition frequency amounted to 93 MHz. In figure 7.10 the measured autocorrelation trace and the fit assuming a $sech^2$-pulse shape is shown together with the emission spectrum centered at 1029 nm (inset). 66 fs pulses were generated with an average output power of 182 mW for an input pump power of 1.3 W. Using T_{OC}=10 % the output power could be increased to 264 mW with only somewhat longer pulse durations of 69 fs. The time-bandwidth-product of 0.43 is above the Fourier-limit, indicating the potential for further chirp compensation. An additional extracavity compression was implemented to shorten the pulses. A sequence of two SF10 prism pairs separated by 32 cm each was used. After passing the external compressor, pulses as short as 62 fs were achieved without noteworthy power loss. The autocorrelation trace of the shortest pulses together with the corresponding fit is shown in Fig. 3b. With the preserved spectral bandwidth of 23 nm (FWHM), the calculated time-bandwidth product of 0.40 was still slightly above the Fourier limit (0.314). The achieved pulse durations in this work are, the shortest for mode-locked Yb-doped monoclinic double tungstate lasers and any Yb laser based on a composite crystal. The 71 fs once obtained with a Kerr-lens mode-locked Yb:KYW laser was the shortest pulse duration reported so far [LNM01]. The short pulse spectral tunability was also examined for the diffusion-bonded Yb:KYW/KYW oscillator by means of the intracavity prisms, applying T_{OC}=3%. Sub-90 fs pulse durations were obtained for a tuning range from 1027 to 1034 nm. The average output power was between 80 and 92 mW for an input power of 1.3 W. Neither in the emitted spectrum nor in the field distribution of the Yb:KYW/KYW laser we were able to detect any indications of modulations.

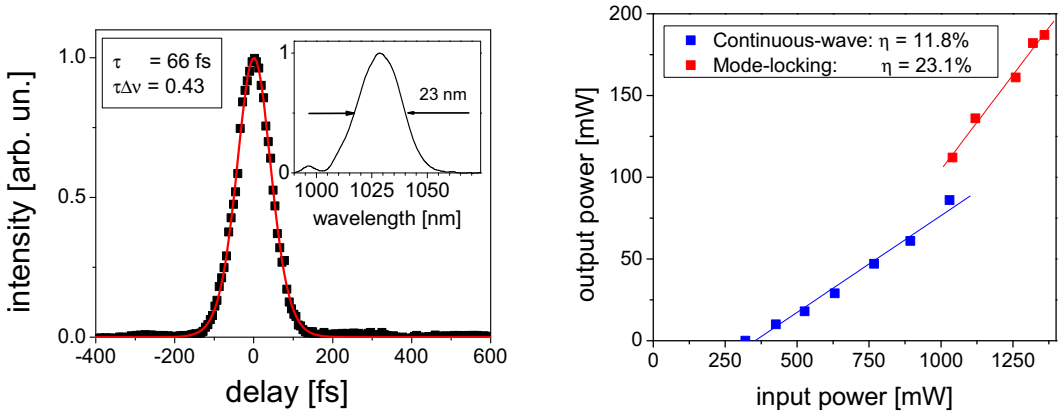

(a) (b)

Figure 7.10: (a) Autocorrelation traces and spectra (insets) of the shortest pulses under Ti:sapphire laser pumping and (b) stability range of the passively mode-locked diffusion bonded Yb:KYW/KYW oscillator.

Implementing the broad-stripe diode laser as a pump source, pulses as short as 66 fs were achieved, the same as using Ti:sapphire laser pumping but with an improved pulse quality. The corresponding output spectrum was centered at 1038 nm and had a bandwidth of 19 nm. This results in a time-bandwidth product of 0.35 corresponding to nearly transform-limited $sech^2$-pulses (Fig. 2b). The laser operated at a repetition rate of 90 MHz and 1% output coupler transmission was used. The measured average output power was 22 mW for an absorbed pump power of 1.1 W. These results indicate that a proper selection of the diode pump parameters and careful alignment allow similar mode-locked laser performance with Ti:sapphire- or diode-laser pumping.

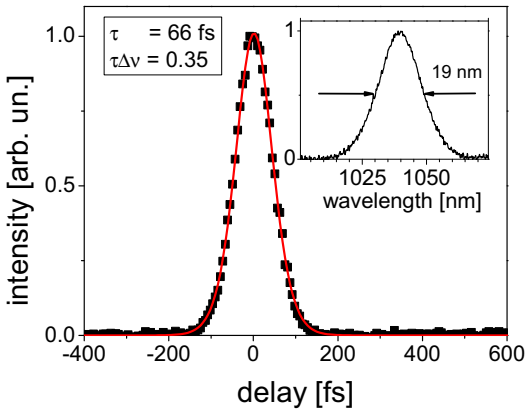

Figure 7.11: Autocorrelation traces and spectra (insets) of the shortest pulses obtained from the diffusion-bonded Yb:KYW/KYW oscillator under diode laser pumping

7.3 Tetragonal Double Tungstates

Several different disordered double tungstates and molybdates have been studied in the mode-locking regime throughout this work. In particular, sub-100 fs have been achieved for the three tetragonal double tungstates Yb:NaGdW [CSEB+06], Yb:NaYW [GCTS+07] and Yb:NaLuW [GCH+07]. See Fig. 7.14 for a recapitulation of all Yb-doped oscillators leading to sub-100 fs pulses. However, only the most interesting and promising results obtained with Yb:NaYW are described here.

7.3.1 Yb:NaY$(WO_4)_2$ oscillator

The broad tunability achieved with Yb:NaYW in CW operation is promising to generate femtosecond pulses. In order to better estimate the potential gain bandwidth for the mode-locked operation for both π- and σ-polarization, the gain cross section for several realistic population inversion rates can be calculated, see Fig. 7.12. As it can be seen, the gain bandwidth is very similar for both polarizations, however, the higher gain for the π-polarization indicates a more

efficient laser operation in terms of output power. This has been confirmed by experiment in the CW regime, see section 5.4.

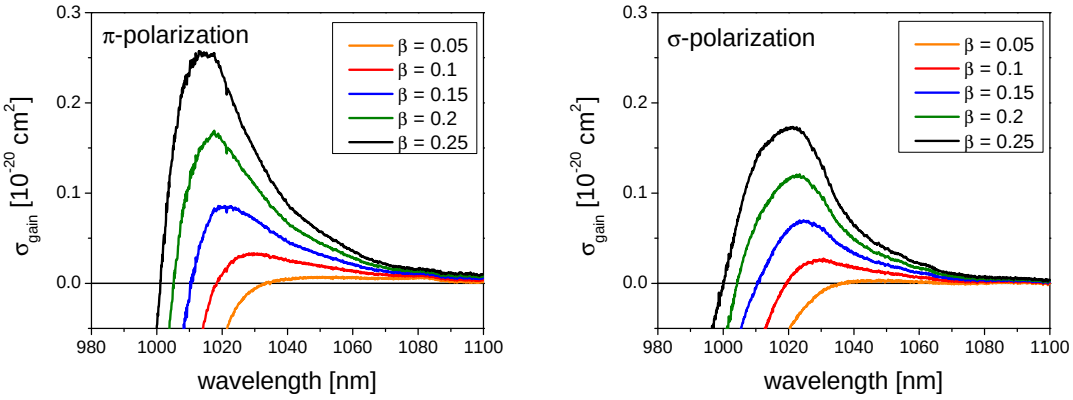

(a) (b)

Figure 7.12: Calculated gain cross section σ_{gain} (equation 2.8) for (a) π- and (b) σ-polarizations of Yb:NaYW and different realistic population inversion rates β. The two curves are obtained from the measured transitions cross sections presented in figure 3.14.

Thus, the a-cut, 1.51 mm-thick Yb:NaYW plate, was oriented for the π-polarization (E//c). The arm with the output coupler of transmission T_{OC}=1% contained two SF10 Brewster prisms separated by 37 cm. The cavity length corresponded to a repetition rate of 96 MHz. With intracavity optimization of the group-velocity dispersion, pulse durations as short as 67 fs ($sech^2$-pulse shape) were obtained. Yet shorter pulses were achieved by additional extracavity compression.

For this purpose, an analogous SF10 prism pair was first used to compensate the spatial offset of the spectral components and a third SF10 prism pair (separation of 29 cm) was used in a double pass for additional compression. The autocorrelation trace of the shortest pulse duration of 53 fs is shown in figure 7.13 together with the corresponding spectrum (inset). The time-bandwidth product (0.513) was still above the Fourier limit (0.314). The output power was 91 mW. These are one of the shortest pulses from Yb lasers: Sub-60 fs pulses were obtained up to now only with phosphate glass [HMGM+98], $LuVO_4$ [RML+06], CALGO [ZDB+06] and LSB [RSK07] as hosts.

The spectral tunability in the mode-locked regime was also investigated using a knife edge placed between the second prism and the output coupler. Stable mode-locking with sub-200fs pulses was achieved for central wavelengths between 1018 to 1040 nm.

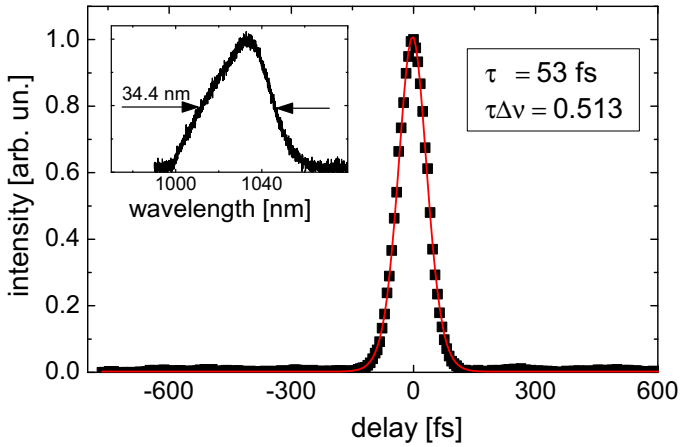

Figure 7.13: Autocorrelation trace and spectrum (inset) of the mode-locked Yb:NaYW laser

7.4 Comparison and summary of the mode-locked laser results

As we just saw, many very promising results have been achieved with bulk monoclinic and tetragonal double tungstates as well as with new composite structures based on the monoclinic double tungstates. The results presented here can be compared with other results achieved by other groups, or throughout this project but based on other Yb-doped gain media. For this comparison, it is convenient to plot the pulse duration versus the average output power for all Yb-oscillators generating sub-100 fs pulses, see Fig. 7.14. As one can see, the double tungstates and their composite structures corresponds to 8 of the 18 crystal variations that have lead to sub-100 fs pulses. This immediately demonstrates the excellence of the double tungstates for femtosecond generation. It should also be noted that the results achieved with the segmented growth and diffusion bonded crystals represent the first oscillators based on composite structures that generate sub-100 fs pulses. In these two cases, it is especially important to observe that no modulation is detected in the emitted spectra or in the field distribution so that composite crystals offer only advantages for efficient ultrashort pulse generation as they allow efficient heat removal.

Throughout this work, some of the shortest pulse durations ever generated from Yb-doped gain media have been achieved. Actually, at the moment, the shortest pulse has been obtained based on Yb:CALGO with external compression with a duration of 47 fs, but a CW component was present. Without CW component, the pulse duration was longer with a value of 57 fs [ZDB+06]. Thus, the 53 fs and the 66 fs pulse durations that have been achieved with Yb:NaYW and the diffusion bonded Yb:KYW/KYW, respectively, are among the shortest ever obtained based on Yb-doped gain media. Although some results have been achieved only with Ti:sapphre laser pumping, the similar results in terms of pulse duration achieved directly from the oscillator in the case of the diffusion bonded crystal with both Ti:sapphire laser- and diode-pumping indicate that proper optimization of the diode laser and the cavity permit to achieve comparable mode-locked laser performance.

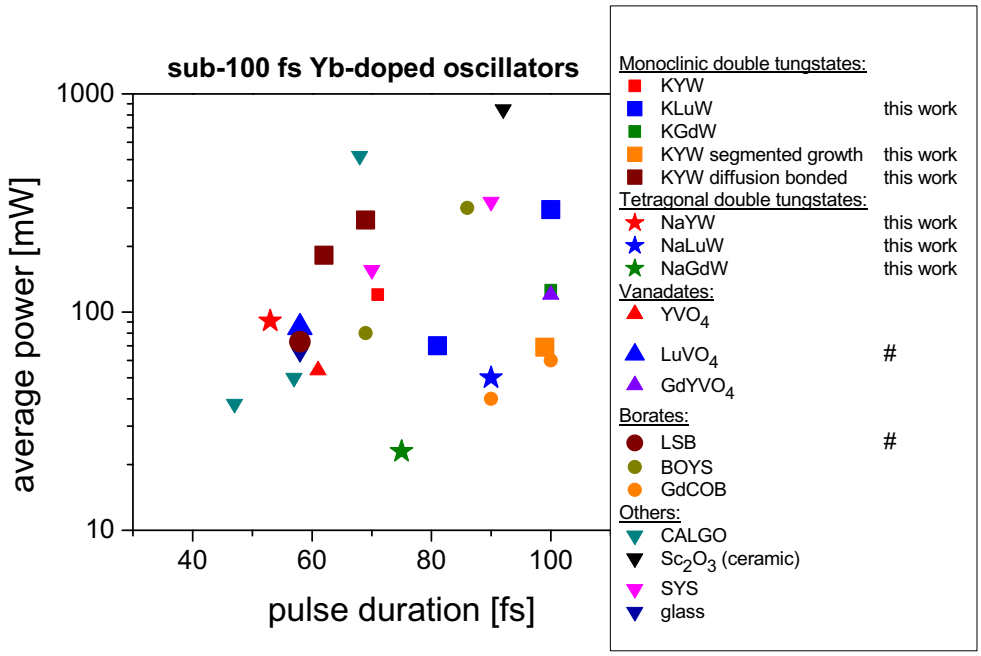

Figure 7.14: Comparison of sub-100 fs Yb-oscillators. The average output power versus pulse duration is plotted for all Yb-doped oscillators that have generated sub-100fs pulses. (#) indicates additional research results that I have obtained parallel to this work.

It is also interesting to note that out of the 18 different experiments presented in figure 7.14, only two of them rely on Kerr-lens mode-locking. This well reflects the flexibility and reliability of the mode-locked operation with slow saturable absorbers. In the case of the experiments presented in this thesis, the choice of a specific gain medium with a suitable SAM permitted to achieve large stability ranges in term of average output power and tunability. Consequently, this demonstrates that inherent problems such as Q-switching instabilities in mode-locking or double pulsing can be well neutralized with double tungstate crystals.

Finally, it is worth to mention that the time-bandwidth product was still above the Fourier limit even after external compression, signaling uncompensated chirp, for several experiments in which very short pulse durations were achieved. A reasonable explanation is the large amount of third order dispersion that is introduced by the SF10 prism pair. The influence of the higher order dispersion in passively mode-locked solid-state lasers has been treated theoretically [HMN93, HKM97]. These models demonstrate the formation of resonant spectral sidebands due to higher order dispersion. In particular, third-order dispersion causes only one sideband to appear and its location, at the red or blue side of the principal spectrum, depends on the sign of the TOD. For the case of negative TOD as generated by the two SF10 prisms (Fig. 6.7), the resonant sideband appear at the blue side of the spectrum. This corresponds very well with these experiments where an asymmetric spectrum with a sideband at the blue side is usually observed. Let us then concisely detail a way to minimize the influence of the third order dispersion.

Minimization of the third order dispersion

It is known that, for a certain wavelength range, an careful selection of the prism material can result in intracavity group delay dispersion and third order dispersion compensation simultaneously [LB93]. The TOD of a prism pair composed of any typical optical material can be calculated by means of the Sellmeier equations and is found to be negative in the visible and to increase with increasing wavelength. If no prism insertion is assumed, the TOD dispersion crosses zero between 990 nm for silica and 1390 nm for SF10. The minimum required insertion as well as any supplementary prism insertion will further shift all curves upward so that all curves cross each other for slightly positive TOD (Fig. 7.15).

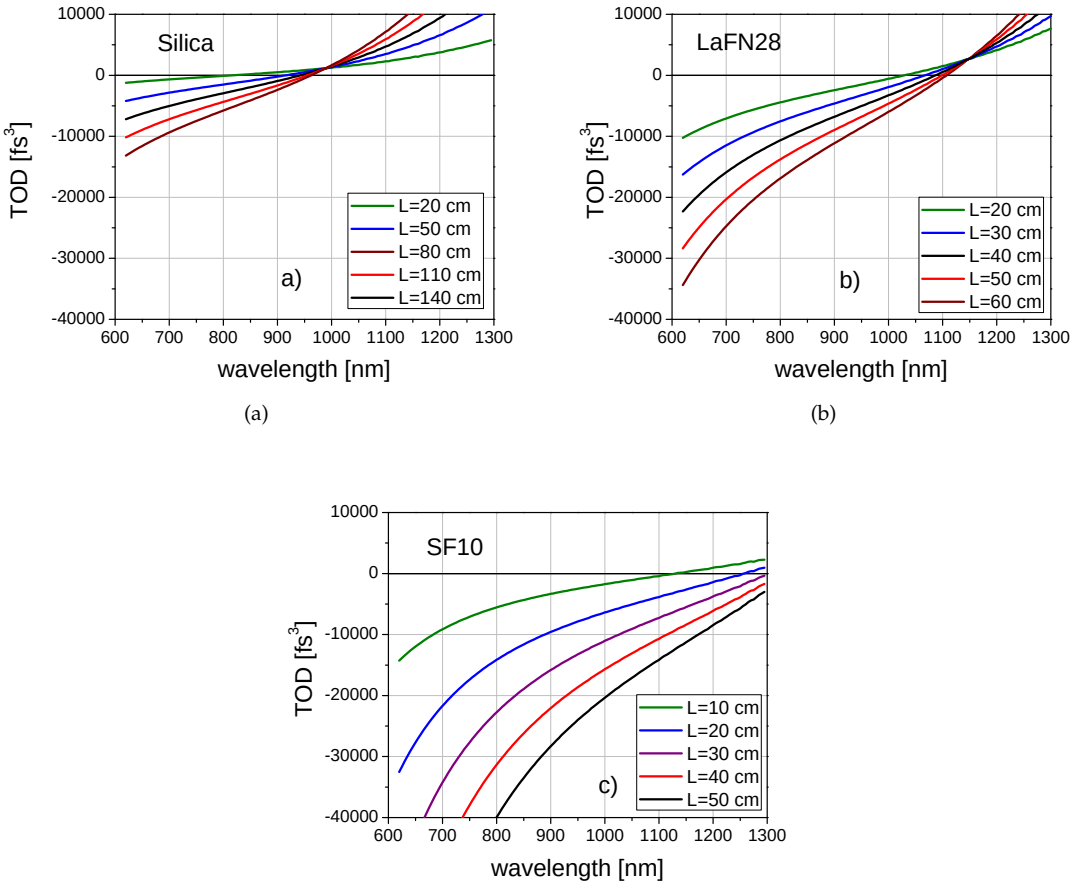

(a) (b) (c)

Figure 7.15: Third order dispersion introduced by a (a) silica, (b) LaFN28 and (c) SF10 prisms pair. The Sellmeier coefficients used to calculate these curves are given in the appendix.

As one can note from figure 7.15(a), a silica prism pair introduces positive TOD dispersion around 1040 nm for all tip-to-top separations so that compensation of the positive TOD introduced by doubles tungstates is not conceivable. Moreover, it can be shown that silica prisms

introduce only a small amount of GDD, requiring a very large tip-to-tip separation for dispersion compensation, which is not handy in a laser resonator. On the opposite, SF10 prisms (Fig. 7.15(b)) demand only a small prisms separation for GDD compensation but introduce a large amount of TOD as we have seen. Prism materials that correspond to an average situation would allow to compensate the GDD and minimize TOD. From the prism materials that are available in the market, LaFN28 seems to be an adequate solution. As shown in figure 7.15(c), the TOD is only slightly negative around 1040 nm with LaFN28 prisms, which is adequate to compensate the small positive TOD of double tungstates and a reasonable prisms separation of roughly 50 cm would generate the same amount of GDD that was necessary for all aforementioned experiments. Initial results show that sub-100 fs can be generated with these prisms. However, shorter pulse duration than what has been achieved with SF10 prisms is still not demonstrated. Mode-locked experiments with GTI mirrors, allowing a close control of the TOD, is also currently investigated and will be further studied in the future.

Chapter 8

Conclusion

In the laser physics domain, a major change is taking place over the last years, associated with the progress of Yb-doped laser materials for emission in the 1 μm spectral range that was previously covered by their Neodymium counterparts. The absorption band of the Yb ion well matches the emission spectrum of readily available high power InGaAs laser diodes developed for the telecommunication sector. Moreover, the Yb ion is ideally suited for the development of efficient laser sources as it exhibits very few spectroscopic loss processes and provides a small Stokes shift between absorption and emission. Thus, detrimental thermal effects are minimized denoting a remarkable potential for power scaling. Finally, the Yb-doped gain media can exhibit broad transition cross sections when associated with a suitable host. In this work, the double tungstate crystals, recognized as some of the most attractive Yb-doped gain media, are investigated. At first, the monoclinic potassium double tungstates KREW, which are characterized by an important anisotropy and in a second place, the tetragonal sodium double tungstates NaREW, which present a structural disorder, were studied.

Partially due to the strong anisotropy of the monoclinic tungstate compounds, one polarization (E$//N_m$) presents some remarkable features with extremely large absorption and emission cross sections together with broad linewidths. Moreover, these crystals can incorporate a large amount of Yb^{3+} (up to 100 % doping for KYW and KLuW) without significant concentration quenching as a consequence of the large separation between two active ions. The monoclinic potassium double tungstates offer thus some unique properties and are specially adapted for efficient continuous-wave operation as well as for ultrashort pulse generation. However, their strong anisotropy proscribed till recently the manufacture of composite structures. These composites are known to enable a better thermal management and mechanical stability of the gain media and permit, therefore, to reach new frontiers in both the continuous-wave and ultrashort pulse regimes.

With the KYW crystal, the most popular tungstate crystal with a more mature technology, and KLuW, a newly introduced tungstate crystal, laser operation of various composite structures based on newly developed manufacturing method were investigated and slope efficiencies near the theoretical limit were achieved. In particular, the efficient laser operation based on planar waveguide structures was obtained, which corresponds to new possible applications in integrated optics for such compounds.

In the mode-locked regime, these new composites were also studied and some of the shortest pulses ever obtained directly from an Yb-doped oscillator were achieved. These results

demonstrate that these composite structures do not limit the potential of the gain media by uncontrolled rise of parasitic reflections or modulations but help to minimize the thermal effects. So, the quasi-three level nature of Yb-doped lasers can be well controlled and ultimate performance can be obtained.

An other point of interest was to develop highly doped crystals for the introduction of extremely thin disk elements. In this geometry that allows very efficient cooling of the active layer, the monoclinic double tungstates are ideal as they exhibit the highest absorption cross section of usual hosts and therefore allow efficient absorption in a single pass absorption configuration. Actually, a close comparison between the monoclinic double tungstates shows that KLuW is ideally suited for Yb doping. The minimal ionic radii difference between the Yb and Lu ions prevents important stress and defect formation in the crystal. This host is also optimum for the production of complex structures based on highly doped and undoped layers with small lattice mismatch and therefore high optical quality of the interface. Finally, the Yb substitution is expected to affect only weakly the thermal conductivity of the host.

Thus, composite structures based on highly doped Yb:KLuW were developed by collaborators and the first thin disk laser pumped in a single pass in the absorption maximum was demonstrated in this work. Moreover, the thickness of such active layer was for the first time below 100 μm, ensuring an optimal heat extraction at high power level. Thus, these results correspond to entirely new perspectives in high power laser operation with very simple pump designs.

The other group of crystals that was studied in this thesis was that of the tetragonal double tungstates. These crystals are characterized by a significant inhomogeneous broadening of the linewidths that can be related to the local disorder of these hosts. One of the most attractive host of this category, the Yb:NaYW, was fully characterized in CW and mode-locked operation. CW laser experiments permitted to select the most favorable orientation of this uniaxial crystal and study of the tunability showed a strong potential for ultrashort pulse generation. In the passive mode-locked regime, this potential was confirmed as pulses as short as 53 fs were obtained, corresponding to one of the shortest pulses ever generated from an Yb-doped laser.

In future works, the study of more elaborated composite structures based on monoclinic doubles tungstates will be considered. In particular, waveguide lasers with higher optical confinement have to be studied as well as channel waveguides that permit to achieve laser operation with even lower threshold. Considering the thin disk geometry, the manufacture of highly doped composite crystals with extremely thin active layers (less than 50 μm) will be investigated. Such structures can also be studied in the mode-locked regime where high average output power and high pulse energies can be achieved.

Concerning the tetragonal compounds, further investigation of the most favorable host with the optimal concentration and thickness for broad tunability and ultrashort pulse generation has to be performed. Such disordered compounds, that are characterized by a low thermal conductivity, can also largely benefit from the implementation of composite structures.

In the future, dispersion compensation methods allowing a better control of higher order dispersion will also be considered so that transform limited pulses with even shorter pulse duration can be generated. Finally, investigation of double tungstates with other prospective ions will continue. In particular, Tm- and Ho-doped double tungstates are interesting for efficient laser operation in the 2 μm spectral range.

Appendix A

A.1 Properties of Yb:KLu$(WO_4)_2$

Some important physical properties of the Yb:KLuW as well as the Stark level energies determined at low temperature (6-10 K) are presented in the following tables

Properties	
Temperature of polymorphic transformation/melting [K]	1312 / 1326, 1330
Crystal structure (space group - point group)	monoclinic centrosymmetric (C2/c=C^6_{2h}) - 2/m
site symmetry / coordination number / Lu^{3+} ionic radius	C_2 / 8 / 0.977 Å
lattice constants	a=10.576(7) Å, b=10.214(7) Å, c=7.487(2) Å, β=130.68(4)°, Z=4
cell volume and density	613.3(6) $Å^3$ and 7,686 g/cm^3
cation density / minimum Lu-Lu separation	6.52×10^{21} cm^{-3} / 4.045(3) Å
transparency range (1 cm^{-1} level for 1 mm thickness)	365-5110 nm
refractive index @ 1μm	n_p=1.995, n_m=2.030, n_g=2.084
optical ellipsoid orientation (632.8 nm)	$N_p \parallel b, \angle(a, N_m) = 59,2°, \angle(c, N_g) = 18.5°$
angle between the two optic axes at 1064 nm	$2V_g$=82.03°(optically positive)
strongest phonon mode [cm^{-1}]	908, 756
specific heat @ 300 K / 363 K / 1099 K	324.4 / 350 (365) / (701) J/kgK
thermal conductivity coefficient κ @ 298 K / 563 K	$\kappa_1 = 3.09/2.49$ $Wm^{-1}K^{-1}$, $\kappa_2 = 2.55/2.05$ $Wm^{-1}K^{-1}$,
	$\kappa_3 = 4.40/3.15$ $Wm^{-1}K^{-1}$
and orientation of the condicitivity ellipsoid, $X_1X_2X_3$	$X_2 \parallel b, \angle(a, X_1) = 6.34°/1.94°, \angle(X_3, c) = 34.4°/38.8°$
thermal expansion coefficients $\alpha[10^{-6}$ $K^{-1}]$ and	$\alpha_{11} = 8.98(12.8), \alpha_{22} = 3.35(7.8), \alpha_{33} = 16.72(22.2)$
orientation of the thermal expansion ellipsoid, $X_1X_2X_3$	$X_2 \parallel b, \angle(a, X_1) = 27.24°$

Table A.1: Physical properties of the monoclinic KLuW crystal host.

Manifold	Stark level energy [cm^{-1}]
$^2F_{7/2}$	0, 175, 435, 559
$^2F_{5/2}$	10187, 10498, 10735

Table A.2: Experimental Stark level energies of Yb^{3+}observed in KLuW.

A.2 Sellmeier equations and coefficients for several optical materials

The Sellmeier series equation for optical glass can be written as follow

$$n^2(\lambda) = 1 + \frac{B_1\lambda^2}{\lambda^2 - C_1} + \frac{B_2\lambda^2}{\lambda^2 - C_2} + \frac{B_3\lambda^2}{\lambda^2 - C_3} \tag{A.1}$$

where the wavelength λ is expressed in μm. The different order of derivation can also be easily calculated [Klo06]

$$\frac{dn(\lambda)}{d\lambda} = -\frac{1}{n(\lambda)} \sum_i \frac{B_i C_i \lambda}{(\lambda^2 - C_1)^2} \tag{A.2}$$

$$\frac{d^2n(\lambda)}{d\lambda^2} = -\frac{1}{n(\lambda)} \left[\left(\frac{dn(\lambda)}{d\lambda} \right)^2 - \sum_i \frac{3B_i C_i \lambda^2 + B_i C_i^2}{(\lambda^2 - C_i)^3} \right] \tag{A.3}$$

$$\frac{d^3n(\lambda)}{d\lambda^3} = -\frac{3}{n(\lambda)} \left[\frac{dn(\lambda)}{d\lambda} \frac{d^2n(\lambda)}{d\lambda^2} - \sum_i \frac{4B_i C_i \lambda^3 + 4B_i C_i^2 \lambda}{(\lambda^2 - C_i)^4} \right] \tag{A.4}$$

The Sellmeier coefficients can be found in the literature for most optical materials and are given here for the materials that have been used in this work

	Fused Silica	**LaFN28**	**SF10**
B_1	6.961663×10^{-1}	1.75882549	1.61625977
B_2	4.079426×10^{-1}	3.1519767×10^{-1}	$2.59229334 \times 10^{-1}$
B_3	8.974794×10^{-1}	1.19029675	1.07762317
C_1 [μm^2]	$4.67914826 \times 10^{-3}$	$8.72810026 \times 10^{-3}$	$1.27534559 \times 10^{-2}$
C_2 [μm^2]	$1.35120631 \times 10^{-2}$	$2.93020832 \times 10^{-2}$	$5.81983954 \times 10^{-2}$
C_3 [μm^2]	$9.79340025 \times 10^{+1}$	$8.51780644 \times 10^{+1}$	$1.16607680 \times 10^{+2}$

Table A.3: Sellmeier coefficients for several optical glasses

Bibliography

[Ack02] L. Ackermann. Method for producing segmented crystals. *Patents US 6387177, DE 19936651*, 2002.

[Agr01] P. Agrawal. *Nonlinear Fiber Optics*. San Francisco, CA : Academic Press, third edition, 2001.

[ASA+04] A. Aznar, R. Solé, M. Aguiló, F. Díaz, U. Griebner, R. Grunwald, and V. Petrov. Growth, optical characterization and laser operation of epitaxial Yb:$KY(WO_4)_2$/$KY(WO_4)_2$ composites with monoclinic strucutre. *Applied Physics Letters*, 85:4313–4315, 2004.

[BB01] A. Brenier and G. Boulon. Overview of the best Yb^{3+}-doped laser crystals. *Journal of Alloys and Compounds*, 323-324:210–213, 2001.

[BB06] G. L. Bourdet and E. Bartnicki. Generalized formula for continuous-wave end-pumped Yb-doped material amplifier gain and laser output power in various pumping configurations. *Applied Optics*, 45(36):9203–9209, 2006.

[BBST00] C. L. Bonner, T. Bhutta, D. P. Shepherd, and A. C. Tropper. Double-clad structures and proximity coupling for diode- bar-pumped planar waveguide lasers. *IEEE Journal of Quantum Electronics*, 36(2):236–242, 2000.

[BBW+97] C. T. A. Brown, C. L. Bonner, T. J. Warburton, D. P. Shepherd, A. C. Tropper, Hanna D. C., and H. E. Meissner. Thermally bonded planar waveguide lasers. *Appliel Physics Letters*, 71:1139–1141, 1997.

[Bou00] G. L. Bourdet. Theoretical investigation of quasi-three-level longitudinally pumped continuous wave lasers. *Applied Optics*, 39(6):966–971, 2000.

[Bou01] G. L. Bourdet. New evaluation of ytterbium-doped materials for cw laser applications. *Optics Communications*, 198:411–417, 2001.

[BSAdA+00] F. Brunner, G. J. Spühler, J. Aus der Au, L. Krainer, F. Morier-Genoud, R. Paschotta, N. Lichtenstein, S. Weiss, C. Harder, A. A. Lagatsky, A. Abdolvand, N. V. Kuleshov, and U. Keller. Diode-pumped femtosecond Yb:$KGd(WO_4)_2$ laser with 1.1-W average power. *Optics Letters*, 25:1119–1121, 2000.

[BTI+02] F. Brunner, Südmeyer, T., E. Innerhofer, F. Morier-Genoud, R. Paschotta, V. E. Kisel, V. G. Shcherbitsky, N. V. Kuleshov, J. Gao, K. Contag, A. Giesen, and U. Keller. 240-fs pulses with 22-W average power from a mode-locked thin disk Yb:$KY(WO_4)_2$ laser. *Optics Letters*, 27:2261–1164, 2002.

[CSEB+06] C. Cascales, M. D. Serrano, F. Esteban-Betegon, C. Zaldo, R. Peters, K. Petermann, G. Huber, L. Ackermann, D. Rytz, C. Dupre, M. Rico, U. Griebner, and

V. Petrov. Structural, spectroscopic, and tunable laser properties of Yb^{3+}-doped $NaGd(WO_4)_2$. *Physical Review B*, 74:174114, 2006.

[CTHGC+08] J. M. Cano-Torres, X. Han, A. Garcia-Cortes, M. D. Serrano, C. Zaldo, F. J. Valle, X. Mateos, S. Rivier, U. Griebner, and V. Petrov. Infrared spectroscopic and laser characterization of Tm in disordered double tungstates. *Materials Science and Engineering: B*, 146:22–28, 2008.

[DC63] G. H. Dieke and H. M. Crosswhite. The spectra of the doubly and triply ionized rare earths. *Applied Optics*, 2(7):675–686, 1963.

[DCB+05] F. Druon, S. Chenais, F. Balembois, P. Georges, R. Gaume, and B. Viana. Diode-pumped continuous-wave and femtosecond laser operation of a heterocomposite crystal Yb^{3+}:$SrY_4(SiO_4)_3O/Y_2Al_5O_{12}$. *Optics Letters*, 30:857–859, 2005.

[Dex53] D. L. Dexter. A theory of sensitized luminescence in solids. *Journal of Chemical Physics*, 21(5):836–850, 1953.

[DG85] M. J. F. Digonnet and C. J. Geata. Theoretical analysis of optical fiber laser amplifiers and oscillators. *Applied Optics*, 24(3):333–342, 1985.

[DMSH66] A. J. De Maria, D. A. Stetser, and H. Heynau. Self mode-lockng of lasers with saturable absorbers. *Applied Physics Letters*, 8:174–176, 1966.

[DPC+93] L. D. Deloach, S. A. Payne, L. K. Chase, L. L. anc Smith, W. L. Kway, and W. F. Krupke. Evaluation of absorption and emission properties of Yb^{3+} doped crystals for laser applications. *IEEE Journal of Quantum Electronics*, 29(4):1179–1191, 1993.

[dSMP+03] D. F. de Sousa, N. Martynyuk, V. Peters, K. Lunstadt, K. Rademaker, K. Petermann, and S. Basun. Quenching behavior of highly doped Yb:YAG and YbAG. *Lasers and Electro-Optics Europe, 2003. CLEO/Europe.*, page 337, 2003.

[EKK+84] J. M. Eggleston, T. J. Kane, K. Kuhn, J. Unternahrer, and R. L. Byer. The slab geometry laser - part 1: theory. *IEEE Journal of Quantum Electronics*, 26(3):289–301, 1984.

[FB87] T. Y. Fan and R. L. Byer. Modeling and cw operation of a quasi-three level 946 nm Nd:YAG laser. *IEEE Journal of Quantum Electronics*, 23(5):605–612, 1987.

[FCC99] B. Ferrand, B. Chambaz, and M. Couchaud. Liquid phase epitaxy: A versatile technique for the development of miniature optical components in single crystal dielectric medias. *Optical Materials*, 11:101–114, 1999.

[FMG84] R. L. Fork, O. E. Martinez, and J. P. Gordon. Negative dispersion using pairs of prisms. *Optics Letters*, 9:151–153, 1984.

[GCH+07] A. García-Cortés, J. M. Cano-Torres, X. Han, C. Cascales, C. Zaldo, X. Mateos, S. Rivier, U. Griebner, V. Petrov, and F. J. Valle. Tunable continuous wave and femtosecond mode-locked Yb^{3+} laser operation in $NaLu(WO_4)_2$. *Journal of Applied Physics*, 101:3110, 2007.

[GCTS+07] A. García-Cortés, J. M. Cano-Torres, M. D. Serrano, C. Casacales, C. Zaldo, S. Rivier, X. Mateos, U. Griebner, and V. Petrov. Spectroscopy and lasing of Yb-doped $NaY(WO_4)_2$: tunable and femtosecond mode-locked laser operation. *IEEE Journal of Quantum Electronics*, 43(9):758–764, 2007.

[GGS+00] U. Griebner, R. Grunwald, H. Schönnagel, J. Huschke, and G. Erbert. Laser with guided pump and free-propagating resonator mode using diffusion-bonded rectangular waveguides. *Applied Physics Letters*, 77:3505–3507, 2000.

[GHV+94] A Giesen, H Hugel, A Voss, K Wittig, U Brauch, and H. Opower. Scalable concept for diode-pumped high-power solid-state lasers. *Applied Physics B - Lasers and Optics*, 58(5):365–372, 1994.

[GRB+07] F. Gardillou, R. E. Romanyuk, C. N. Borca, R. P. Salathé, and M. Pollnau. Lu, Gd co-doped $KY(WO_4)_2$:Yb epitaxial layers: Towards integrated optics based on $KY(WO_4)_2$. *Optics Letters*, 32:488–490, 2007.

[GRP+05] U. Griebner, S. Rivier, V.. Petrov, M. Zorn, M. Weyers, X. Mateos, R. Solé, J. Gavaldà, M. Aguiló, J. Massons, and F. Díaz. Passively mode-locked Yb:$KLu(WO_4)_2$ oscillators. *Optics Express*, 13:3465–3470, 2005.

[GS07] A Giesen and J. Speiser. Fifteen years of work on thin disk lasers: Results and scaling laws. *IEEE Journal of Selected Topics in Quantum Electronics*, 13(3):598–609, 2007.

[GSP+07] A. Giesen, J. Speiser, R. Peters, C Kränkel, and K. Petermann. Thin-disk lasers come of age. *Photonics Spectra*, pages 52–58, 2007.

[GT64] F. Gires and P. Tournois. Interferometre utilisable pour la compression d' impulsion lumineuses modulees en frequence. *Comptes Rendu de l'Académie des Sciences, Paris*, 258:6112–6115, 1964.

[GVV03] R. Gaume, B. Viana, and D. Vivien. A simple model for the prediction of thermal conductivity in pure and doped insulating crystals. *Applied Physics Letters*, 83(7):1355–1357, 2003.

[Hau00] H. A. Haus. Mode-locking of lasers. *IEEE Journal of Selected Topics in Quantum Electronics*, 6:1173–1185, 2000.

[HBP+06] J. E. Hellström, S. Bjurshagen, V. Pasiskevicius, J. Liu, V. Petrov, and U. Griebner. Efficient Yb:KGW lasers end-pumped by high-power diode bars. *Applied Physics B*, 83:235–239, 2006.

[HCCS+07] X. Han, A. Carcia-Cortes, M. D. Serrano, C. Zaldo, and C. Cascales. Structural and thermal properties of tetragonal double tungstate crystals intended for ytterbium laser composites. *Chemistry of Materials*, 19:3002–3010, 2007.

[HKM97] J. Herrmann, V. P. Kalosha, and M. Müller. Higher-order phase dispersion in femtosecond Kerr-lens mode-locked solid-state lasers: sideband generation and pulse splitting. *Optics Letters*, 22:236–238, 1997.

[HMGM+98] C. Hönninger, F. Morier-Genoud, M. Moser, U. Keller, L. R. Brovelli, and C. Harder. Efficient and tunable diode-pumped femtosecond Yb:glass lasers. *Optics Letters*, 23:126–128, 1998.

[HMN93] H. A. Haus, J. D: Moores, and L. E. Nelson. Effect of third-order dispersion on passive mode locking. *Optics Letters*, 18:51–53, 1993.

[Hol06] G. R. Holtom. Mode-locked Yb:KGW laser longitudinally pumped by polarization-coupled diode bars. *Optics Letters*, 31:2719–2721, 2006.

[HPMG+99] C. Hoenninger, R. Paschotta, F. Morier-Genoud, M. Moser, and U. Keller. Q-switching stability limits of continuous-wave passive mode-locking. *Journal of the Optical Society of America B*, 16:46–56, 1999.

[KAdAK98] F. X. Kärtner, J. Aus der Au, and U. Keller. Mode-locking with slow and fast saturable absorbers - what's the difference? *IEEE Journal of Selected Topics in Quantum Electronics*, 4:159–168, 1998.

[Kan89] D. M. Kane. Astigmatism compensation in off-axis laser resonators with two or more coupled foci. *Optics Communication*, 71:113–118, 1989.

[KBDU06] D. Kouznetsov, J.-F. Bisson, J. Dong, and K.-I. Ueda. Surface loss limit of the power scaling of a thin disk laser. *Journal of the Optical Society of America B*, 23(5):1074–1082, 2006.

[KBss] D. Kouznetsov and J.-F. Bisson. Role of anti-ASE cap in the scaling of thin disk lasers. *Journal of the Optical Society of America B*, in press.

[Kel04] Ursula Keller. Ultrafast solid-state lasers. In *Progress in Optics*, volume 46, pages 1–115. Editor: Emil Wolf, 2004.

[KFB+92] F. Krausz, M. E. Fermann, T. Brabec, P. F. Curley, M. Hofer, M. H. Ober, C. Spielmann, E. Wintner, and A. J. Schmidt. Femotsecond solid-state lasers. *IEEE Journal of Quantum Electronics*, 28:2097–2122, 1992.

[KFK+07] H. Kühn, S. T. Fredrich-Thornton, C. Kränkel, R. Peters, and K. Petermann. Model for the calculation of radiation trapping and description of the pinhole method. *Optics Letters*, 32:1908–1910, 2007.

[KJK96] F. X. Kärtner, I. D. Jung, and U. Keller. Soliton mode-locking with saturable absorbers. *IEEE Journal of Selected Topics in Quantum Electronics*, 2:540–556, 1996.

[KK69] P. V. Klevtsov and L. P. Kozeeva. Synthesis and X-ray and thermal studies of potassium rare-earth tungstates, $KLn(WO_4)_2$, Ln = rare-earth element. *Soviet Physics Doklady*, 14:185–187, 1969, (Transl.: Doklady Akademii Nauk SSSR, vol. 185, pp. 571-574, 1969).

[KK95] F. X. Kärtner and U. Keller. Stabilization of solitonlike pulses with a slow saturable absorber. *Optics Letters*, 20:16–18, 1995.

[KKK75] P. V. Klevtsov, L. P. Kozeeva, and L. Y. Kharchenko. Study on the crystallization and polymorphism of double potassium and trivalent tungstates, $KR(WO_4)_2$. *Soviet Physics Crystallography*, 20:732–735, 1976, (Transl.: Kristallografiya 20:1210-1215, 1975).

[Klo06] P. Klopp. *New Yb^{3+}-doped laser materials and their application in continuous-wave and mode-locked laser*. PhD thesis, Humbolt-Universitat Berlin, 2006.

[KLP+97] N. V. Kuleshov, A. A. Lagastky, A. V. Podlipensky, V. P Mikhailov, and G. Huber. Pulsed laser operation of Yb-doped $KY(WO_4)_2$ and $KGd(WO_4)_2$. *Optics Letters*, 22:1317–1319, 1997.

[KLS+97] N. V. Kuleshov, A. A. Lagastky, V. G. Shcherbitsky, V. P. Mikhailov, M.-T. Heumann, T. Jensen, A. Diening, and G. Huber. Cw laser performance of Yb and Er, Yb doped tungstates. *Applied Physics B*, 64:409–413, 1997.

[KPG+03] P. Klopp, V. Petrov, U. Griebner, V. Nesterenko, V. Nikolov, M. Marinov, M. A. Burukova, and M. Galan. Continuous-wave lasing of a stoichiometric Yb laser material: $KYb(WO_4)_2$. *Optics Letters*, 28:322–324, 2003.

[KPGE02] P Klopp, V. Petrov, U. Griebner, and G. Erbert. Passively mode-locked Yb:KYW laser pumped by a tapered diode laser. *Optics Express*, 10:108–113, 2002.

[KTS+06] V. A. Kisel, A. E. Troshin, V. G. Shcherbitskii, N. V. Kuleshov, A. A. Pavlyuk, F. Brunner, R. Paschotta, F. Morier-Genoud, and U. Keller. Luminescent and lasing characteristics of heavily doped Yb^{3+}:$KY(WO_4)_2$ crystals. *Quantum Electronics*, 36:319–323, 2006.

[KWK+96] U. Keller, K. J. Weingarten, F. X. Kärtner, D. Kopf, B. Braun, I. D. Jung, R. Fluck, C. Hönninger, N. Matuschek, and J. Aus der Au. Semiconductor saturable absorber mirrors (SESAM's) for femtosecond to nanosecond pulse generation in solid-state lasers. *IEEE Journal of Selected Topics in Quantum Electronics*, 2:435–453, 1996.

[LB93] B. E. Lemoff and C. P. J. Barty. Cubic-phase-free dispersion compensation in solid-state ultrashort-pulse laser. *Optics Letters*, 18:57–59, 1993.

[LBER91] H. C. Lee, O. L. Brownlie, Meissner H. E., and R. C. Rea. Diffusion bonded composites of YAG single crystals. *Proceedings of SPIE.*, 1624:1, 1991.

[LBNG07] M. Larionov, F. Butze, D. Nickel, and A. Giesen. High-repetition-rate regenerative thin-disk amplifier with 116 μJ pulse energy and 250 fs pulse duration. *Optics Letters*, 32:494–496, 2007.

[LCW+91] P. Lacovara, H. K. Choi, C. A. Wang, R. L. Aggarwal, and T. Y. Fan. Room-temperature diode-pumped Yb:YAG laser. *Optics Letters*, 16:1089–1091, 1991.

[LKM99] A. A. Lagatsky, N. V. Kuleshov, and V. P. Mikhailov. Diode pumped CW lasing of Yb:KYW and Yb:KGW. *Optics Communication*, 165:71–75, 1999.

[LMZ+05] J. Liu, X. Mateos, H. Zhang, J. Wang, M. Jiang, U. Griebner, and V. Petrov. Continuous-wave laser operation of Yb:$LuVO_4$. *Optics Letters*, 30(23):3162–3164, 2005.

[LNM01] H. Liu, J. Nees, and G. Mourou. Diode-pumped kerr-lens mode-locked Yb:$KY(WO_4)_2$ laser. *Optics Letters*, 26:1723–1725, 2001.

[LPG+07] J. Liu, V. Petrov, U. Griebner, V. Nesterenko, V. Nikolov, M. Marinov, M. A. Burukova, and M. Galan. Efficient high-power laser operation of Yb:$KLu(WO_4)_2$ crystals cut along the principal optical axes. *Optics Letters*, 32:2016–2018, 2007.

[Mac07] J. I. Mackenzie. Dielectric solid-state planar waveguide lasers: a review. *IEEE Journal of Selected Topics in Quantum Electronics*, 13(3):626–637, 2007.

[McC64] D. E. McCumber. Einstein relations connecting broadband emission and absorption spectra. *Physical Review*, 136(4A):954–957, 1964.

[MIKK07] S. Matsubara, M. Inoue, S. Kawato, and T. Kobayashi. Continous wave laser oscillation of stoichiometric YbAG crystal. *Japanese Journal of applied physics 2*, 46(1-3):L61–L63, 2007.

[MNA+03] A. Major, I. Nikolakakos, J. S. Aitchison, A. I. Ferguson, N. Langford, and P. W. E. Smith. Characterization of the nonlinear refractive index of the laser crystal Yb:$KGd(WO_4)_2$. *Applied Physics B*, 77:433–436, 2003.

[Mou86] P. F. Moulton. Spectroscopic and laser characteristics of $TiAl_2O_3$. *Journal of the Optical Society of America B*, 3:125–133, 1986.

[MPA+04] X. Mateos, V. Petrov, M. Aguiló, R. M. Solé, J. Gavaldà, J. Massons, F. Díaz, and U Griebner. Continuous-wave laser oscillation of Yb^{3+} in monoclinic $KLu(WO_4)_2$,. *IEEE Journal of Quantum Electronics*, 40(8):1056–1059, 2004.

[MPS+95] C. D. Marshall, S. A. Payne, L. K. Smith, H. T. Powell, W. F. Krupke, and B. H. T. Chai. 1.047-μm Yb:$Sr_5(PO_4)_3F$ energy storage optical amplifier. *IEEE Journal of Selected Topics in Quantum Electronics*, 1(1):67–77, 1995.

[MSG+05] X. Mateos, R. Solé, J. Gavaldà, M. Aguiló, J. Massons, F. Díaz, V. Petrov, and U. Griebner. Crystal growth, spectroscopic studies and laser operation of Yb^{3+}-doped potassium lutetium tungstate. *Optical Materials*, 28:519–523, 2005.

[PFPJ+05] K. Petermann, D. Fagundes-Peters, J. Johannsen, M. Mond, V. Peters, J. J. Romero, S. Kutovoi, J. Speiser, and A. Giesen. Highly Yb-doped oxides for thin-disc lasers. *Journal of Crystal Growth*, 275:135–140, 2005.

[PHS+01] F. D. Patel, E. C. Honea, J. Speth, S. E. Payne, R. Hutcheson, and R. Equall. Laser demonstration of $Yb_3Al_5O_{12}$ (YbAG) and materials properties of highly doped Yb:YAG. *IEEE Journal of Quantum Electronics*, 37(1):135–144, 2001.

[PHS04] G. Paunescu, J. Hein, and R. Sauerbrey. 100-fs diode-pumped Yb:KGW mode-locked laser. *Applied Physics B*, 79:555–558, 2004.

[PK03] R. Paschotta and U. Keller. Ultrafast solid-state lasers. In *Ultrafast lasers*, pages 1–60. Ed.: M. E. Fermann, A. Galvanauskas, G. Sucha, 2003.

[PKPH07] R. Peters, C. Kränkel, K. Petermann, and G. Huber. Thin-disk laser operation of Yb3+-Doped NaGd(WO4)2. In *Advanced Solid-State Photonics*, page MA4. Optical Society of America, 2007.

[PPG+06] V. Petrov, K. Petermann, U. Griebner, V. Peters, J. Liu, M. Rico, P. Klopp, and G. Huber. Continuous-wave and mode-locked lasers based on cubic sesquioxide crystalline hosts. volume 6216, page 62160H. SPIE, 2006.

[PPM+07] V. Petrov, M. C. Pujol, X. Mateos, O. Silvestre, S. Rivier, M. Aguiló, R. M. Solé, J. Liu, U Griebner, and F. Díaz. Growth and properties of $KLu(WO_4)_2$ and novel ytterbium and thulium lasers based on this monoclinic crystalline host. *Laser & Photonics Review*, 1(2):179–212, 2007.

[PR07] M. Pollnau and Y. E. Romanyuk. Optical waveguides in laser crystals. *Comptes Rendu de Physique*, 8:123–137, 2007.

[PRG+06] V. Petrov, S. Rivier, U. Griebner, J. Liu, X. Mateos, A. Aznar, R. Solé, M. Aguiló, and F. Díaz. Epitaxially grown Yb:$KLu(WO_4)_2$ composites for continuous-wave and mode-locked lasers in the 1 μm spectral range. *Journal of Non-Crystalline Solids*, 352(23-25):2367–2370, 2006.

[PRG+07] M. Pollnau, Y. E. Romanuyk, F. Gardillou, C. N. Broca, S. Rivier, U. Griebner, and V. Petrov. Double tungstate lasers: towards on-chip integrated devices. *IEEE Journal of Selected Topics in Quantum Electronics*, 32(15):1343–1344, 2007.

[PSM+02] X. Pujol, M. C. Mateos, R. Solé, J. Massons, J. Gavaldà, X. Solans, F. Díaz, and M. Aguiló. Structure crystal growth and physical anisotropy of $KYb(WO_4)_2$, a new laser matrix. *Journal of Applied Chrystallography*, 35:108–112, 2002.

[PSSM07] G. Palmer, M. Siegel, A. Steinmann, and U. Morgner. Microjoule pulses from a passively mode-locked Yb:$KY(WO_4)_2$ thin-disk oscillator with cavity dumping. *Optics Letters*, 32:1593–1595, 2007.

[Ris88] W. P. Risk. Modeling of longitudinally pumped solid-state lasers exhibiting reabsorption losses. *Journal of the Optical Society of America B*, 5(7):1412–1423, 1988.

[RJM+05] J. J. Romero, J. Johannsen, M. Mond, K. Petermann, G. Huber, and E. Heumann. Continuous-wave laser action of Yb^{3+}-doped lanthanum scandium borate. *Applied Physics B: Laser and Optics*, 80:159–163, 2005.

[RML+06] S. Rivier, X. Mateos, J. Liu, V. Petrov, U. Griebner, M. Zorn, M. Weyers, H. Zhang, J. Wang, and M. Jiang. Passively mode-locked Yb:$LuVO_4$ oscillator. *Optics Express*, 14(24):11668–11671, 2006.

[RMP+07] S. Rivier, X. Mateos, V. Petrov, U. Griebner, Y. E. Romanuyk, C. N. Borca, F. Gardillou, and M. Pollnau. Tm:$KY(WO_4)_2$ waveguide laser. *Optics Express*, 15(9):1885–1892, 2007.

[RPG+05] S. Rivier, V. Petrov, U. Griebner, A. Aznar, X. Mateos, O. Silvestre, R. Solé, M. Aguiló, F Díaz, M. Zorn, and M. Weyers. Mode-locked laser operation of epitaxially grown Yb:$KLu(WO_4)_2$ composite. *Optics Letters*, 28(18):2484–2486, 2005.

[RSK07] S. Rivier, A. Schmidt, and Kränkel, C. and Peters, R and Petermann, K. and Huber, G. and Zorn, M. and Weyers, M. and Erbert, G. and Petrov, V. Ultrashort pulse Yb:$LaSc_3(BO_3)_4$ mode-locked oscillator. *Optics Express*, 15:15539–15544, 2007.

[SF94] D. S. Sumida and T. Y. Fan. Effect of radiation trapping on fluorescence lifetime and emission cross section measurements in solid-state laser media. *Optics Letters*, 19:1343–1345, 1994.

[SFSK94] R. Szipöcs, K. Ferencz, C. Spielmann, and F. Krausz. Chirped multilayer coatings for broadband dispersion control in femtosecond lasers. *Optics Letters*, 19:201–203, 1994.

[SHHV91] M. Sheikbahae, D. C. Hutchings, D. J. Hagan, and E. W. Vanstryland. Dispersion of bound electronic nonlinear refraction in solids. *IEEE Journal of Quantum Electronics*, 27:1296–1309, 1991.

[SHL+01] D. P. Shepherd, S. J. Hettrick, C. Li, J. I. Mackenzie, R. J. Beach, S. C: Mitchell, and H. E. Meissner. High-power planar dielectric waveguide lasers. *Journal of Physics D: Applied Physics*, 34:2420–2432, 2001.

[SKS91] D. E. Spence, P. N. Kean, and W. Sibbett. 60-fs pulse generation from a self-mode-locked Ti-sapphire laser. *Optics Letters*, 16:42–44, 1991.

[SNR+96] R. Solé, V. Nikolov, X. Ruiz, J. Gavaldà, X. Solans, M. Aguiló, and F. Díaz. Growth of β-$KGd_{1-x}Nd_x(WO_4)_2$ single crystals in $K_2W_2O_7$ solvents. *Journal of Crystal Growth*, 169:600–603, 1996.

[Spr07] Springer. *Handbook of lasers and optics*. Ed. : Frank Traeger, 2007.

[SSG+06] F. Saas, G. Steinmeyer, U. Griebner, M. Zorn, and M. Weyers. Exciton resonance tuning for the generation of subpicosecond pulses from a mode-locked semiconductor disk laser. *Applied Physics Letters*, 89:141107, 2006.

[ST91] B. E. A. Saleh and M. C. Teich. *Fundamentals of Photonics*. John Wiley & Sons, Inc., 1991.

[TKJ+99] E. R. Thoen, E. M. Koontz, M. Joschko, P. Langlois, T. R. Schobli, and Kärtner, F. X. and Ippen, E. P. and Kolodziejski, L. A. Two-photon absorption in semiconductor saturable absorber mirrors. *Applied Physics Letters*, 74:3927, 1999.

[TTB97] T. Taira, W. M. Tulloch, and R. L. Byer. Modeling of quasi-three-level lasers and operation of cw Yb:YAG lasers. *Applied Optics*, 36(9):1867–1874, 1997.

[TTKI97] M. Tsunekane, N. Tagichi, T. Kasamatsu, and H. Inaba. Analytical and experimental studies on the characteristics of composite sold-state laser rods in diode-end-pumped geometry. *IEEE Journal of Selected Topics in Quantum Electronics*, 3(1):9–18, 1997.

[ZDB+06] Y. Zaouter, J. Didierjean, F. Balambois, G. Lucas Leclin, F. Druon, P. Georges, J. Petit, P. Goldner, and B. Viana. 47-fs diode-pumped Yb^{3+}:$CaGdAlO_4$ laser. *Optics Letters*, 31:119–121, 2006.

list of symbols

a, b, c	crystallographic axis
A	effective laser mode area
$A(z,t)$	slow varying enveloppe
A, B, C, D	Sellmeier coefficient
α	thermal expansion coefficient or linear absorption coefficient
β	inversion parameter
β_{min}	minimum inversion parameter to reach transparency
β_i	i^{th} order dispersion
γ	self-phase modulation coefficient
c	speed of light in vacuum
χ	electric susceptibility
d	core thickness of a planar waveguide
$\Delta\nu$	spectral bandwidth FWHM
ΔR	modulation depth of a saturable absorber
$\mathbf{E}$	electric field strength (vector)
E_i	energy of level i
$E_{sat,a}$	saturation pulse energy in a saturable absorber
$E_{sat,g}$	saturation pulse energy of the gain media
E_Y	Young modulus
E_z	energy of the zero line transition
f	focal length
f_i	fractional population in the energy level i
g_i	degeneracy of states i
γ	self-phase modulation coefficient
h	Planck constant
η	optical efficiency or slope efficiency
I_L	laser intensity
I_{min}	minimum pump intensity to achieve crystal transparency
I_P	pump intensity
I_{sat}	saturation intensity
$k(\omega)$	wave number
k_B	Boltzmann constant
κ_i	principal thermal conductivity coefficient
L	distance between two prisms apices
l_c	crystal length
L_i	internal losses

λ	wavelength
n	refractive index
n_2	nonlinear refractive index
N	active ion concentration
N_i	population density of the energy level i
ν	optical frequency
ν_{Poi}	Poisson ratio
P	total optical path in a prism pair or electric polarization field
P_{th}	absorbed pump power at the laser threshold
ϕ	instantaneous phase
q	quantum defect
R_{abs}	absorption rate
R_{em}	stimulated emission rate
R_{nr}	non-radiative decay rate
ROC	radius of curvature
R_{OC}	reflection of the output coupler
R_P	pump transition rate
R_{rad}	radiative decay rate
R_{reabs}	reabsorption rate
R_{reem}	reemission rate
R_s	steady state resistance parameter
σ_{abs}	absorption cross section
σ_{em}	emission cross section
σ_g	gain cross section
σ_T	maximal surface stress
T	temperature
T_{OC}	output coupler transmission
τ	pulse duration
$\tau\Delta\nu$	time bandwidth product (FWHM)
τ_f	fluorescence lifetime
τ_{nr}	non-radiative lifetime
τ_{rad}	radiative lifetime
V_{eff}	effective mode volume
w_P, w_L	waist size of the pump and laser, respectively
X_i	principal axes of the thermal expansion tensor
z	longitudinal coordinate
Z_i	partition function of the energy level i

Acknowledgment

First of all, I would like to thank my supervisor Prof. I. V. Hertel for accepting me as a PhD student at the Max-Born-Institute and for his confidence and encouragements during these years. I also would like to thank the second member of the comittee, Prof. Markus Pollnau who accompanied my first steps in scientific research in Switzerland, greatly advised me to come here at the Max-Born-Insitute and finally cooperated with me during this project.

Of course, I would like to express all my thanks to Dr V. Petrov who coordinated the project with such competence and kindness. He was at all time disposed to answer skillfully to my numerous questions on very diverse subjects. Throughout this work, I also had the chance to have Dr U. Griebner as an additional project leader. I really would like to express my gratitude to both of them for their wonderful guidance and support during these years.

I also had the chance to meet a lot of great collaborators during this project. I especially appreciated to share the office and to work with Junhai Liu, Xavier Mateos, Mauricio Rico, Andreas Schmidt and Cinta Pujol. Thank you so much for sharing your knowledge with me and for the great time we spent together working at the MBI. Obviously, all the results that have been achieved and presented in this thesis would not have been possible without the expertise of all the people involved in this project. I really would like to thank all people that have been involved in the crystal growth characterization and their post-processing. The quality of the crystals and the related information that I have been receiving from all of you was absolutely amazing. In particular, I would like to thank all coworkers of Prof. Diaz in the Univesitat Rovira I Virgili, of Prof. Zaldo at the Materials Science Institute of Madrid and of Prof. Pollnau at the EPFL, Switzerland. I would also like to thank D. Rytz and S. Vernay from FEE GmbH as well as the researchers at the Ferdinand-Braun-Institute who developed the saturable absorbers and the laser diode.

Needless to say, I would like to thank all collaborators from the A3 group at the MBI and more generally from the Max-Born-Insitute for their participation in the good working environment. I especially think of Dr. Frank Noack, Gabriel Mügge, Wolfgang Krüger, Michael Dose and Marco Harwardt for the helpful discussions, for their infinite patience and goodwill, for their assistance when something went wrong in the lab, for the great birthday-breakfast parties but at first for their gentleness. It was great to work in such a competent and harmonious team.

Last but not least, I would like to thanks my family for their great support and all my friends in Berlin, in Switzerland or elsewhere for their never-ending encouragement. I am so grateful that you have been there for me over the past 4 years.

Curriculum vitae

Due to private data policy, the curriculum vitae of the author is not available in the online version.